Magnetic Effects in Astrophysically Relevant Laboratory Plasmas

Alexandra Rigby

Keble College

University of Oxford

Thesis submitted for the degree of

Doctor of Philosophy in Atomic and Laser Physics

Hilary 2018

Acknowledgments

First and foremost, I would like to thank my supervisor Gianluca Gregori for all his help, guidance, support and the many opportunities he has given me over the years.

I also wish to thank Bob Bingham for all his enthusiastic discussions and feedback; Petros Tzeferacos for always taking the time to provide assistance and Brian Reville for his willingness to fix both grammar and physics.

Thanks is due to the fellow members of Gianluca's group, Nick, Jena, Pawel, Paul, Brett, Konstantin, Jacob. A special thanks should go to Tom and Laura, my fellow crew mates on the SSG; Joe and Archie for their comments, both insightful and catty, and Matt for putting up with me as a lab partner for 8 years and always providing entertainment.

I was lucky enough to be involved in several collaborations. I would like to thank all those involved in making both the LULI and Omega experiments a success, especially Michel Koenig, Fabio Cruz, Joe Katz and Don Lamb. I also wish to thank the LLE and LULI staff for their technical advice and everyone at RAL for providing training courses and help with simulations.

I would like to thank my family and friends for their continual support and always offering a welcome distraction. Last but not least, I'd like to thank Dave for all of his support, patience and many mugs of tea.

Abstract

Astrophysics typically uses observation, theory and simulation to further the understanding of the cosmos. By using high power lasers, scaled astrophysical events can be created in the laboratory.

This thesis describes laboratory results based on two different astrophysical phenomena, particle acceleration and the turbulent dynamo mechanism, both of which are governed by magnetic fields.

Particle acceleration is commonly seen at astrophysical shocks. The exact mechanism of this acceleration, especially for electrons, remains unclear. One possible method of electron acceleration is through lower hybrid turbulence, a phenomena observed at the interaction between the Solar wind and a comet. The results from a laboratory experiment demonstrate the observation of electron acceleration via lower hybrid waves. Lower hybrid waves require an external magnetic field to generate the necessary electron accelerating instability.

Magnetic fields themselves are ubiquitous throughout the universe. Having generated seed fields through, for example an astrophysical shock, these magnetic fields can be amplified through the turbulent dynamo mechanism. To generate the dynamo mechanism within the laboratory, two plasma jets are collided. A new Faraday rotation diagnostic, for magnetic field measurements, was added to the suite of diagnostics characterizing the turbulent plasma. The setup, calibration and analysis for the Faraday rotation diagnostic is new to the OMEGA laser facility and dynamo experiment. The results from this new Faraday rotation diagnostic and Thomson scattering diagnostic allow the plasma parameters and evolution of the jets to be fully characterized.

Finally, the thesis is concluded by drawing these results together.

Role of the Author

This thesis contains experimental results relating to laboratory experiments. The work was not performed alone, but as part of a series of collaborations with others. In this section the author's contributions to the work will be clarified.

The introductory chapter 1 is written to put the work in a more general sense and place its important in terms of a wider context. The background theory in chapter 2 contains the necessary plasma physics required to understand the work in this thesis. The content contained in both these chapters is produced from a variety of sources of which the original authors are identified within the text.

Chapter 3 marks the beginning of the author's original work. It contains the design, execution and analysis of an experiment at the LULI laser facility. The original experimental idea was conceived by Gianluca Gregori, Robert Bingham, Brian Reville, Anthony Bell, Federico Fraschetti, Sergey Lebedev, Francesco Miniati and Subir Sarkar. The preparation and experiment was led by the author in November 2015. Analysis was performed by the author. Hydrodynamic simulations were performed by Petros Tzeferacos. PIC simulations were performed by Fabio Cruz. PrismSPECT simulations were performed by the author. The work has been accepted for publication in Nature Physics.

Chapter 4 describes the setup, calibration and analysis of a Faraday rotation diagnostic. The design and setup of the diagnostic was made by Joseph Katz and Dustin Froula. Analysis of the results was performed by the author. The results are compared with proton radiography, the analysis of which was performed by Archie Bott. This work has been submitted for publication in the HPLSE special issue on laboratory astrophysics.

Chapter 5 describes the Thomson scattering results from an experiment at the OMEGA laser facility. The experiment was originally conceived by Gianluca Gregori, Petros Tzeferacos, Don Lamb, Alexander Schekochihin and others. The author and others contributed to the preparation of the experiment. Analysis of the Thomson scattering data was performed by the author. Whilst the analysis presented in this thesis has not been published in its current form, the Thomson scattering analysis performed by the author has been published in Nature Communications.

Publications

First Author

- Rigby et al. *Electron Acceleration by Wave Turbulence in a Magnetized Plasma*, Nature Physics (accepted) (2018)
- Rigby et al. *Implementation of a Faraday Rotation Diagnostic at the OMEGA laser facility*, HPLSE laboratory astrophysics special issue (submitted) (2018)

Other Publications

- Tzeferacos et al. *Laboratory evidence of dynamo amplification of magnetic fields in a turbulent plasma*, Nature Communications, 9, 591, (2018)
- Tzeferacos et al. *Numerical modeling of laser-driven experiments aiming to demonstrate magnetic field amplification via turbulent dynamo*, Physics of Plasmas, 24, 041404, (2017)
- Kettle et al. *Experimental measurements of the collisional absorption of XUV radiation in warm dense aluminium*, Physical Review E, 94, 023203, (2016)
- Brambrink et al. *Short-pulse laser-driven x-ray radiography*, High power laser science and engineering, 4, (2016)
- Mabey et al. *Characterization of x-ray lens for use in probing high energy density states of matter*, Journal of Instrumentation, 10, (2015)

Contents

List of Figures

List of Tables

Chapter 1

Introduction and Motivation

This chapter introduces the concept of laboratory astrophysics and the motivation for investigating it as a research area.

Astrophysics is traditionally studied through observation, first through the naked eye and now through telescopes. Advances in telescope engineering have led to better resolution, allowing deeper regions of space to be probed. There is still a certain amount of luck in positioning the telescope at the right place and collecting data at the right time. Further, astrophysical events often happen over very large time scales, requiring data to be collected over the course of many years. Time on telescopes is often at a premium and so an alternative method for carrying out experiments would be helpful. Simulations offer an alternative way to replicate these events. However, simulations are limited by the current state of physics understanding and at the cost of running a supercomputer. As such, experiments are always required to validate simulation results.

Laboratory astrophysics offers an alternative experimental route. By creating conditions in the laboratory that are similar to astrophysical events, experiments can be performed that can be used to understand astrophysical phenomena [1, 2, 3, 4, 5]. Performing experiments within the laboratory has advantages: experiments can be performed at a much higher rate and with greater control over the system's design.

To create accurately scaled experiments [6, 7], there are certain conditions that must be satisfied:

1. Create conditions required to match the astrophysical case,

2. Show that the underlying physics is independent of the scale of the system,

3. Design relevant experiments to further the understanding of specific astrophysical cases.

To create astrophysically relevant conditions, often a plasma needs to be generated. Plasma makes up the majority of visible matter in the universe and is a mixture of ionized gas. To create the plasma, a large amount of energy must be injected to overcome the internal atomic attractions and so ionize the material. High power lasers are one way of delivering this energy.

Laser technology has only recently, since the 1980s/1990s, been sufficient to reach conditions labeled as high-energy-density (HED) laboratory physics. Laser facilities such as OMEGA [8], in Rochester, NY, USA; LULI, in Paris, France; Vulcan in Harwell, UK and Gekko XII [9], in Osaka, Japan are capable of producing energy in excess of a kilojoule with multiple beam lines. These laser facilities now make it possible to reproducibly attain the high temperatures, densities and pressures required for HED physics.

Alternative facilities such as MAGPIE [10] at Imperial College London, UK and Sandia National labs [11], NM, USA are pulse power machines that produce a plasma by exploding an array of wires. By re-orienting the wires, different experiments can be performed and so produce astrophysically relevant results.

In particular, magnetic fields have a great influence on the nature of astrophysical events [12, 13]. In astrophysical plasmas, the magnetic field is often frozen into the plasma and so is often dynamically significant. A number of effects arise from these fields. For one, astrophysical shocks often result in turbulent plasmas. If these plasmas are threaded with a weak magnetic field, the action of the plasma to fold

over and twist as the turbulence progresses, the frozen in magnetic field becomes amplified and so reaches dynamically significant levels [14, 15, 16]. This turbulent dynamo mechanism has been widely investigated [17] within simulations but has only recently been demonstrated experimentally [18]. Turbulent astrophysical plasmas are also a hotbed for particle acceleration [19, 20, 21]. Observation of high energy astrophysical particles [22, 23] has led to numerous simulations and theoretical work [21, 24, 13]. One example of particle acceleration is where the Solar-wind interacts with a comet [25]. High energy electrons are produced from this reaction and so generate the observed X-rays. This phenomena has recently been investigated within the laboratory, providing a platform for future investigation into particle acceleration [26].

1.1 Thesis Layout

This thesis is organised to investigate different astrophysical phenomena. Chapter 2 introduces the basic concepts of plasma physics, hydrodynamics, waves in plasmas and plasma diagnostics which are required to describe what is happening in space and in the laboratory.

Chapter 3 describes a recent experiment investigating particle acceleration at the LULI laser facility. A theoretical description of the phenomena, electron acceleration via lower hybrid waves, is given in the context of the Solar-wind interacting with the comet. The experimental setup is then described including the results from the optical diagnostics. A radiative hydrodynamic simulation is then compared with the optical data. Combining results from the X-ray data with particle-in-cell simulations indicates that electron acceleration via lower-hybrid waves was achieved in the experiment and an estimate of the accelerated electron energy is given. This chapter demonstrates the observation of electron acceleration via lower hybrid turbulence within the laboratory.

Chapter 4 describes the setup, calibration and analysis of a Faraday rotation diagnostic that has been implemented at the OMEGA laser facility. This diagnostic allows a time resolved magnetic field measurement to be made. The inferred magnetic field is then compared with the magnetic field determined by proton radiography. This chapter shows that this Faraday rotation diagnostic can accurately measure the magnetic fields within a plasma.

Chapter 5 describes the results from an experiment at the OMEGA laser facility. The experimental campaign aimed to investigate the turbulent dynamo mechanism. This chapter focuses on the results from the Thomson scattering diagnostic which can characterize the flow properties of the plasma. This chapter first describes the experimental campaign as a whole, followed by the effect different plasma parameters have upon the Thomson scattered features. The plasma parameters, as determined from the Thomson scattering diagnostic, are presented to show how the collision of two plasma jets progresses. Next, the effect of the addition of Chlorine to the target foils on the plasma jets is reported. Finally, a theoretical prediction of the effect of Chlorine on the flow properties is presented. This chapter demonstrates how Thomson scattering can be used to characterize the flow properties of two colliding jets.

Finally, chapter 6 summarizes the results of the previous chapters and suggests how the work could be taken further to improve upon current understanding of the phenomena discussed within each chapter.

Chapter 2

Background Theory

This chapter will present an introduction to the necessary plasma physics for the following chapters. Fluid theory, plasma waves and shock theory are first presented. Finally, astrophysical phenomena and plasma diagnostics relevant for the remaining chapters are described.

2.1 Plasma Physics

Plasma is the most common state of visible matter: stars, the interstellar medium and the Solar-wind are all plasmas. A plasma is an ionized gas and this ionized nature gives a plasma unique properties. The ions and electrons can move freely but each individual particle is governed by the local electromagnetic field. This motion leads to quasi-neutrality and collective effects whereby the movement of one particle will cause others to react.

2.1.1 Debye Shielding and the Plasma Frequency

A plasma can screen and reduce electric fields very effectively. The effect of shielding can be investigated [27] by placing a test charge $+Q$ in a plasma with initial electron and ion density n_{e0} and n_{i0} and electron and ion temperature T_e and T_i. The electrons

within the plasma will be attracted to the positive charge and the ions will be repelled. The density of the electrons and ions that are perturbed by this test charge can be described by,

$$n_e(\mathbf{r}) = n_{e0}\exp\left(\frac{e\Phi}{k_B T_e}\right) \quad , \tag{2.1}$$

and

$$n_i(\mathbf{r}) = n_{i0}\exp\left(-\frac{e\Phi}{k_B T_i}\right) \quad . \tag{2.2}$$

Assuming the perturbed potential Φ is small compared to the thermal energy, $|e\Phi| \ll k_B T$, the perturbed density can be expanded in a Taylor expansion. The electric potential can then be obtained by using Poisson's equation, $\nabla^2\Phi = -en/\epsilon_0$,

$$\nabla^2\Phi = -\frac{1}{\epsilon_0}\left[Q\delta(r) - en_{e0}\frac{e\Phi}{k_B T_e} - en_{i0}\frac{e\Phi}{k_B T_i}\right] \quad . \tag{2.3}$$

Assuming quasi-neutrality, $n_{e0} = n_{i0}$, and spherical symmetry,

$$\frac{\partial^2\Phi}{\partial r^2} + \frac{2}{r}\frac{\partial\Phi}{\partial r} - \frac{1}{\lambda_D^2}\Phi = -\frac{Q}{\epsilon_0}\delta(r) \quad . \tag{2.4}$$

The parameter λ_D is a length scale and is defined as,

$$\frac{1}{\lambda_D^2} = \frac{e^2 n_{e0}}{\epsilon_0 k_B T_e} + \frac{e^2 n_{i0}}{\epsilon_0 k_B T_i} \quad . \tag{2.5}$$

The potential Φ is then given by,

$$\Phi(r) = \frac{Q}{4\pi\epsilon_0 r}e^{-\sqrt{2}r/\lambda_D} \quad . \tag{2.6}$$

The parameter λ_D is the Debye shielding length which describes the combined shielding action of electrons and ions. The electric potential around a test charge Q decays exponentially for $r > \lambda_D$. Any deviation from equal densities of electrons and

ions tends to be smoothed by Debye shielding. Therefore a plasma has the tendency to become quasi-neutral.

Debye shielding is an example of collective behaviour from a plasma. Additionally, there is a timescale on which the electrons establish a shielded equilibrium. The heavier ions take longer to reach their equilibrium conditions.

The potential perturbation is small, $|e\Phi| \ll k_B T$, and so the electron velocity is not much changed from its thermal velocity $v_e \approx (k_B T_e/m_e)^{1/2}$. To establish a new equilibrium, the electron must be able to reach its new position at a typical distance λ_{De}. This time can be estimated as $\tau \approx \lambda_{De}/v_{Te}$. The reciprocal of this response time is the electron plasma frequency,

$$\omega_{pe} = \frac{v_{Te}}{\lambda_{De}} = \left(\frac{n_{e0}e^2}{\epsilon_0 m_e}\right)^{1/2} \quad . \tag{2.7}$$

In summary, a plasma of size L must be sufficiently large $L \gg \lambda_D$ and exist for a period of time larger than the response time $\tau \gg \omega_{pe}^{-1}$ to behave in a collective manner.

2.1.2 Collisions

A simplified view of Coulomb collisions can be used to describe electron-ion scattering [27]. The trajectory of an electron in the field of an isolated ion can be described by the Coulomb force. Assuming that the impact factor of the electron, b, is the distance of closest approach of the electron to the ion, then the electron feels an average force,

$$F_C \approx \frac{Ze^2}{4\pi\epsilon_0 b^2} \quad . \tag{2.8}$$

The electron experiences this force for a time $\Delta t \approx 2b/v$ where v is the velocity

of the electron and is assumed to be the time taken for which the force acts then,

$$F_C = m_e \frac{\Delta v}{\Delta t} \quad , \tag{2.9}$$

and so,

$$\frac{Ze^2}{4\pi\epsilon_0 b^2} = m_e \Delta v \frac{v}{2b} \quad . \tag{2.10}$$

The cross section for the collision is a function of the impact parameter and so if an electron has an impact parameter that lies between b and $b + \mathrm{d}b$, the cross section for the collision must be $2\pi b \mathrm{d}b$. The maximum impact parameter is the distance beyond which the Coulomb field is not felt as strongly i.e., the Debye length. The minimum meaningful impact parameter is where the electron encounters a head-on collision and returns back along its original path and so $\Delta v \approx v$ thus giving,

$$b_{min} = \frac{Ze^2}{2\pi\epsilon_0 m v^2} \quad . \tag{2.11}$$

Integrating across all possible impact parameters gives,

$$\frac{\mathrm{d}}{\mathrm{d}t}\left\langle (\Delta v)^2 \right\rangle = \int_{b_{min}}^{b_{max}} 2\pi b n_i v \left(\Delta v\right)^2 \mathrm{d}b = \int_{b_{min}}^{b_{max}} \frac{n_i Z^2 e^4}{2\pi\epsilon_0^2 m_e^2 v} \frac{\mathrm{d}b}{b} = \frac{n_i Z^2 e^4}{2\pi\epsilon_0^2 m_e^2 v} \ln\left(\Lambda\right) \quad . \tag{2.12}$$

where the Coulomb logarithm, $\ln(\Lambda)$, is defined as,

$$\Lambda = \frac{b_{max}}{b_{min}} = \sqrt{\left(\frac{\epsilon_0 k_B T}{n_0 e^2}\right)} \frac{2\pi\epsilon_0 m_e v^2}{Ze^2} \approx \frac{3\pi n_0 \lambda_{De}^3}{Z} \quad , \tag{2.13}$$

which is approximately the number of particles in a Debye sphere.

For a 90^o collision, $(\Delta v)^2 \sim v^2$ giving,

$$\frac{1}{\tau_{ei}} v^2 = \frac{n_i Z^2 e^4}{2\pi \epsilon_0^2 m_e^2 v} \ln(\Lambda) \quad , \tag{2.14}$$

and so the electron-ion collision time is,

$$\tau_{ei} = \frac{2\pi \epsilon_0^2 m_e^2 v^3}{n_i Z^2 e^4 \ln(\Lambda)} \quad . \tag{2.15}$$

This simplified analysis has assumed that the electrons have one velocity, v.

Similarly, electron-electron τ_{ee}, ion-electron τ_{ie} and ion-ion τ_{ii} collision times can be written as [28],

$$\tau_{ee} = \frac{2\pi \epsilon_0^2 m_e^2 v^3}{n_e e^4 \ln(\Lambda)} \quad , \tag{2.16}$$

$$\tau_{ie} = \frac{2\pi \epsilon_0^2 m_i^2 v^3}{n_e Z^2 e^4 \ln(\Lambda)} \quad , \tag{2.17}$$

$$\tau_{ii} = \frac{2\pi \epsilon_0^2 m_i^2 v^3}{n_i Z^4 e^4 \ln(\Lambda)} \quad . \tag{2.18}$$

2.1.3 Resistivity

A cloud of electrons in an electric field, E, will be accelerated by the electric field and decelerated by collisions. In this case, a friction force is described by the electron-ion collision frequency, $\nu_{ei} = 1/\tau_{ei}$. If the electrons have a mean drift velocity v_d much less than the electron thermal velocity $v_{th,e}$ then,

$$\frac{\mathrm{d}}{\mathrm{d}t}(m_e v_d) = -eE - \nu_{ei} m_e v_d \approx 0 \quad , \tag{2.19}$$

and so the current is,

$$j = -n_e e v_d = \frac{n_e e^2 E}{m_e \nu_{ei}} \quad . \tag{2.20}$$

For a conducting medium, the resistivity η can be written as $\eta = E/j$ and so for $v \approx v_{th,e}$,

$$\eta = \frac{Ze^2 \ln\Lambda m^{1/2}}{2\pi\epsilon_0^2 \left(k_B T\right)^{3/2}} \quad . \tag{2.21}$$

Additional transport properties such as charge exchange whereby a moving ion captures an electron and leaves a slow ion behind also add to the elastic scattering to determine the transport properties of a plasma.

2.1.4 Beam Collisions

When a beam of particles passes through a background of particles, the beam can undergo processes such as slowing and transverse spreading.

Following [29], relaxation processes arising from the interaction of test particles, α, streaming with velocity $\mathbf{v}_\alpha$ through a background of field particles, β, can be described through the stopping distance, L_s and the transverse and parallel spreading distances, L_t and L_p, of the test particle beam as,

$$\frac{d\mathbf{v}_\alpha}{dt} = -\nu_s^{\alpha|\beta} \mathbf{v}_\alpha \quad , \tag{2.22}$$

$$\frac{d}{dt}\left(\mathbf{v}_\alpha - \overline{\mathbf{v}}_\alpha\right)_t^2 = \nu_t^{\alpha|\beta} v_\alpha^2 \quad , \tag{2.23}$$

$$\frac{d}{dt}\left(\mathbf{v}_\alpha - \overline{\mathbf{v}}_\alpha\right)_p^2 = \nu_p^{\alpha|\beta} v_\alpha^2 \quad , \tag{2.24}$$

where $v_\alpha = |\mathbf{v}_\alpha|$ and the averages are performed over an ensemble of test particles

and a Maxwellian field particle distribution for the slowing, transverse spreading and parallel spreading of the beam.

Defining $\mu = m_i/m_p$, ionisation Z, Coulomb logarithm $\ln(\Lambda_{\alpha\beta})$, field particle temperature T, test particle energy ϵ and electron density n_e, the interactions can be evaluated [29] for very slow $x^{\alpha|\beta} \ll 1$ and very fast $x^{\alpha|\beta} \gg 1$ test particles where $x^{\alpha|\beta} = m_\beta v_\alpha^2/2k_B T_\beta$ as shown in Table 2.1.

Table 2.1: Expressions for the relaxation rates of different test and field particles given in $\mathrm{cm^3 s^{-1}}$, taken from [29] The temperature and test particle energy are given in eV and the electron density in $\mathrm{cm^{-3}}$ and Λ is the Coulomb logarithm.

Expression	Slow ($x^{\alpha\|\beta} \ll 1$)	Fast ($x^{\alpha\|\beta} \gg 1$)
Electron-electron		
$\nu_S^{e\|e}/n_e \ln(\Lambda)$ $(\mathrm{cm^3 s^{-1}})$	$5.6 \times 10^{-6} T^{-3/2}$	$7.7 \times 10^{-6} \epsilon^{-3/2}$
$\nu_t^{e\|e}/n_e \ln(\Lambda)$ $(\mathrm{cm^3 s^{-1}})$	$5.8 \times 10^{-8} T^{-1/2} \epsilon^{-1}$	$7.7 \times 10^{-6} \epsilon^{-3/2}$
$\nu_p^{e\|e}/n_e \ln(\Lambda)$ $(\mathrm{cm^3 s^{-1}})$	$2.9 \times 10^{-6} T^{-1/2} \epsilon^{-1}$	$3.9 \times 10^{-6} T \epsilon^{-5/2}$
Electron-ion		
$\nu_S^{e\|i}/n_i Z^2 \ln(\Lambda)$ $(\mathrm{cm^3 s^{-1}})$	$0.23 \mu^{3/2} T^{-3/2}$	$3.9 \times 10^{-6} \epsilon^{-3/2}$
$\nu_t^{e\|i}/n_i Z^2 \ln(\Lambda)$ $(\mathrm{cm^3 s^{-1}})$	$2.5 \times 10^{-4} \mu^{1/2} T^{-1/2} \epsilon^{-1}$	$7.7 \times 10^{-6} \epsilon^{-3/2}$
$\nu_p^{e\|i}/n_i Z^2 \ln(\Lambda)$ $(\mathrm{cm^3 s^{-1}})$	$1.2 \times 10^{-4} \mu^{1/2} T^{-1/2} \epsilon^{-1}$	$2.1 \times 10^{-9} \mu^{-1} T \epsilon^{-5/2}$
Ion-electron		
$\nu_S^{i\|e}/n_e Z^2 \ln(\Lambda)$ $(\mathrm{cm^3 s^{-1}})$	$1.6 \times 10^{-9} \mu^{-1} T^{-3/2}$	$1.7 \times 10^{-4} \mu^{1/2} \epsilon^{-3/2}$
$\nu_t^{i\|e}/n_e Z^2 \ln(\Lambda)$ $(\mathrm{cm^3 s^{-1}})$	$3.2 \times 10^{-9} \mu^{-1} T^{-1/2} \epsilon^{-1}$	$1.8 \times 10^{-7} \mu^{-1/2} \epsilon^{-3/2}$
$\nu_p^{i\|e}/n_e Z^2 \ln(\Lambda)$ $(\mathrm{cm^3 s^{-1}})$	$1.6 \times 10^{-9} \mu^{-1} T^{-1/2} \epsilon^{-1}$	$1.7 \times 10^{-4} \mu^{1/2} T \epsilon^{-5/2}$
Ion-ion		
$\nu_S^{i\|i'}/n_i' Z'^2 Z^2 \ln(\Lambda)$ $(\mathrm{cm^3 s^{-1}})$	$6.8 \times 10^{-8} \frac{\mu'^{1/2}}{\mu} \left(1 + \frac{\mu'}{\mu}\right) T^{-3/2}$	$9.0 \times 10^{-8} \left(\frac{1}{\mu} + \frac{1}{\mu'}\right) \frac{\mu^{1/2}}{\epsilon^{3/2}}$
$\nu_t^{i\|i'}/n_i' Z'^2 Z^2 \ln(\Lambda)$ $(\mathrm{cm^3 s^{-1}})$	$1.4 \times 10^{-7} \mu'^{1/2} \mu^{-1} T^{-1/2} \epsilon^{-1}$	$1.8 \times 10^{-7} \mu^{-1/2} \epsilon^{-3/2}$
$\nu_p^{i\|i'}/n_i' Z'^2 Z^2 \ln(\Lambda)$ $(\mathrm{cm^3 s^{-1}})$	$6.8 \times 10^{-8} \mu'^{1/2} \mu^{-1} T^{-1/2} \epsilon^{-1}$	$9.0 \times 10^{-8} \mu^{1/2} \mu'^{-1} T \epsilon^{-5/2}$

These relaxation times can be related to a length scale using the velocity, v_α, of the test particles as $L_y^{\alpha|\beta} = v_\alpha/\nu_y^{\alpha|\beta}$.

2.2 Plasma equations of motion

There are multiple ways to describe the movement of a plasma [30]. A simple description is to start by considering single particle motion. By considering the motion of a charged particle, j, in an externally applied electromagnetic field, the equation

of motion is,

$$m_j \frac{d\mathbf{v}_j}{dt} = q_j \left(\mathbf{E} + \mathbf{v}_j \times \mathbf{B}\right) \quad , \tag{2.25}$$

where m is the particle mass, q is the particle charge, $\mathbf{E}$ is the electric field, $\mathbf{B}$ is the magnetic field and $\mathbf{v}_j$ is the particle velocity where j signifies either electrons, e, or ions, i.

This description allows the individual forces on each particle to be calculated. However, for the large number of particles required to describe a plasma, this description becomes unwieldy and too computationally expensive.

A kinetic description can be used which considers the distributions of particles. Assuming a Boltzmann distribution of particles in an externally applied electromagnetic field, the equation of motion can be written as the Vlasov equation [27],

$$\frac{\partial f_j}{\partial t} + \mathbf{v}_j \cdot \nabla f_j + \frac{q_j}{m_j} \left(\mathbf{E} + \mathbf{v}_j \times \mathbf{B}\right) \cdot \frac{\partial f_j}{\partial \mathbf{v}_j} = 0 \quad , \tag{2.26}$$

where f_j is a function which includes the variation of the number density in space and time and the velocity distribution in each direction, $f_j\left(\mathbf{r}, \mathbf{u}, t\right)$. The Vlasov equation is valid for hot, non-relativistic plasmas where collisions can be neglected.

This form of the equations of motion allows calculations for much larger systems. Often, the movement of individual particles is unknown and so it is useful to consider the entire plasma as a fluid. There are several different fluid descriptions, what follows is a single fluid form which treats the whole plasma as one fluid. The velocity distributions are considered as Maxwellian and so are described by a single temperature.

Fluid Equations

By considering a volume, the rate of mass density, $\rho = mn$, flowing through the surface bounding this volume is the surface integral and flow velocity, $\mathbf{u}$. Using the divergence theorem then gives,

$$\frac{\partial \rho}{\partial t} + \nabla \cdot (\rho \mathbf{u}) = 0 \quad . \tag{2.27}$$

This continuity equation describes the conservation of mass within the system.

The total force acting over the surface of the same volume element is related to the pressure, P. Conservation of momentum then gives,

$$\rho \frac{D\mathbf{u}}{Dt} = -\nabla P \quad , \tag{2.28}$$

where D is the material derivative,

$$\frac{D}{Dt} = \left\{ \frac{\partial}{\partial t} + \mathbf{u} \cdot \nabla \right\} \quad . \tag{2.29}$$

Equation 2.28 only includes pressure as a source term since only a simple fluid is considered here.

The rate of change of energy within the fluid volume gives the conservation of energy. The internal and kinetic energies are treated separately. Using the relation $d\epsilon = TdS - (P/\rho^2)\, d\rho$, where ϵ is the internal energy per unit mass, S is the entropy per unit mass and T is the temperature and combining this with the adiabatic relation $DS/Dt = 0$ and the continuity equation then gives the energy conservation,

$$\frac{\partial}{\partial t}\left(\rho\epsilon + \frac{1}{2}\rho u^2\right) = -\nabla \cdot \left[\rho \mathbf{u}\left(\frac{u^2}{2} + \epsilon\right) + p\mathbf{u}\right] \quad . \tag{2.30}$$

Similarly to the momentum equation, this equation only includes pressure as a source term for energy whereas other terms have to be included in more compli-

cated systems. Assuming an ideal gas equation of state, the conservation of energy, Equation 2.30, can also be written as [28],

$$\frac{DP}{Dt} = -\gamma P \nabla \cdot \mathbf{u} \quad , \tag{2.31}$$

here γ is the adiabatic index and is the ratio of specific heats, $\gamma = C_p/C_v$. Equations 2.27, 2.28 and 2.30 for the Euler equations of hydrodynamics.

2.2.1 Ideal Magnetohydrodynamics

It has been shown that a plasma can be treated as a fluid. However, since a plasma contains charged particles, the fluid equations should be expanded to properly describe the plasma motion [31]. The continuity and energy equations remain unchanged, but the momentum equation requires an additional magnetic term. The electric term can be neglected since the fluid element exhibits the quasi-neutrality of the plasma.

The ideal MHD equations can then be written as

$$\frac{\partial \rho}{\partial t} + \nabla \cdot (\rho \mathbf{u}) = 0 \quad , \tag{2.32}$$

$$\rho \frac{D\mathbf{u}}{Dt} = -\nabla P + \mathbf{J} \times \mathbf{B} \quad , \tag{2.33}$$

$$\frac{DP}{Dt} = -\gamma P \nabla \cdot \mathbf{u} \quad , \tag{2.34}$$

which correspond to the fluid description of the plasma. To close the system, Maxwell's equations are used,

$$\frac{\partial \mathbf{B}}{\partial t} = \nabla \times (\mathbf{u} \times \mathbf{B}) \quad , \tag{2.35}$$

$$\mathbf{J} = \frac{1}{\mu_0}\nabla \times \mathbf{B} \quad , \tag{2.36}$$

where Faraday's equation,

$$\nabla \times \mathbf{E} = -\frac{\partial \mathbf{B}}{\partial t} \quad , \tag{2.37}$$

has been substituted from the generalized Ohm's law [28],

$$\mathbf{E} = -\mathbf{u} \times \mathbf{B} \quad . \tag{2.38}$$

Here, the displacement current has been neglected from quasi-neutrality. The ideal MHD equations are non-relativistic since there is low frequency (velocity) within the system.

The approximations required for the ideal MHD equations to be valid are:

1. Velocities are non-relativistic, to be consistent with quasi-neutrality.

2. Resistivity of the fluid is zero, the fluid is perfectly conducting.

3. Localisation of particles. This can occur as a result of collisions, when the ion mean free path is much smaller than the spatial scale, or magnetic fields, where magnetic entanglement or plasma microfluctuations cause the system to be localised along the field lines, requiring the gyroradius to be much smaller than the spatial scale.

The range over which ideal MHD is able to predict plasma behaviour is remarkably large. In these equations, the plasma is considered to act as one fluid and so a single temperature is assigned to the fluid. Generally strong coupling between the ions and electrons is seen when the collisionality between the two species is high, resulting in both species being the same temperature allowing for a single temperature fluid description to be valid. This also assumes that radiation is not dominant which is true for many systems within the laboratory. Beyond this simple case, it may be

required to treat the plasma as two or more fluids each with distinct temperatures.

Resistive MHD

The ideal MHD equations do not take into account many other effects that can be important in plasma evolution such as heat conduction, fluid viscosity etc. However, arguably, magnetic resistivity is the most frequent deviation from the ideal case that could otherwise be explained fully by the equations above. For a perfectly conducting plasma, the magnetic field lines are frozen into the plasma and so move with the fluid. In many astrophysical settings, the finite diffusivity of the plasma means that, whilst a magnetic field can diffuse out of the plasma, the time it would take for this to happen is far longer than the time scale of the phenomena of interest. Within the laboratory, it can be relied upon that the diffusion time is of the order of the experimental timescale. As such, additional terms need to be included into the ideal equations to take into account the effect of resistivity.

Ohm's law should now be written as $\mathbf{E} + \mathbf{u} \times \mathbf{B} = \rho_E \mathbf{J}$, where ρ_E is the electrical resistivity. The magnetic diffusivity, $\eta_M = \rho_E / \mu_0$ is then included as,

$$\frac{\partial \mathbf{B}}{\partial t} = \nabla \times (\mathbf{u} \times \mathbf{B}) - \nabla \times (\eta_M \nabla \times \mathbf{B}) \quad . \tag{2.39}$$

The first term on the RHS of the above equation represents advection of the magnetic field within the plasma whilst the second term represents the diffusion of the magnetic field through the plasma. The ratio of these terms is given by the magnetic Reynolds number,

$$Re_M = \frac{u_0 \ell_0}{\eta_M} \quad , \tag{2.40}$$

where u_0 and ℓ_0 are typical values of the fluid velocity and length scale within the system. Consequently, if the magnetic Reynolds number in a system is sufficiently

large, advection outweighs diffusion and the ideal equations are recovered. Such characteristic ratios detail the relative importance of different effects within a system and thus are of great importance when considering scaling between laboratory experiments and astrophysical events.

2.3 Electrostatic and Electromagnetic Waves

Electrostatic and electromagnetic waves within a plasma are the font of many plasma properties and instabilities [27, 32]. The dispersion relation for different waves can be found by combining Maxwell's equations to give,

$$\nabla\left(\nabla\cdot\mathbf{E}\right)-\nabla^2\mathbf{E}=-\frac{\partial}{\partial t}\left(\nabla\times\mathbf{B}\right)=-\frac{\partial}{\partial t}\left(\mu_0\mathbf{J}+\mu_0\epsilon_0\frac{\partial\mathbf{E}}{\partial t}\right) \quad . \tag{2.41}$$

Assuming that the electric field is oscillatory, $\mathbf{E}\left(\mathbf{k},\omega\right)=\mathbf{E_0}\exp\left[i\left(\mathbf{k}\cdot\mathbf{x}-\omega t\right)\right]$, Equation 2.41 can then be written as,

$$c^2\mathbf{k}\left(\mathbf{k}\cdot\mathbf{E}\right)-c^2k^2\mathbf{E}=\omega^2\left(1-\frac{i\sigma}{\epsilon_0\omega}\right)\mathbf{E} \quad . \tag{2.42}$$

2.3.1 Waves in a warm non-magnetized plasma

Langmuir Waves

When the electron species has a finite temperature, the pressure can no longer be neglected and $\nabla P_e=\gamma_e k_B T_e$. This change in pressure can be added to the conservation of momentum as,

$$m_e n_e\left[\frac{\mathrm{d}\mathbf{v}}{\mathrm{d}t}+\left(\mathbf{v}\cdot\nabla\mathbf{v}\right)\right]=-en_e\mathbf{E}-\nabla P_e \quad . \tag{2.43}$$

Assuming that each of these quantities, x, are oscillating around some constant

part x_0, such that $x = x_0 + x_1$ and that the oscillations are harmonic then leads to,

$$-i\omega m_e n_0 u_1 = -e n_0 E_1 - ikP_1 \quad , \tag{2.44}$$

where quantities $x_1 y_1$ are considered negligible.

The continuity equation becomes,

$$-i\omega n_1 + ikn_0 u_1 = 0 \quad , \tag{2.45}$$

and Gauss' law, $\nabla \cdot E = \rho/\epsilon_0$, can be written as

$$ik\epsilon_0 E_1 = -en_1 \quad . \tag{2.46}$$

Assuming that the electron compression occurs one-dimensionally and faster than thermal conduction, $\gamma = 3$. This then gives a dispersion relation of,

$$\omega^2 = \omega_{pe}^2 + \gamma_e k^2 v_{th,e}^2 \quad . \tag{2.47}$$

This is the Bohm-Gross dispersion relation. The waves associated with this dispersion relation are Langmuir waves. The propagation is possible because in addition to the restoring electric field, which is responsible for the plasma frequency, there is now an added pressure term which accelerates the high density regions back to their equilibrium locations. This added energy causes the electrons to overshoot the ions by an even greater distance and thus continue propagating forward through the plasma.

Landau Damping

Landau damping is the effect of damping of longitudinal waves in a plasma [33, 28]. Landau damping occurs because of the energy exchange between an electromagnetic wave and particles in the plasma with a velocity similar to that of the

phase velocity. Those particles that have velocities less than the phase velocity will be accelerated by the wave whilst those particles with velocities slightly greater than the wave's phase velocity will be decelerated and lose energy to the wave.

Ion acoustic waves

Waves can also propagate through the ion species, although the timescales are generally much larger due to the greater mass. Since the timescale applicable to ion motions is far greater than that for electrons, instead of using Poisson's equation, the approximation of $n_e = n_i$ due to Debye shielding can be made. Since the electrons are so light, the electric field is related only to the electron motion such that $n_e e\mathbf{E} = -k_B T_e \nabla n_e$ whilst the pressure of the ions is $\nabla P_i = \gamma_i k_B T_i$. The conservation of momentum is then given by,

$$m_i n_i \left[\frac{\partial \mathbf{v}_i}{\partial t} + (\mathbf{v}_i \cdot \nabla)\, \mathbf{v}_i \right] = -e n_i Z E - \nabla P_i \quad , \tag{2.48}$$

where Z is the ionization of the ions.

Using a similar method to before, the dispersion relation is then found to be,

$$\frac{\omega}{k} = \sqrt{\left(\frac{k_B T_e + \gamma_i k_B T_i}{m_i} \right)} \quad . \tag{2.49}$$

This is the dispersion relation for ion acoustic waves, traveling at a fixed sound speed. These waves have regions of compression and rarefaction. The ions will primarily spread out due to their thermal distribution. There is also rarefaction caused by the ions' positive charges repelling one another. If Poisson's equation were used instead [27], the full dispersion relation would be given as,

$$\frac{\omega}{k} = \sqrt{\left(\frac{k_B T_e}{m_i} \frac{1}{1 + k^2 \lambda_{De}^2} + \frac{\gamma_i k_B T_i}{m_i} \right)} \quad . \tag{2.50}$$

This correction is minor for all ion acoustic waves except for those with wave-

lengths smaller than the Debye length where single particle interactions are important.

2.3.2 Waves in a cold magnetized plasma

When considering magnetized waves, the conductivity should be described as a tensor [28]. The conductivity tensor is defined as $\mathbf{J} = \sigma \cdot \mathbf{E}$. The dielectric response is then described as,

$$\epsilon = \mathbf{I} - \frac{i}{\epsilon_0 \omega}\sigma \quad . \tag{2.51}$$

The equations of motion can be used to describe the full expression for the dielectric tensor as,

$$\epsilon = \begin{pmatrix} \epsilon_1 & -i\epsilon_2 & 0 \\ i\epsilon_2 & \epsilon_1 & 0 \\ 0 & 0 & \epsilon_3 \end{pmatrix} \quad , \tag{2.52}$$

where,

$$\epsilon_1 = 1 + \frac{\omega_{pe}^2}{\omega_{ce}^2 - \omega^2} + \frac{\omega_{pi}^2}{\omega_{ci}^2 - \omega^2} \quad , \tag{2.53}$$

$$\epsilon_2 = \frac{\omega_{ce}}{\omega}\frac{\omega_{pe}^2}{\omega_{ce}^2 - \omega^2} + \frac{\omega_{ci}}{\omega}\frac{\omega_{pi}^2}{\omega_{ci}^2 - \omega^2} \quad , \tag{2.54}$$

$$\epsilon_3 = 1 - \frac{\omega_{pe}^2}{\omega^2} - \frac{\omega_{pi}^2}{\omega^2} \quad , \tag{2.55}$$

and $\omega_{pi} = \sqrt{m_e/m_i}\omega_{pe}$ is the ion plasma frequency and $\omega_{ce} = eB_0/m_e$ and $\omega_{ci} = ZeB/m_i$ are the electron and ion cyclotron frequencies for an external magnetic field, $\mathbf{B_0}$, with magnitude B_0.

Defining $S = \frac{1}{2}(R + L)$ and $D = \frac{1}{2}(R - L)$ where,

$$R = 1 - \frac{\omega_{pe}^2}{\omega(\omega + \omega_{ce})} - \frac{\omega_{pi}^2}{\omega(\omega + \omega_{ci})} \quad , \tag{2.56}$$

and,

$$L = 1 - \frac{\omega_{pe}^2}{\omega(\omega - \omega_{ce})} - \frac{\omega_{pi}^2}{\omega(\omega - \omega_{ci})} \quad , \tag{2.57}$$

the dispersion relation can be readily determined. From Equation 2.42 the equation for electromagnetic waves can be written as $\mathbf{M} \cdot \mathbf{E} = 0$ where,

$$\mathbf{M} = \frac{\omega^2}{c^2}\epsilon + \mathbf{kk} - k^2\mathbf{I} \quad . \tag{2.58}$$

Defining $\mathbf{N} = c\mathbf{k}/\omega$, the above equation can be solved by finding and setting to zero the determinant of $\mathbf{M}$. Choosing convenient axes such that $k_y = N_y = 0$ and θ the angle between $\mathbf{k}$ and $\mathbf{B_0}$ then,

$$AN^4 - BN^2 + C = 0 \quad , \tag{2.59}$$

where,

$$A = S\sin^2\theta + P\cos^2\theta \quad , \tag{2.60}$$

$$B = RL\sin^2\theta + PS\left(1 + \cos^2\theta\right) \quad , \tag{2.61}$$

$$C = PRL \quad , \tag{2.62}$$

where,

$$P = 1 - \frac{\omega_{pe}^2}{\omega^2} - \frac{\omega_{pi}^2}{\omega^2} \quad . \tag{2.63}$$

The solutions are then $N^2 = (B \pm F)/2A$ where,

$$F^2 = (RL - PS)^2 \sin^4\theta + 4P^2D^2\cos^2\theta \quad . \tag{2.64}$$

F^2 is positive and so N^2 is real and so there is no evanescent wave for a cold plasma.

The solutions can also be written as,

$$\tan^2\theta = -\frac{P(N^2 - R)(N^2 - L)}{(SN^2 - RL)(N^2 - P)} \quad . \tag{2.65}$$

This equation then makes it simple to identify propagation parallel and perpendicular to the magnetic field $\mathbf{B_0}$. Parallel propagation occurs when $P = 0$, $N^2 = R$ and $N^2 = L$. Perpendicular propagation occurs at $N^2 = RL/S$ and $N^2 = P$.

Hybrid resonance

For perpendicular propagation $N^2 = RL/S$. Resonance occurs when the denominator is zero and so,

$$1 - \frac{\omega_{pe}^2}{2\omega(\omega + \omega_{ce})} - \frac{\omega_{pi}^2}{2\omega(\omega + \omega_{ci})} - \frac{\omega_{pe}^2}{2\omega(\omega - \omega_{ce})} - \frac{\omega_{pi}^2}{2\omega(\omega - \omega_{ci})} = 0 \quad . \tag{2.66}$$

The solution to this equation then gives the upper-hybrid wave,

$$\omega_{UH}^2 = \omega_{pe}^2 + \omega_{ce}^2 \quad , \tag{2.67}$$

and the lower-hybrid wave,

$$\omega_{LH}^2 = \frac{\omega_{ce}\omega_{ci}}{\left(1+\frac{\omega_{ce}^2}{\omega_{pe}^2}\right)} \quad . \tag{2.68}$$

For a warm plasma with a quasi-perpendicular magnetic field ($k_\perp/k_\parallel \approx \sqrt{m_i/m_e}$), the full dispersion relation for lower-hybrid waves can be found in Ref. [34]. Lower-hybrid waves will be discussed further in Chapter 3.

Faraday-rotation

For waves traveling parallel to a magnetic field, there are two possible solutions, $N^2 = R, L$, with refractive indices given by,

$$N^2 = \frac{c^2k^2}{\omega^2} = 1 - \frac{\omega_{pe}^2}{\omega\left(\omega \pm \omega_{ce}\right)} \quad , \tag{2.69}$$

when neglecting the ion dynamics. These are the right-hand and left-hand polarized waves. The refractive index can be approximated as,

$$N_\pm \approx 1 - \frac{\omega_{pe}^2}{2\omega^2}\left(1 - \pm\frac{\omega_{ce}}{\omega}\right) \quad . \tag{2.70}$$

Linearly polarized light can then be constructed by summing the two circularly polarized components. The electric field can then be written as,

$$E_{x,Linear} = E_0\left[\cos\left(\frac{\omega}{c}\left(N_+ z - ct\right)\right) + \cos\left(\frac{\omega}{c}\left(N_- z - ct\right)\right)\right] \quad , \tag{2.71}$$

and,

$$E_{y,Linear} = E_0\left[\sin\left(\frac{\omega}{c}\left(N_+ z - ct\right)\right) - \sin\left(\frac{\omega}{c}\left(N_- z - ct\right)\right)\right] \quad . \tag{2.72}$$

Defining $\tan\phi = E_{y,Linear}/E_{x,Linear}$ gives,

$$\phi = \frac{\omega}{2c}\left(N_+ - N_-\right) z \quad . \tag{2.73}$$

The difference between the two refractive indices is,

$$N_+ - N_- = \frac{\omega_{pe}^2 \omega_{ce}}{\omega^3} \quad , \tag{2.74}$$

and so,

$$\phi = \left(\frac{n_e e^2}{\epsilon_0 m_e}\right) \frac{eB}{m_e} \frac{1}{2c\omega^2} z = \frac{e^3 n_e B}{8\pi^2 \epsilon_0 m_e^2 c^3} \lambda^2 z \quad . \tag{2.75}$$

The rotation therefore depends on the electron density, magnetic field and length through which the radiation will have traveled.

Faraday-rotation can be used to measure the magnetic field in space or in the laboratory. In space, the electron density can be measured by absorption spectroscopy; the length through which the radiation has traveled is measured by the dispersion of the radio waves from the pulsar and so by measuring the angle as a function wavelength the amount of rotation can be found and so the magnetic field determined [35].

2.4 Shocks

Shocks are common throughout astrophysics and arise in numerous environments such as the Earth's bow shock [36], supernova remnants [13] and galaxy clusters [37]. The main difference between astrophysical shocks and shocks in a more familiar setting such as in a gas, is that astrophysical shocks are collisionless. In a normal gas, the collisions ensure that the constituent particles all have the same temperature and also provide the mechanism to propagate pressure and temperature

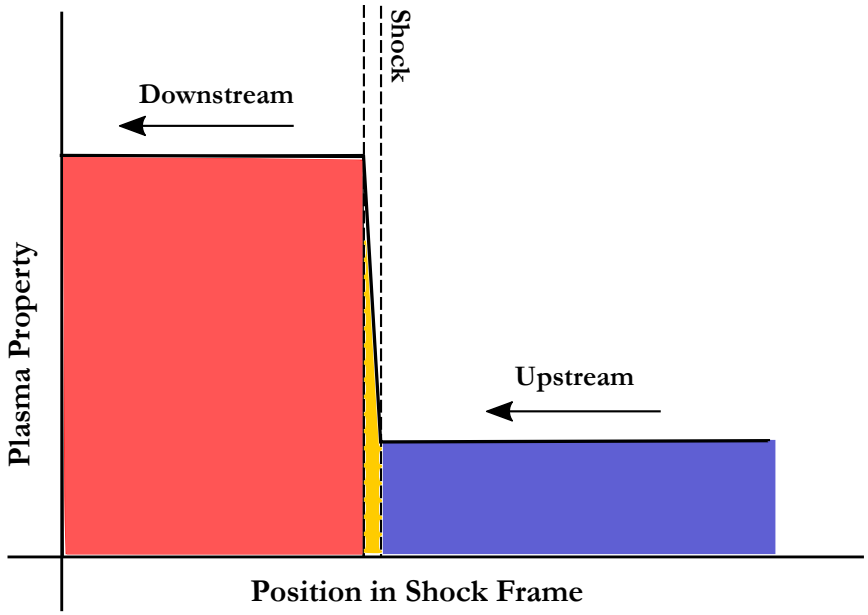

Figure 2.1: Shock illustration: Schematic of a shock adapted from [43] depicting how the plasma properties change across the shock.

changes. The collisions in a gas also allow for dissipation in the form of viscosity. In collisionless shocks, the lack of collisions means that collisionless shocks require a different dissipation mechanism [38] compared with collisional shocks. These dissipation mechanisms are often mediated by electromagnetic forces and often result in heating, particle acceleration and the formation of instabilities [39, 40, 41, 42].

A shock is defined as a sudden change in fluid properties across a narrow transition region as shown in Figure 2.1. The density and temperature jump across a shock front have very different properties upstream and downstream of the shock. Upstream of the shock, the fluid has no warning of the incoming shock since the shock travels faster than the sound speed in the unshocked upstream material. Generally materials dissipate energy by forming sound waves, however the amount of pressure that can be sustained by the material is limited by the sound speed of the material. If more energy is introduced to the material than the fluid can dissipate as a sound wave, a shock is formed instead [43]. This energy can be introduced to the fluid through, for instance, a laser pulse.

2.4.1 Jump conditions

Whilst the fluid properties upstream and downstream of the shock can vary considerably, both sides still have to obey mass, momentum and energy conservation laws. Beginning with the hydrodynamic equations of motion for a fluid and a plane parallel, steady-state disturbance (i.e., in the x-direction only and $\frac{\partial}{\partial t} = 0$). Conservation of mass, momentum and energy then gives the following equations:

$$\frac{d}{dx}(\rho u) = 0 \quad , \tag{2.76}$$

$$u\frac{du}{dx} = -\frac{1}{\rho}\frac{dP}{dx} \quad , \tag{2.77}$$

$$\frac{d}{dx}\left[\rho u\left(\frac{1}{2}u^2 + \epsilon\right)\right] = -\frac{d(Pu)}{dx} \quad . \tag{2.78}$$

Integrating across the discontinuity where $x_1 < x_s < x_2$ and x_s is the shock position and the subscripts $1, 2$ refer to the pre- and post-shock properties respectively, gives,

$$[\rho u]_{x_1}^{x^2} = 0 \;\rightarrow\; \rho_1 u_1 = \rho_2 u_2 \quad , \tag{2.79}$$

$$\left[\rho u^2 + P\right]_{x_1}^{x_2} = 0 \;\rightarrow\; \rho_1 u_1^2 + P_1 = \rho_2 u_2^2 + P_2 \quad , \tag{2.80}$$

$$\left[\rho u\left(\frac{1}{2}u^2 + \epsilon\right) + Pu\right]_{x_1}^{x_2} = 0 \;\rightarrow\; \rho_1 u_1\left(\frac{1}{2}u_1^2 + \epsilon_1\right) + P_1 u_1 = \rho_2 u_2\left(\frac{1}{2}u_2^2 + \epsilon_2\right) + P_2 u_2 \quad , \tag{2.81}$$

where the simplification $d/dx\,(\rho u^2) = \rho u du/dx$ has been made with the requirement $\rho u \neq 0$. Under these assumptions the shock width is infinitesimally narrow,

in reality this is not true and the width is affected by a number of factors including viscosity and radiation. These effects generally only become important at or near the shock front and so these equations are valid as long as we look at the shocked and unshocked regions far from the shock front.

2.5 Astrophysical Plasmas

Many of the phenomena arising in astrophysical plasmas can be investigated within the laboratory. Recent experimental campaigns have investigated collisionless shocks [44], accretion columns in a binary star [45] and Rayleigh-Taylor formation at a supernova [46]. The phenomena of most interest to this work is particle acceleration by diffusive shock acceleration, and magnetic field amplification by the turbulent dynamo mechanism.

2.5.1 Diffusive Shock Acceleration

Particle acceleration is known to occur at astrophysical shocks [47, 48]. It is generally considered that diffusive shock acceleration (DSA) can account for these observations of non-thermal particles. DSA is based on Fermi acceleration [49]. In Fermi acceleration, charged particles gain energy through random scattering events with magnetized clouds that move with average speed u. The particles will lose or gain energy depending on whether they encounter a head-on or overtaking collision. Since head-on collisions are more likely, the particles receive an overall gain in energy of $\sim (u/c)^2$. The scattering medium can be a turbulent magnetized plasma or a turbulent wave spectrum [50, 51]. Since $u \ll c$, the particle acceleration is generally slow. However, since there is turbulence present throughout the universe, this process occurs almost everywhere in the interstellar medium and intergalactic medium. A more efficient mechanism was suggested by Fermi [19] whereby the scattering clouds are

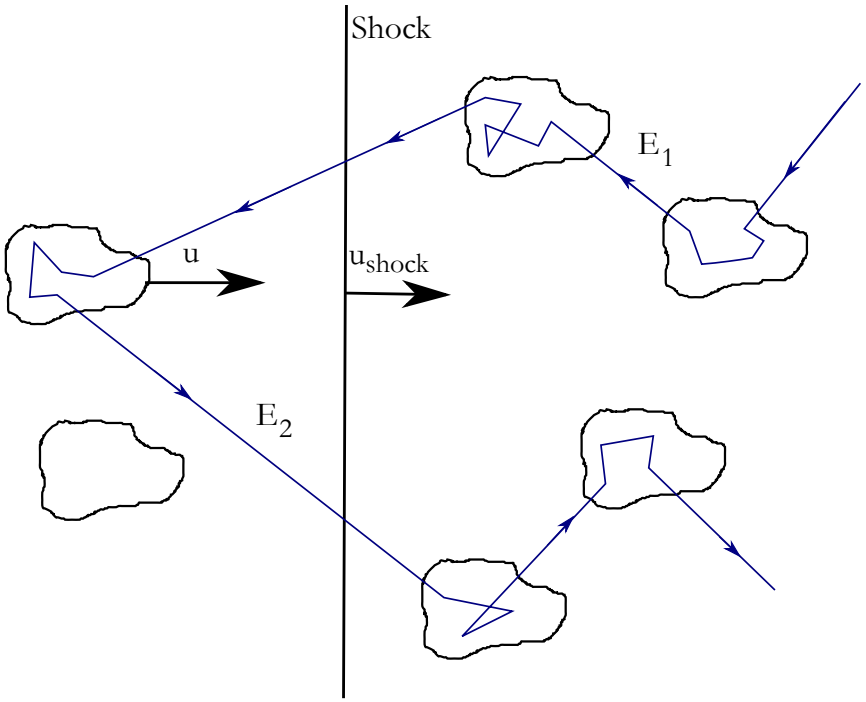

Figure 2.2: DSA: Schematic adapted from [22] shows a particle scattering off of magnetized clouds and so being accelerated across the shock front.

converging and so the particle will gain energy upon every collision resulting in an acceleration $\sim u/c$.

It was later suggested that shock waves provide the ideal environment for this process [52] as shown in Figure 2.2. However, for DSA to effectively accelerate particles, the particles themselves must already have large velocities that permit multiple shock crossings. As such, an initial acceleration mechanism is required to energize the particles in-situ. This is known as the injection problem [53] and will be discussed further in Chapter 3.

2.5.2 Turbulent Dynamo Mechanism

The MHD equation for the magnetic field evolution, including diffusion, does not include a term for magnetic field generation. There are a number of mechanisms that can generate magnetic fields, one of which is the Biermann battery mechanism which requires misaligned density and temperature gradients [54]. Having generated

these seed fields [55], they can then become amplified through a dynamo mechanism [12, 56, 57].

Biermann Battery

The thermally generated electric field is found from balancing the forces on the electrons due to the pressure gradient and the electric field.

Inserting the electric field,

$$m_e \frac{\mathrm{d}\mathbf{v}}{\mathrm{d}t} = -e\mathbf{E} - \frac{\nabla P_e}{n_e} = 0 \quad , \tag{2.82}$$

into Faraday's law gives,

$$\frac{\partial \mathbf{B}}{\partial t} = \frac{k_B}{n_e e} \nabla n_e \times \nabla T_e \quad . \tag{2.83}$$

Therefore there is a source term which is only non-zero if the density and temperature gradients are misaligned to one another. Astrophysically this can arise in a number of ways such as from asymmetrical shocks [55].

This Biermann battery mechanism [54] operates at small scales to produce seed fields. Through dynamo action, the magnetic field is amplified to large values.

Turbulent Plasmas

A turbulent flow with a high Reynolds number can be considered to consist of eddies of different sizes [58]. These eddies are considered to be a turbulent motion that is moderately coherent within that region. The large eddies are unstable and break up, transferring their energy to the smaller eddies. These smaller eddies undergo a similar process and so an energy cascade transfers energy to smaller and smaller scales until the eddy motion is stable and is effective in dissipating the kinetic energy. At these small scales, the kinetic energy is converted into heat. To determine how the

turbulent kinetic energy is distributed amongst the eddies at different wavenumbers, k, the kinetic energy spectrum, $E(k)$, can be considered. Following Ref. [59], a Kolmogorov spectrum of $E(k) \sim k^{-5/3}$ can be determined for high Reynolds number fluids.

Fluctuation Dynamos

In a conducting medium, magnetic fields can be amplified by the inductive effects associated with the motions of the medium [17, 60, 61]. In this dynamo mechanism, kinetic energy is transferred into magnetic energy. Since astrophysical plasmas are often turbulent, this is often referred to as a turbulent dynamo [62, 63]. Turbulent dynamos can be split into fluctuation (small-scale) and mean-field (large-scale) dynamos. The fluctuation dynamo produces magnetic fields that are correlated only on scales of the order of or smaller than the energy carrying scale of the random motions.

Fluctuation dynamos are generic in any random flow where R_m exceeds a critical value $R_{m,cr} \sim 100$ [17]. A magnetic field line frozen into such a fluid will then be extended by the random stretching. For a nearly incompressible fluid, any random shearing motion will increase the length of a fluid element and so also amplify the magnetic field, due to flux freezing.

As the field strength increases, the rate of Ohmic dissipation increases until it compensates the effect of random stretching. In the kinematic regime, the field grows exponentially roughly on the eddy turnover time ℓ_0/u_0 where ℓ_0 and u_0 are typical length and velocity scales of the plasma.

Whilst the turbulent dynamo mechanism has been postulated for astrophysical plasmas, it has been difficult to replicate within the laboratory. A laboratory realisation of the turbulent dynamo mechanism is discussed further in chapter 5.

2.6 Laser-target interaction

To attain the high temperature and pressure regimes encountered astrophysically within the laboratory, a large amount of energy is required. High power lasers are one such way of delivering the required energy to overcome the material's internal attractions and so ionise the material [64].

When a high power laser is incident on a target, the substance removed from the condensed target surface ionizes to form a plasma cloud. This cloud is also referred to as the laser plasma corona. The dominant mechanism for this ionization for laser intensities $\leq 10^{15}$ W/cm^2 is through collisional absorption [28, 65], also known as inverse Bremsstrahlung. Whilst the laser pulse is incident upon the neutral atoms, its electric field causes the electrons to accelerate. These free electrons oscillate and will collide with the ions, transferring energy from the laser pulse to the particles. This leads to heating of the target and so, eventually, the bound electrons are released. These newly freed electrons can then also oscillate with the laser field and so transfer more energy to the neutral atoms, leading to avalanche ionization.

At high intensities, other forms of ionization can take place [30]. The electric field of a high-intensity laser pulse acts to lower the barrier energy trapping the bound electrons. By lowering one side of the potential, energies below the typical ionization will now allow escape via quantum tunneling, thus leading to tunnel ionization. This is different to multi-photon ionization whereby multiple photons are simultaneously absorbed by a bound electron to escape the potential well. Here, for a high enough frequency laser, fewer photons are required to ionize the atoms and so increases the likelihood of ionization. Consequently, multi-photon ionization is most likely to occur at high laser intensities when the laser has a large frequency.

The laser generated plasma is normally opaque to the radiation since the absorption takes place inside the corona, near the critical surface. The critical surface is so-called since the electron density at this surface is equal to the critical value

whereby the plasma frequency is equal to the laser radiation frequency.

The heat absorbed at the critical surface is transported by thermal conduction to the target surface, termed the ablation front [64]. The solid density substance begins to heat up at this front, its density lowers, and a new portion of the substance is delivered to the flow from the target to the corona. This portion reaches the critical surface, crosses it and continues its expansion in vacuum.

The hot plasma pressure ahead of the ablation front is transferred to the solid-state density substance behind the ablation front. It is the corona pressure that drives the flow in the target. For a thick target, the coronal pressure sustains the shock wave traveling into the target interior. The pressure gradient in the dense substance beyond the ablation front accelerates the target substance.

In this manner, a high power laser can generate a fast flowing, hot plasma within the laboratory.

2.7 Plasma Diagnostics

There are numerous diagnostics for measuring different properties of a laser produced plasma. There are several standard techniques to measure the temperature, density and flow velocity of the plasma which then allows an array of plasma properties to be determined. Whilst these quantities are generally inferred from separate diagnostics, for particular plasmas Thomson scattering [66] can provide values for several of these quantities in one measurement.

In many plasma experiments, it is useful to measure the magnetic field. There are multiple techniques for making magnetic field measurements, including through Faraday rotation. Chapter 4 discusses how a Faraday rotation diagnostic is utilised at the OMEGA laser facility.

Two standard techniques for measuring electron density and temperature will now be described.

2.7.1 Interferometry

Interferometry can be used to infer the electron density of a plasma [67].

A Mach-Zender interferometer involves a laser being split into two optical paths, one goes through the plasma and the other, a reference beam, passes through the vacuum in the target chamber. The two beams are then recombined where they interfere with one another before being imaged onto a CCD camera. If no plasma is present, the resultant fringes appear as straight lines. If there is a plasma, the refractive index along one path is different and so the relative phase of the wavefronts are shifted causing them to interfere at different spots and leading to a distortion in the fringe pattern. The phase distortions can be translated back into changes in refractive index and so give a measurement of the plasma's electron density.

In an experimental system, imperfections will result in phase shifts even when there is no plasma present and so a background reference interferogram is subtracted from the data to minimize imperfections. To retrieve the phase shifts, a Fourier transform technique can be used. A Fourier transform technique uses a carrier frequency to separate the zero-order background and the frequency of the fringes. The first order spectrum, the fringe frequency, carries the phase information. To retrieve solely the frequency information, a Fourier transform is made and everything except for the first order portion of the spectrum is filtered out.

To recover the true phase, the interferogram must be unwrapped such that the total phase difference has no discontinuities. The unwrapped phase map, s, can be related to electron density through [67],

$$s = \left[\frac{\Delta\left(N-1\right)}{\lambda}\right] L \quad , \tag{2.84}$$

where $\Delta\left(N-1\right)$ is the change in refractivity, λ is the wavelength of the probe laser and L is the path length through the plasma.

The refractivity for a plasma which has a probe beam frequency greater than electron-ion collision frequency,

$$(N-1) = -\frac{1}{2}\frac{\omega_{pe}^2}{\omega^2} \sim \lambda^2 n_e \quad . \tag{2.85}$$

Consequently the unwrapped phase difference map can be multiplied by a constant factor to obtain an electron density.

This phase extraction can be carried out using the Interferometric Data Evaluation Algorithms (IDEA) software.

2.7.2 Optical spectroscopy

Emission spectra are generated by spontaneous emission of photons due to electron transitions within an atom. The distribution of the energy levels within the atom are therefore dependent on the electron temperature. In equilibrium, the Saha-Boltzmann distribution can relate the intensities of two different spectral lines to the electron temperature of the plasma through [68, 69],

$$\frac{\epsilon_z\left(p \to q\right)}{\epsilon_z\left(p' \to q'\right)} = \frac{\lambda_{p'q'} A_z\left(p \to q\right) g_z\left(p\right)}{\lambda_{pq} A_z\left(p' \to q'\right) g_z\left(p'\right)} \exp\left[-\frac{E_z\left(p\right) - E_z\left(p'\right)}{k_B T_e}\right] \quad , \tag{2.86}$$

where ϵ_z is the emission coefficient for ionization state z, λ_{pq} and $\lambda_{p'q'}$ are the wavelengths under comparison, A_z is the Einstein coefficient of spontaneous emission, $g\left(p\right)$ is the statistical weight of the upper energy level in the transition, $E(p)$ is the energy of the upper level in the transition and T_e is the electron temperature.

By taking line ratios, an absolute calibration of the spectrometer is not required. The line ratios require sufficiently different lines in energy or electron scattering cross section. None of the emission lines will be infinitely sharp and will be broadened in some manner by the plasma.

If an absolute calibration of the spectrometer is performed with a white light source, the absolute emission can be fitted instead as,

$$\epsilon\left(p \rightarrow q\right) = \frac{h\nu_{pq} A_z\left(p \rightarrow q\right)}{4\pi n_z} \frac{g_z\left(p\right)}{U_z\left(T_e\right)} \exp\left[-\frac{h\nu_{pq}}{k_B T_e}\right] \quad , \tag{2.87}$$

where n_z is the density, ν_{pq} is the frequency of the emitted photon and $U_z\left(T_e\right)$ is the partition function of ionizing stage z is given by,

$$U_z\left(T\right) = \sum_{i=g}^{\infty} g_z\left(i\right) \exp\left[-\frac{E_z\left(i\right) - E_z\left(g\right)}{k_B T}\right] \quad , \tag{2.88}$$

where i is the ionization state and g is the ground state. An absolute calibration makes it possible to find the electron temperature and, potentially, density.

The collisional-radiative code PrismSPECT can be used to fit an optical emission spectra to obtain the correct electron temperature and density.

2.7.3 Xray spectroscopy

When an electron from the inner shell of an atom is excited, once it returns to a lower level the energy which it previously gained is emitted by a photon. Atoms can be excited by high energy charged particles such as electrons.

A crystal can be used as a wavelength dispersive X-ray spectrometer, which diffracts the X-rays according to Bragg's law which can be detected on, for instance, an image plate.

In a von-Hamos geometry, the X-ray fluorescence from the sample is diffracted by a cylindrically bent crystal [70, 71]. On the detector plane, the diffracted X-rays create a 2D image. On the dispersion axis, the position of the detected X-rays is correlated to the X-ray energy. The energy range of the detected X-rays is correlated to the length of the crystal and the detector. The bending of the crystal enhances the efficiency of the instrument by providing focusing in the non-dispersion plane.

The non-dispersion axis indicates the spatial variation of the X-rays.

The main factors influencing the energy resolution and efficiency of the spectrometer are the bending radius of the crystal, source size and spatial resolution of the detector in the dispersion plane.

2.7.4 Thomson Scattering

Thomson scattering is a process by which incident electromagnetic radiation accelerates a charged particle and the particle re-emits radiation in response to being accelerated [66]. Thomson scattering is the limiting case of Compton scattering for low frequency. The process of photon re-emission can be described by accelerating charges.

To describe the shape of the Thomson scattered signal and position of the resonances, the theory can be followed in [72]. First, to describe the radiation produced by a moving charge, Maxwell's equations can be combined to give, in cgs units,

$$\nabla \times (\nabla \times \mathbf{E}) + \frac{1}{c^2}\frac{\partial^2 \mathbf{E}}{\partial t^2} = \frac{4\pi}{c}\frac{\partial \mathbf{J}}{\partial t} \quad . \tag{2.89}$$

The electric field $\mathbf{E}$ and current density $\mathbf{J} = q\mathbf{v}(t')$ for a single charge, q, needs to be determined. The behaviour of the electric field at a distance R from the charge and time t can be related to the retarded time, t', where,

$$t' = t - R'/c \quad . \tag{2.90}$$

Equation 2.89 can be solved [73] to give,

$$\mathbf{E}(\mathbf{r}, t) = q \left\{ \frac{(\hat{\mathbf{s}} - \beta)(1 - \beta^2)}{(1 - \hat{\mathbf{s}} \cdot \beta)^3 \mathbf{R}'^2} + \frac{\hat{\mathbf{s}} \times \left[(\hat{\mathbf{s}} - \beta) \times \dot{\beta}\right]}{c(1 - \hat{\mathbf{s}} \cdot \beta)^3 \mathbf{R}'} \right\}_{ret} \quad , \tag{2.91}$$

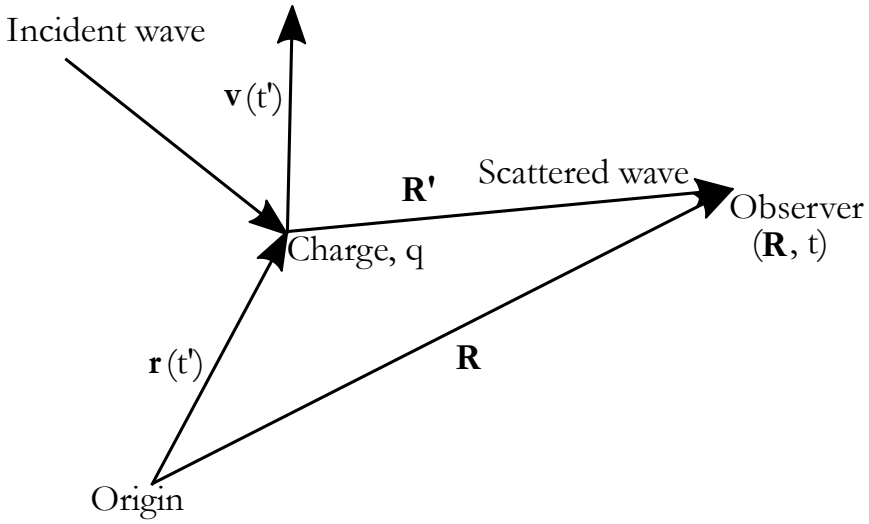

Figure 2.3: Thomson scattering co-ordinate system, adapted from [72].

and the corresponding magnetic field, $\mathbf{B}$, is,

$$\mathbf{B}\left(\mathbf{R}', t\right) = \mathbf{n}\left(\hat{\mathbf{s}} \times \mathbf{E}\right) \quad , \tag{2.92}$$

where $\beta = \mathbf{v}/c$, $\hat{\mathbf{s}}$ is the unit vector pointing from the charge to the observer and $\mathbf{n} = c\mathbf{k}/\omega$.

In scattering experiments, the condition $R' \gg L$ is normally made whereby the observing point is at a large distance from the charge compared to the characteristic length, L, over which the motion of the charge is observed. The first term in Equation 2.91 is therefore dropped in all following calculations and the approximation $R' \approx R$.

The measured property in a scattering experiment is the scattered power. The scattered power, P_s, per unit solid angle, Ω, is given by,

$$\frac{dP_s}{d\Omega} = R^2 \mathbf{S} \cdot \hat{\mathbf{s}} \quad , \tag{2.93}$$

where $\mathbf{S} = \frac{c}{4\pi}\mathbf{E} \times \mathbf{B}$ is the Poynting vector. This then gives,

$$\frac{dP_s}{d\Omega} = \frac{R^2 c}{4\pi} E_s^2 \quad . \tag{2.94}$$

For low-velocity charges, the magnetic field can be neglected and the scattered electric field, E_s, can be written as,

$$\mathbf{E}_s\left(R,t\right)=\frac{q}{cR}\left[\hat{\mathbf{s}}\times\left(\hat{\mathbf{s}}\times\dot{\beta}\right)\right]_{ret} \quad . \tag{2.95}$$

The scattered power per unit solid angle is then written as,

$$\frac{dP_s}{d\Omega}=\frac{q^2}{4\pi c}\left[\hat{\mathbf{s}}\times\left(\hat{\mathbf{s}}\times\dot{\beta}\right)\right]^2 \quad . \tag{2.96}$$

To determine the orbit of the charge, the influence of the electromagnetic wave is neglected and the unperturbed orbit is simply $\mathbf{r}\left(t'\right)=\mathbf{r}\left(0\right)+\mathbf{v}t'$.

The retarded time $t'=t-(R'/c)\approx t-(|R-\hat{s}\cdot\mathbf{r}|/c)$ for $R'\approx R$ and $\hat{s}$ is constant in time.

Substituting the retarded time into the unperturbed orbit gives,

$$t'=\frac{(t-R/c+\hat{s}\cdot\mathbf{r}\left(0\right)/c)}{(1-\hat{s}\cdot\beta)} \quad , \tag{2.97}$$

which then gives,

$$\mathbf{k}_i\cdot\mathbf{r}\left(t'\right)-\omega_i t'=k_i\frac{\left(1-\hat{i}\cdot\beta\right)}{(1-\hat{s}\cdot\beta)}R-\omega_i\frac{\left(1-\hat{i}\cdot\beta\right)}{(1-\hat{s}\cdot\beta)}t-k_i\frac{\left(1-\hat{i}\cdot\beta\right)}{(1-\hat{s}\cdot\beta)}\hat{s}\cdot r_0+\mathbf{k}_i\cdot\mathbf{r}\left(0\right) \quad , \tag{2.98}$$

where $\hat{i}$ and $\hat{s}$ are the incident and scattering unit vectors.

For a plane monochromatic wave, the incident electric field can be written as,

$$\mathbf{E}_i\left(\mathbf{r},t'\right)=\mathbf{E}_{i0}\cos\left(\mathbf{k}_i\cdot\mathbf{r}-\omega_i t'\right) \quad , \tag{2.99}$$

and so the scattered electric field can be written as,

$$\mathbf{E_s}\left(\mathbf{R},t\right)=\left(\frac{q^2}{c^2m_eR}\right)\left[\hat{s}\times\left(\hat{s}\times\mathbf{E}_{i0}\right)\right]\cos\left[k_sR-\omega_st-\left(\mathbf{k}_s-\mathbf{k}_i\right)\cdot\mathbf{r}\left(0\right)\right] \quad , \quad (2.100)$$

and so the charge, q, radiates the Doppler shifted electromagnetic wave whose frequency and wave vector are,

$$\omega_s=\omega_i\frac{\left(1-\hat{i}\cdot\beta\right)}{\left(1-\hat{s}\cdot\beta\right)} \quad , \quad (2.101)$$

and

$$\mathbf{k}_s=\omega_s\hat{s} \quad . \quad (2.102)$$

It is convenient to work with a shift in frequency, $\omega=\omega_s-\omega_i=\left(\mathbf{k_s}-\mathbf{k_i}\right)\cdot\mathbf{v}=\mathbf{k}\cdot\mathbf{v}$, and wave vector $\mathbf{k}=\mathbf{k_s}-\mathbf{k_i}$.

For an electron, the time averaged scattered power in the solid angle $d\Omega$ is,

$$\left\langle P_s\left(\mathbf{R}\right)\right\rangle d\Omega=\left(\frac{cE_{i0}^2r_0^2d\Omega}{8\pi}\right)\left[\hat{s}\times\left(\hat{s}\times\hat{E}_{i0}\right)\right]^2 \quad , \quad (2.103)$$

where the angled brackets represent a time average and $r_0=e^2/m_ec^2=2.8179\times10^{-13}$ cm is the classical electron radius.

Experimentally, the fluctuating density is measured. The spectrum is normally written in terms of the spectral density function, defined as,

$$S\left(\mathbf{k},\omega\right)\equiv\lim_{V\to\infty,T\to\infty}=\frac{1}{VT}\left\langle\frac{n_e\left(\mathbf{k},\omega\right),n_e^*\left(\mathbf{k},\omega\right)}{n_{e0}}\right\rangle \quad , \quad (2.104)$$

where n_{e0} is the mean electron density and $N=n_{e0}V$ is the number of electrons within the scattering volume, V.

It can be shown that the scattered power [72], in the frequency range $\omega_s\rightarrow$

$\omega_s + d\omega_s$ and in the solid angle $d\Omega$ centred on $\mathbf{R}$ is,

$$P_s\left(\mathbf{R},\omega_s\right)d\Omega d\omega_s = P_i r_0^2 L d\Omega \frac{d\omega_s}{2\pi}\left(1+\frac{2\omega}{\omega_i}\right)\left[\hat{s}\times\left(\hat{s}\times\hat{E_{i0}}\right)\right]^2 n_e S\left(\mathbf{k},\omega\right) \quad , \quad (2.105)$$

where L is the length of the scattering volume. The term $(1 + 2\omega/\omega_i)$ is a result of two effects. The first is the relativistic headlight effect where light is preferentially directed in the emitter's propagation. The second effect is a result of the electron motion in the direction of the incident light vector interacting with the magnetic field of the probing beam. When the electron is moving towards the detector, the increased force enhances the velocity and as a result the scattered power.

Neglecting collisions, the spectral density function can be written as,

$$S\left(\mathbf{k},\omega\right) = \frac{2\pi}{k}\left|1-\frac{\chi_e}{\epsilon}\right|^2 f_{e0}\left(\frac{\omega}{k}\right) + \frac{2\pi Z}{k}\left|\frac{\chi_e}{\epsilon}\right|^2 f_{i0}\left(\frac{\omega}{k}\right) \quad , \quad (2.106)$$

where ϵ is the dielectric response of the plasma, χ_e and χ_i are the electron and ion susceptibilities and f_{e0} and f_{i0} are the electron and ion distribution functions.

For a stable plasma, Landau damping and collisions keep the resonant wave amplitude at a low level. The precise level of this damping depends critically on the form of the distribution function.

The electron and ion susceptibilities can be defined as,

$$\chi_e\left(\mathbf{k},\omega\right) = \int_{-\infty}^{+\infty} d\mathbf{v}\frac{4\pi e^2 n_{e0}}{m_e k^2}\frac{\mathbf{k}\cdot\partial f_{e0}/\partial\mathbf{v}}{\omega-\mathbf{k}\cdot\mathbf{v}-i\gamma} \quad , \quad (2.107)$$

and

$$\chi_i\left(\mathbf{k},\omega\right) = \int_{-\infty}^{+\infty} d\mathbf{v}\frac{4\pi Z^2 e^2 n_{i0}}{m_i k^2}\frac{\mathbf{k}\cdot\partial f_{i0}/\partial\mathbf{v}}{\omega-\mathbf{k}\cdot\mathbf{v}-i\gamma} \quad , \quad (2.108)$$

and the dielectric function is then defined as $\epsilon\left(\mathbf{k},\omega\right) = 1 + \chi_e\left(\mathbf{k},\omega\right) + \chi_i\left(\mathbf{k},\omega\right)$.

In thermodynamic equilibrium, the one-dimensional velocity distributions are Maxwellian and are given by,

$$f_{e0} = \sqrt{\frac{1}{\pi a^2}} \exp\left(-\frac{v^2}{a^2}\right) \quad , \tag{2.109}$$

and

$$f_{i0} = \sqrt{\frac{1}{\pi b^2}} \exp\left(-\frac{v^2}{b^2}\right) \quad , \tag{2.110}$$

where the mean thermal speeds are $a = \sqrt{2k_B T_e/m_e}$ and $b = \sqrt{2k_B T_i/m_i}$. The scattering cross section can then be written as,

$$S\left(\mathbf{k},\omega\right) = \frac{2\sqrt{\pi}}{ka} \left\{ \frac{A_e}{|\epsilon|^2} + \frac{A_i}{|\epsilon|^2} \right\} \quad , \tag{2.111}$$

where,

$$A_e = \exp\left(-x_e^2\right) \left[\left(1 + \alpha^2 \frac{ZT_e}{T_i} \mathrm{Rw}\left(x_i\right)\right)^2 + \left(\alpha^2 \frac{ZT_e}{T_i} \mathrm{Iw}\left(x_i\right)\right)^2 \right] \quad , \tag{2.112}$$

and

$$A_i = Z\sqrt{\left(\frac{m_i T_e}{m_e T_i}\right)} \exp\left(-x_e^2\right) \left[\left(\alpha^2 \mathrm{Rw}\left(x_e\right)\right)^2 + \left(\alpha^2 \mathrm{Iw}\left(x_e\right)\right)^2 \right] \quad , \tag{2.113}$$

and

$$|\epsilon|^2 = \left[1 + \alpha^2 \left(\mathrm{Rw}\left(x_e\right) + \frac{ZT_e}{T_i} \mathrm{Rw}\left(x_i\right)\right)\right]^2 + \left[\alpha^2 \mathrm{Iw}\left(x_e\right) + \alpha^2 \frac{ZT_e}{T_i} Iw\left(x_i\right)\right]^2 \quad , \tag{2.114}$$

where $x_e = \omega/ka$, $x_i = \omega/kb$ and $\alpha = 1/k\lambda_{De}$. The electron and ion susceptibili-

ties can then be written as,

$$\chi_e(\mathbf{k},\omega) = \alpha^2 \left[\mathrm{Rw}(x_e) + i\mathrm{Iw}(x_e)\right] \quad , \tag{2.115}$$

and

$$\chi_i(\mathbf{k},\omega) = \alpha^2 = \frac{ZT_e}{T_i}\left[\mathrm{Rw}(x_i) + i\mathrm{Iw}(x_i)\right] \quad , \tag{2.116}$$

where,

$$\mathrm{Rw}(x) = 1 - 2x\exp\left(x^2\right)\int_0^\infty \exp\left(p^2\right)dp \quad , \tag{2.117}$$

and

$$\mathrm{Iw}(x) = \sqrt{\pi}x\exp\left(-x^2\right) \quad . \tag{2.118}$$

Electron plasma resonance

There is a resonance in the high frequency part of the spectrum at $\omega \sim \omega_{pe}$. The ions cannot respond to such frequencies and so the ion component can be neglected. For collective scattering (where the laser wavelength $\lambda > \lambda_{De}$ and so the scattering is from thermal fluctuations rather than from free electrons), the electron Debye shielding contributes most to the spectrum. Each shield is from both the repulsion of the electrons and the attraction of the ions, however, the majority of electrons are moving so fast that the ions cannot respond to their motion and the shielding is primarily achieved by the repulsion of other electrons.

To find the resonance, the real part of ϵ is taken to be zero. The resonance occurs approximately when $\epsilon_R = 1 + \alpha^2 \mathrm{Rw}(\omega/kv_{th,e})$ and so there are two roots. However, at the lower frequency root, the Landau damping term is large and the resonance is strongly damped. The high frequency root can then be denoted by $x_{e0} = \omega_0/kv_{th,e} \gg$

1. The phase velocity is much greater than the electron mean thermal speed and so the waves propagate in the tail of the electron velocity distribution. If the effect of damping is neglected then,

$$\frac{1}{\alpha^2} = -Rw\left(x_{e0}^2\right) \approx \frac{1}{2x_{e0}^2} + \frac{3}{4x_{e0}^4} \quad . \tag{2.119}$$

This can be rearranged to give,

$$\omega_{epw}^2 \approx \omega_{pe}^2 + \frac{3k_B T_e}{m_e} k^2 \quad , \tag{2.120}$$

which is the Bohm-gross relation for longitudinal electron plasma waves.

Ion acoustic resonance

In the low frequency part of the spectrum, a resonance can occur at the ion acoustic frequency. In the low frequency part of the spectrum, there are contributions from both the ions and electrons. The resonances are then found by setting the full permittivity to zero,

$$\epsilon_R = 1 + \alpha^2 + \alpha^2 \left[\frac{ZT_e}{T_i} Rw\left(\frac{\omega}{k v_{th,i}}\right)\right] = 0 \quad , \tag{2.121}$$

and so,

$$\omega_{iaw} \approx \omega_{ac} = \pm k \left(\frac{\alpha^2 Z k_B T_e}{\left(1+\alpha^2\right) m_i} + \frac{3k_B T_i}{m_i}\right)^{1/2} \quad . \tag{2.122}$$

Relative drift of electrons and ions

Resonant oscillations in a plasma are limited by electron and ion Landau damping. The level of damping is proportional to the gradient of the velocity distribution functions, taken at the phase velocity of the waves. The resonances are strongly affected by a resonant drift of the ions and electrons because this shifts the phase

velocity of the waves to a different part of the distribution function.

The effect of small electron drift velocities relative to the ions can be studied by shifting the electron velocity distribution function relative to the ion frame of reference. In this case the Maxwellian distribution functions become,

$$f_{e0}\left(v\right) = \frac{e^{-\left(v-v_d\right)^2/v_{th,e}^2}}{\left(\pi v_{th,e}^2\right)^{3/2}} \quad , \tag{2.123}$$

and,

$$f_{i0}\left(v\right) = \frac{e^{-\left(v/v_{th,i}\right)^2}}{\left(\pi v_{th,i}^2\right)^{3/2}} \quad . \tag{2.124}$$

The resonances then appear at,

$$\epsilon_R = 1 + \alpha^2 \left[\mathrm{Rw}\left(x_e - x_d\right) + \frac{ZT_e}{T_i}\mathrm{Rw}\left(x_i\right)\right] = 0 \quad , \tag{2.125}$$

where $x_d = v_d/v_{th,e}\cos\chi$ and χ is the angle between $\mathbf{v}$ and the drift velocity $\mathbf{v_d}$.

When there is no drift, the resonant fluctuations at the ion-acoustic frequency are symmetric in amplitude, indicating that the Landau damping at both the positive and negative roots are equal. Adding a drift reduces the damping on the positive root and increases the damping on the negative root by moving the resonant waves onto a shallower or steeper part of the distribution functions. For a normalized drift, $x_d = 1$, the electron and ion Landau damping on the positive root are nearly equal and the electron Landau damping on the negative root has been significantly increased. For drift velocities larger than the ion-acoustic speed, the electron damping on the positive root goes to zero and if the growth of the electron wave is larger than the residual ion damping, the system will become unstable.

In summary, Thomson scattering is an extremely versatile diagnostic which can be used to obtain information on several different plasma quantities.

2.7.5 Other Plasma Diagnostics

There are numerous additional plasma diagnostics. For instance, proton radiography whereby mono-energetic protons are passed through a plasma and so are influenced by the magnetic fields present in the plasma. The proton radiograph can be used to reconstruct the magnetic field within the plasma [74].

Streaked optical pyrometry (SOP) measures the self emission from the plasma along one axis and then streaks the emission in time. This variation of self emission with time and space then allows the velocity of the plasma flow can be found.

2.8 Simulations

Simulations are important for describing aspects of the plasma that are difficult to diagnose experimentally due to the complexity and non-linearity of high-energy density plasmas. Different simulations are important for different aspects of the plasma. Radiation hydrodynamic simulations, such as FLASH [75, 76, 77], cover time and length scales over several orders of magnitudes by treating the plasma as a fluid. This makes hydrodynamic simulations extremely useful for designing and interpreting experiments. Kinetic effects cannot be included within hydrodynamic codes as this then makes the simulations too computationally intensive. Instead, if kinetic effects are required, particle-in-cell (PIC) codes are useful.

PIC codes, such as OSIRIS [78], use the Vlasov equation and so can be used to investigate kinetic instabilities within the plasma. Consequently, PIC codes tend to be computationally expensive and so are generally limited to short time scales and small length scales. Its therefore often impossible to fully replicate a laser-plasma experiment with a PIC simulation, but the combination of a hydrodynamic code and a PIC simulation can more fully replicate an experiment.

Optical and X-ray spectra can be predicted using a collisional radiative code such

as PrismSPECT [79]. These codes use atomic models to predict the resultant spectra, given input plasma conditions. An assumption must be made of what kind of plasma model to use, such as thermodynamic equilibrium, coronal model or a collisional-radiative model. Additional populations, such as a hot electron distribution, can be added to the plasma and so the code can predict the effect of this population on the spectra.

2.9 Summary

In this chapter the basic theory required for the remaining chapters is described. Basic plasma physics such as Debye length and Coulomb collisions are presented. Single particle motion, fluid theory and MHD are used to describe the motion of the plasma. Types of waves within a plasma that are most pertinent to the remaining chapters such as lower hybrid waves and Faraday rotation are derived. The basics of shock theory is described. Two different astrophysical problems are presented which will be elaborated upon in future chapters with relevant laboratory experiments. The interaction of a high power laser with a target and the associated plasma diagnostics are described. Finally, a brief description of the plasma simulations used in future chapters is presented.

Chapter 3

Electron Acceleration in a Magnetized Plasma

In this chapter a recent laser experiment, led by the author at the LULI laser facility, will be discussed. The relevant astrophysical motivation and theory is introduced. The experimental setup, diagnostics and results of the experiment are then described. Results from radiation hydrodynamic, particle-in-cell and PrismSPECT simulations are used to aid understanding of experimental results. Finally the experimental results are compared with a specific astrophysical case.

3.1 Astrophysical Motivation

The LULI experiment is the result of a campaign investigating particle acceleration as an effort to further understand the mechanisms behind the high energy particles observed astrophysically. Astrophysical shocks are revealed by the non-thermal emission of energetic electrons accelerated in-situ [47, 80, 81]. Strong shocks are expected to accelerate particles to very high energies [13, 37, 41], however, they require a source of particles with velocities fast enough to permit multiple shock crossings. Whilst the resulting diffusive shock acceleration process can account for observations,

the kinetic physics regulating the continuous injection of non-thermal particles is not well understood. Indeed, this injection problem is particularly acute for electrons, which rely on high frequency plasma fluctuations to raise them above the thermal pool [82, 53].

One mechanism for overcoming this injection problem is through lower-hybrid turbulence. Here, through a wave-particle interaction, energy can be passed from slow ions traveling perpendicularly to a magnetic field, to fast electrons traveling parallel to the magnetic field. This phenomenon has been postulated as an explanation for the X-ray production seen at the interaction between the Solar-wind and a comet [25]. The LULI experiment investigated the mechanism of lower-hybrid turbulence as a possible way of overcoming the injection problem and generating a suprathermal electron popoulation.

3.1.1 Lower-Hybrid Waves and Electron Acceleration

Lower-hybrid waves occur in a variety of laboratory and space environments and have been suggested to be an important electron-heating or energization mechanism in different magnetized plasma environments [83, 84, 85, 86].

Lower-hybrid waves are electrostatic ion waves that propagate quasi-perpendicularly to an external magnetic field. Lower-hybrid waves have a frequency between the ion and electron cyclotron frequency and can be generated through a plasma instability, namely the modified two-stream instability (MTSI) [87]. The MTSI is similar to the two-stream instability in the sense that it is formed through counter-streaming flows, however unlike the classic two-stream instability, the MTSI requires an external magnetic field oriented quasi-perpendicularly to a counter-streaming ion flow [41].

This instability excites lower-hybrid waves which have the following dispersion

relation [34]:

$$\omega^2 = \omega_{LH}^2 \left(1 + \frac{\omega_{pe}^2}{k_\perp^2 c^2}\right)^{-1} \left(1 + x^2\right), \tag{3.1}$$

where ω_{LH} is the lower-hybrid frequency,

$$\omega_{LH} = \sqrt{\frac{\omega_{ci}\omega_{ce}}{1 + \left(\frac{\omega_{ce}}{\omega_{pe}}\right)^2}}, \tag{3.2}$$

and x is defined by

$$x^2 = \frac{m_i}{m_e}\frac{k_\parallel^2}{k_\perp^2}\left(1 + \frac{\omega_{pe}^2}{k_\perp^2 c^2}\right)^{-1}, \tag{3.3}$$

and ω_{pe} is the electron plasma frequency, $k_\parallel$ and $k_\perp$ are the components of the wave vector $\mathbf{k}$ parallel and perpendicular to the magnetic field, ω_{ce} and ω_{ci} are the electron and ion cyclotron frequencies and m_i and m_e are the ion and electron masses.

These lower-hybrid waves can accelerate electrons through Cerenkov resonance. Since the lower-hybrid waves travel mostly perpendicularly to the magnetic field, this wave-vector component is much larger than that of the wave-vector parallel to the magnetic field. As a consequence, the lower-hybrid waves have a high phase velocity along the field lines that resonate with fast moving electrons as well as a low phase velocity across the field lines that resonate with the slow moving ions. Consequently energy can be transferred via the lower-hybrid waves from the ions traveling perpendicularly to the magnetic field to electrons traveling parallel to the field. In this manner, counter-streaming ions in an external magnetic field can accelerate electrons to large energies and so produce high energy X-rays.

This convenient property of lower-hybrid waves as an efficient channel for the acceleration of electrons above the thermal background, is well known in the magnetically confined fusion community [88] where it has been exploited with considerable

efficacy in past experiments [89, 90]. Although a different mechanism is favoured in toroidal configurations, for highly oblique shock such as might be created in the Solar wind [25, 91], supernova explosions [84] or during the formation of galaxy clusters [92], it is thought that the MTSI driven by reflected ions from the shock front, excites broad-band lower-hybrid modes.

The counter streaming ions that form the MTSI can then excite lower hybrid waves. The relative motion of the counter steaming ions provides the free energy that generates this instability. The energy from these counter streaming ions is then absorbed by the lower hybrid waves. Electrons traveling along the magnetic field lines can then absorb the wave energy, provided by the ions, and so are accelerated along the field lines. This acceleration is possible since these lower hybrid waves travel quasi-perpendicularly to the magnetic field and so have highly anisotropic phase velocities. The phase velocity of these waves is low in the direction across the field lines, allowing the waves to be in resonance with the ion beams, whilst the phase velocity can be very large in the direction along the field lines. The waves excited by the ion beams can then easily reach a Cerenkov resonance with the motion of the electrons along the magnetic field lines, accelerating these electrons to very high velocities [93]. In this manner, energy can be transferred from the counter streaming ions to the electrons.

3.1.2 Comet and Solar-wind interaction

Turning to astrophysical environments, in the passing of a comet through the Solar-wind, as described in Ref. [25], lower-hybrid waves have been invoked to explain cometary X-ray emission. In this scenario, which is equivalent to what is described in the experiment, the interaction of the incoming Solar-wind ions with the ions reflected by the cometary bow shock excites waves within the LH frequency range. Here, the photo-ionized cometary ions are accelerated by the $\mathbf{v} \times \mathbf{B}$ electric field,

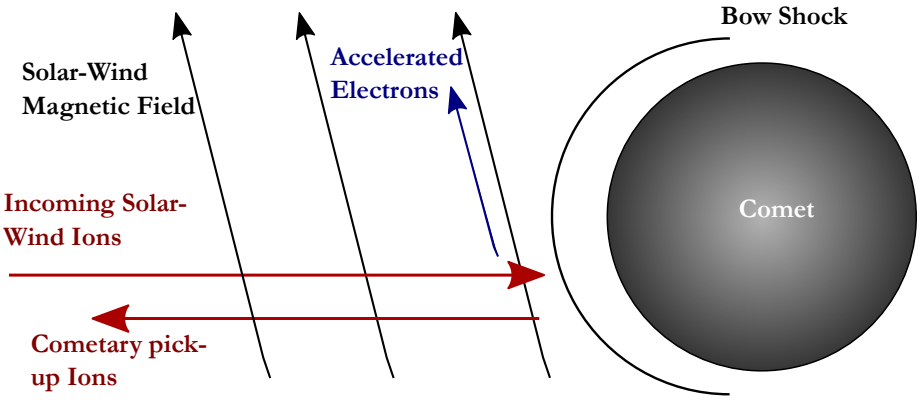

Figure 3.1: Interaction of a comet with the Solar-wind: The relative motion between the incoming solar-wind ions and cometary pick-up ions, across the solar-wind's magnetic field, result in the formation of the modified two-stream instability (MTSI) which, in turn, can excite waves within the lower-hybrid frequency range. The lower-hybrid waves can transfer energy from the counter-streaming ions traveling perpendicular to the magnetic field into accelerating electrons parallel to the magnetic field and so produce a suprathermal electron population capable of producing the observed X-ray spectra.

where **B** is the magnetic field of the Solar wind and **v** is the relative velocity of cometary ions and Solar wind, these so called pick up cometary ions form a beam in the Solar wind. Electrons are heated by LH waves, producing a suprathermal electron population. This hot electron population is estimated to have an average energy $\sim$ 100 eV and maximum energy $\sim$5 keV. These suprathermal electrons are then capable of generating bremsstrahlung and K-shell radiation from excited ions, mostly C, N and O [94].

An alternative explanation of the observed X-ray emission is offered by considering charge exchange processes [95]. In this scenario, the heavier ions in the Solar wind exchange charges with the neutral gases in the comet [96], resulting in stronger line emission. This is also supported by laboratory experiments using a beam ion trap [96].

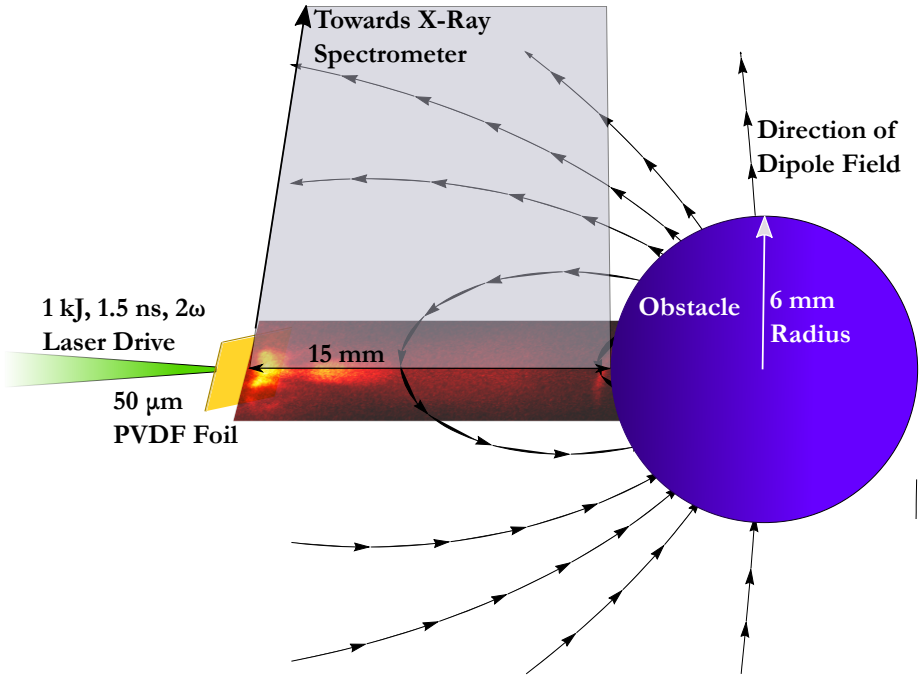

Figure 3.2: Schematic of Experimental Setup: 1 kJ, 1.5 ns laser drive at 527 nm with a spot size of 200 μm diameter is impacted onto a 50 μm PVDF ($C_2H_2F_2$) foil target producing an expanding plasma jet from the back surface as shown in the overlaid image of the 550-800 nm optical emission of the plasma. A 12 mm diameter spherical obstacle is placed 15 mm from the target foil. The obstacle is either a dipole magnetized Neodymium sphere with $\approx$ 7 kG surface field or a non-magnetized soda glass sphere of the same diameter. Optical diagnostics (interferometry and SOP) have $\approx$ 25 mm field of view, 250 ps gate time and look perpendicularly to the laser axis, similarly to the view above. An X-ray spectrometer spatially resolves along the laser axis with an RbAP crystal and spectrally resolves within the region of 630-770 eV.

3.2 Experimental Setup

While electron acceleration by lower-hybrid waves in the Solar system has been inferred from satellite measurements [97, 25], laboratory experiments provide reproducible and controllable conditions that can be used not only as a means of supporting space observations, but also for validating multi-scale transport predictions from simulation codes [98]. This experiment, where a laser-produced plasma flow impacts on a magnetized sphere (see Figure 3.2), mimics, for example, the interaction of the Solar-wind plasma with a comet [25], an environment where excess X-ray generation by accelerated electrons has been observed. The scaling between the experiment

and the comet interaction with the Solar wind is determined by a set of parameters shown in Table 3.1. While both lower-hybrid turbulence and charge exchange processes [96] are possible explanations, the experimental results are compatible only with the former.

The experiment was conducted at the LULI laser facility at École Polytechnique (France). Various diagnostics were implemented to probe the plasma before and after the interaction with the sphere (see Figure 3.4 for details).

The LULI laser facility delivers a 1 kJ, 1.5 ns laser drive (comprised of two 500 J laser beams) at 527 nm with a spot size of 200 μm diameter. The laser-drive was focussed onto a 50 μm PVDF ($C_2H_2F_2$) foil target producing an expanding plasma jet from the back surface. A 12 mm diameter spherical obstacle is placed 15 mm from the target foil. The obstacle is either a dipole magnetized Neodymium sphere with $\approx$ 7 kG surface field or a non-magnetized soda glass sphere of the same diameter. Various optical and X-ray diagnostics were used to probe the plasma as shown in Figure 3.3.

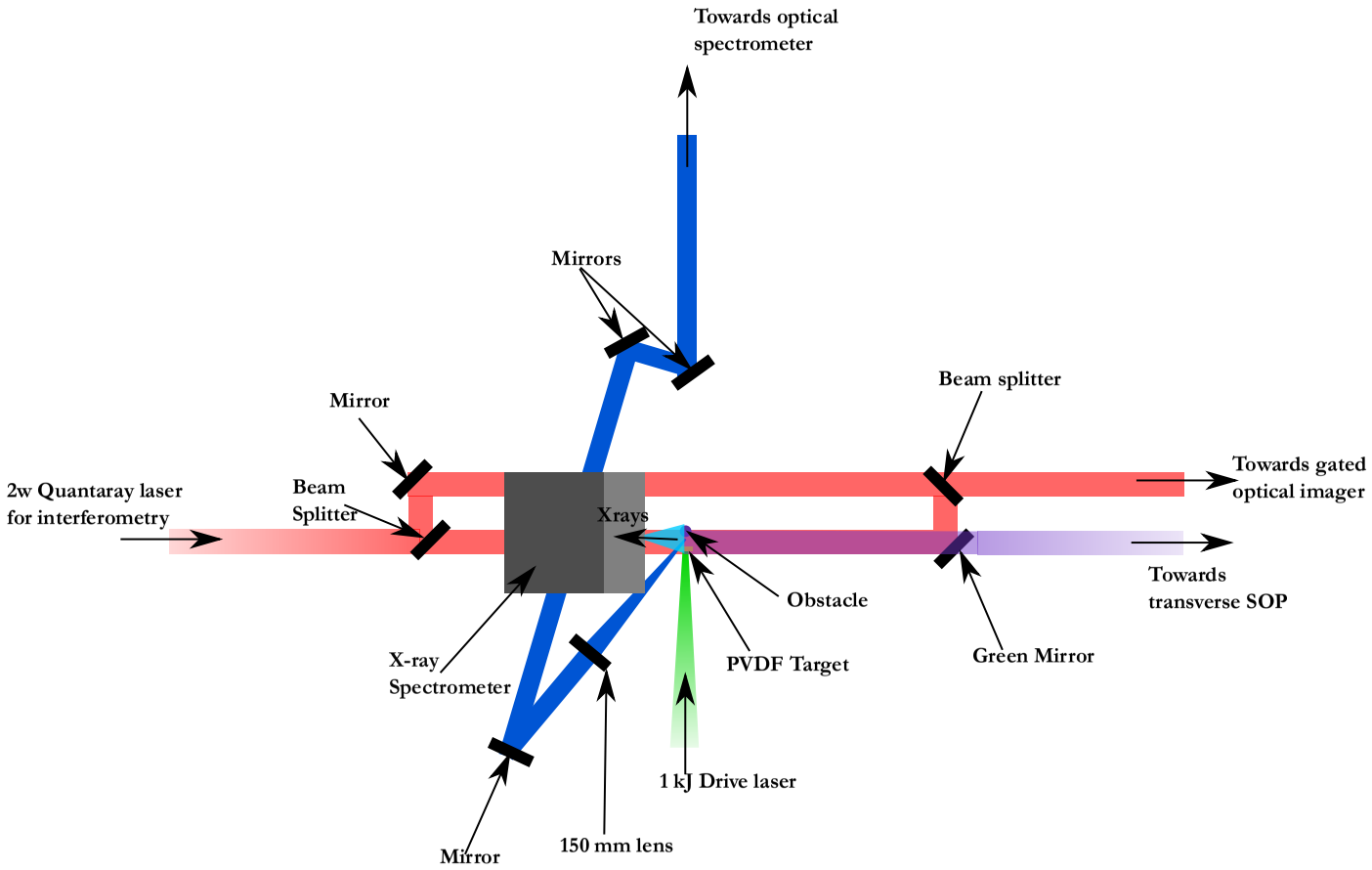

Figure 3.3: Plan view of Experimental Setup: The interaction of the expanding plasma jet with the obstacle is diagnosed by a variety of diagnostics. A transverse Michelson interferometer has an ≈ 25 mm field of view of the target-obstacle. Streaked optical pyrometry streaks the optical emission of the plasma along the laser axis in time, within a 550-800 nm bandwidth. Optical spectroscopy collects light 12 mm from the target, along the laser axis and spectrally resolves this light using an optical spectrometer. Xrays emitted from the interaction of the plasma and obstacle are collected by an Xray spectrometer and are spatially resolved along the laser axis and spectrally resolved within the 630-770 eV region.

3.3 Optical Data

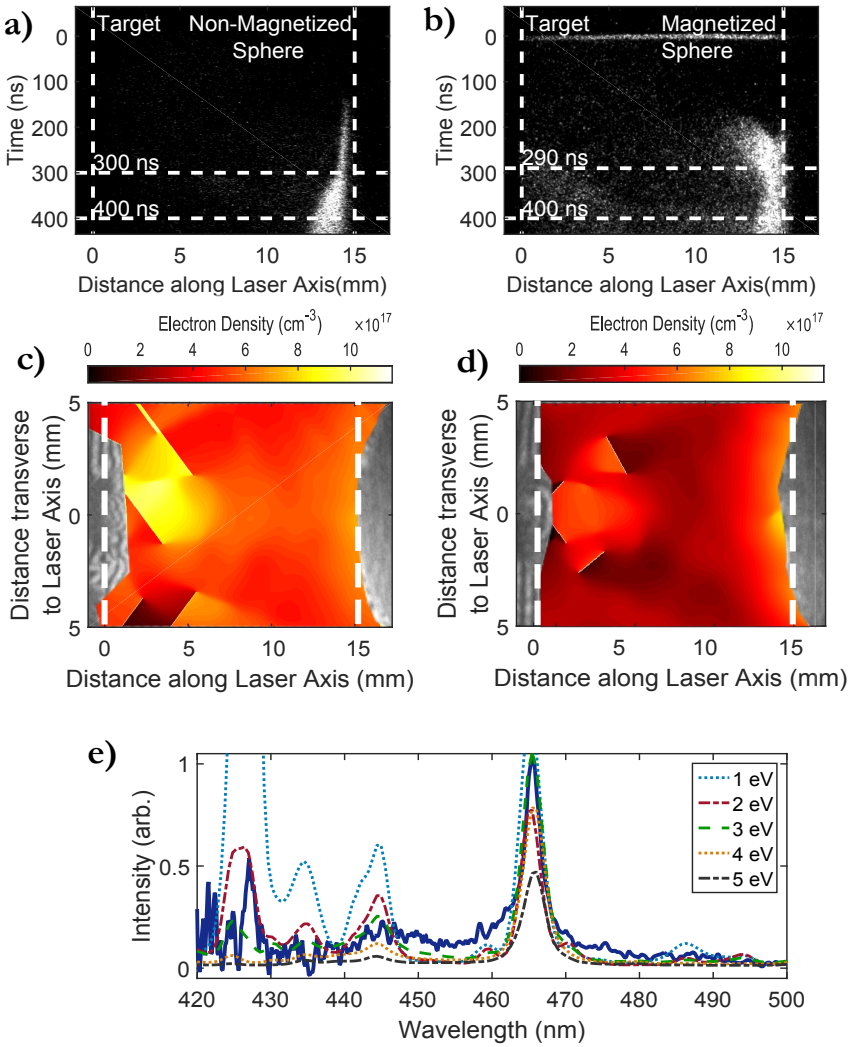

Figure 3.4: Optical Data: a) SOP data for a non-magnetized sphere. The plasma emission in the optical band 550-800 nm along the flow axis is streaked in time for 500 ns. Vertical dashed lines indicate the position of the target and sphere; horizontal lines indicate the time at which the interferometry data and FLASH simulation snapshot (see Figure 3.5) were taken. The plasma reaches the sphere by 200 ns indicating a flow velocity of 70 km/s. b) Same as a) but for a magnetized sphere. c) Transverse optical interferometry data taken at 300 ns for a non-magnetized sphere. The inferred electron density colour plot is overlaid. d) Same as c) but taken at 290 ns for a magnetized sphere. e) Optical emission spectra of the plasma (dark blue solid line) at 300 ns, 12 mm from the target along the flow axis for the non-magnetized sphere case. Different spectra predicted by the code PrismSPECT [99] (dashed lines) are overlaid and, when fitted by eye, give an electron temperature best fit of 3 eV.

3.3.1 Optical Diagnostics

Various diagnostics were implemented to probe the plasma before and after the interaction with the sphere (see Figure 3.4 for details).

Streaked optical pyrometry (SOP) was used to determine the velocity of the plasma outflow from the PVDF foil. The SOP diagnostic was setup such that plasma emission in the 550-800 nm optical band along the laser axis was streaked in time for 500 ns. The SOP data can be used to infer the velocity of the plasma flow from the foil. The emission from the laser-drive can be seen clearly at 0 ns in Figures 3.4a,b. At 210 ± 10 ns, there is strong plasma emission at the sphere, indicating that the plasma has traveled the 15 mm from the foil-target to the sphere, thus indicating a flow velocity of 70 ± 3 km/s. The SOP data shown in Figures 3.4a,b indicates the presence of transients between 200-300 ns. These transients are present in both the magnetized and non-magnetized cases and so are caused by the interaction of the plasma with the sphere, not by the magnetic field.

Transverse optical interferometry was used to determine the electron density. The Mach-Zender interferometry diagnostic was implemented using a 2ω Quantaray laser. The interferometry diagnostic had a $\approx$ 25 mm field-of-view, 250 ps gate time and looked perpendicularly to the laser axis (similarly to the view shown in Figure 3.2). A reference image with no plasma present was taken before each laser-shot. The difference between the pre-shot image and on-shot image can then be used to infer the electron density. The electron density colour maps were generated using the Interferometric Data Evaluation Algorithm (IDEA) software [100]. The electron density rises sharply close to the sphere in the magnetized case, but streams smoothly around the sphere in the non-magnetized case and so the electron density remains roughly constant. However, the shot-to-shot variations and noise in the interferometry data are 3-7 $\times 10^{17}$ cm^{-3}, and so taking a bulk electron density 5×10^{17} cm^{-3} in the upstream flow is appropriate.

The spectra from the optical emission of the plasma on the flow axis, 12 mm from the target foil can be used to determine the bulk electron temperature of the plasma. The optical spectroscopy diagnostic spectrally resolved the optical emission of the plasma on the laser axis, 12 mm from the target foil. The absolute spectral response of the diagnostic was made using a white light calibration, enabling the true spectrum to be recovered from the raw data. The optical spectrum was then fitted using the PrismSPECT software.

Combining the data from all optical diagnostics indicates that the interaction of the plasma with the obstacle is different for both cases (see e.g., [101, 102]). For the non-magnetized sphere, there is less pronounced plasma build up in front of the sphere.

In the non-magnetized case, the plasma begins to flow smoothly around the sphere [101]. Near the axis of the flow and close to the surface of the sphere a shock with $\sim$ 1 mm stand-off distance can be seen. In the magnetized case, the perpendicular field lines constrain the flow, making it more difficult for the plasma to fully flow around the sphere. Consequently, there is a larger pressure build up in front of the sphere, generating a shock at $\sim$ 2.5 mm stand-off position, larger than that of the non-magnetized case. Balancing the ram pressure of the plasma flow with that of the compressed magnetic field gives an estimation for the expected stand-off distance in the magnetized case of $\sim$ 1 mm, similar to the experimental value.

3.3.2 Hydrodynamics Simulations

To further understand the flow dynamics and its interaction with the sphere, 2-dimensional radiation-magnetohydrodynamics (MHD) simulations were performed using the FLASH code. The simulations agree qualitatively with experimental measurements, as shown in Figure 3.4, while providing additional estimates of bulk plasma properties.

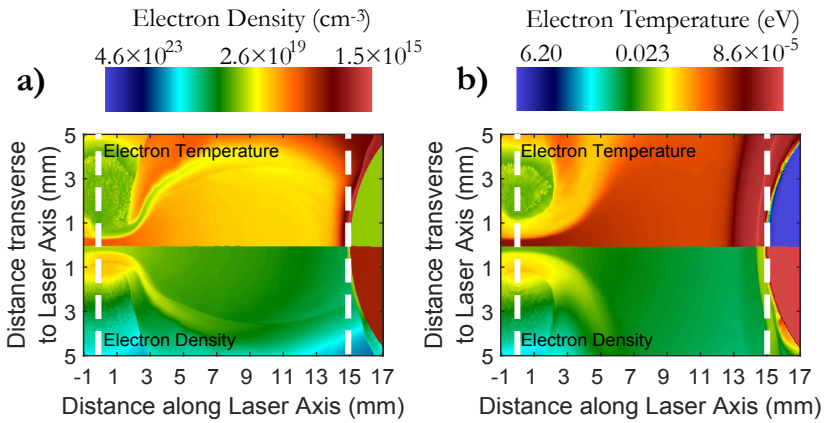

Figure 3.5: Radiative-magnetohydrodynamics Simulations a) Snapshot of a magnetohydrodynamic simulation with no external field after 400 ns, symmetric about the laser-axis. Pseudocolour plots of electron temperature (top) and electron density (bottom) are shown. b) Same as a) but with a constant 5 kG field perpendicular to the flow axis. Colourbars are the same for both a) and b).

2-dimensional, radiation-magnetohydrodynamic simulations were performed using the publicly available code FLASH. FLASH is a parallel, multi-physics, adaptive-mesh-refinement (AMR), finite-volume Eulerian code. The simulations performed here include many of the high-energy density capabilities of the code [75], such as three-temperature MHD solvers, non-ideal MHD effects such as magnetic resistivity, heat exchange between ions and electrons, implicit thermal conduction and radiation transport in the multi-group diffusion approximation, and laser energy deposition via inverse Bremsstrahlung.

The FLASH simulations [75] were set up to fully reproduce the laser-plasma interaction and the resulting flow expansion and collision with the obstacle. Simulations have been performed with and without a constant ambient field of 5 kG strength orientated perpendicularly to the laser axis, which emulates the dipole field of the experiment within the region adjacent to the sphere. Simulations were set up such that the computational domain (2 cm $\times$ 4 cm) was symmetric about the laser-axis and, utilizing FLASH AMR, spatial scales were resolved down to 8 μm. Spatial reconstruction was carried out using a 3rd-order piecewise parabolic method (PPM) [103] and a minmod limiter, while temporal integration was done with the

second-order unsplit USM algorithm [104]. The upwind fluxes were computed using the Harten-Lax-van Leer Contact (HLLC) [105] Riemann solver. The simulations were carried out using the SCARF-MagnaCarta cluster at the Rutherford Appleton Laboratory and the Asterix cluster of the Flash Center for Computational Science at the University of Chicago.

The simulation predictions closely resemble what was observed in the experiment. The plasma outflow from the foil target travels at 70 km/s, reaching the sphere at $\sim$ 200 ns, as seen in the experimental data. In both the field and non-field cases, a shock forms at the sphere surface. Similarly to the experiment, the non-field case results in a much thinner bow-like shock than the field case. As shown in Figure 3.5 the simulation predicts bulk electron densities $\sim 5 \times 10^{17}$ cm^{-3}, rising to over 10^{18} cm^{-3} at the shock front, in agreement with the laboratory data. Additionally, at the time and spatial position that the optical spectroscopy data was taken, FLASH predicts an electron temperature of 3 eV, matching the experiment. The quantitative agreement between simulation and experiment gives us confidence in the accuracy of the electron temperature predictions from the FLASH code. The electron temperature is $\sim$ 200 eV at the beginning of the laser drive, but then it adiabatically cools to a bulk electron temperature $\sim$ 3 eV for times $t > 50$ ns.

3.3.3 Implications for MTSI Production

To produce a MTSI experimentally, several conditions must be met. First, the electric field produced by the shock must be strong enough to reflect ions and so create a counter-streaming ion flow. Secondly, its imperative to check that the growth of the MTSI is not damped by collisions within the plasma. This means that the counter-streaming ions must be effectively collisionless with one another (although they can be thermally collisional).

Shock-Produced Electric Field

The magnetic field carried by the ablated plasma is weak, and from the measured plasma parameters (flow velocity, v, Alfven velocity, v_A, and sound speed c_s) we infer the shock formed to be highly super-critical with a fast magneto-sonic Mach number, $M_{MS} = v/\sqrt{v_A^2 + c_s^2}$, of 5.7 ± 0.2, necessitating a significant reflected ion component [106]. The electric field influencing the plasma near the shock can be estimated using the magnetic field and ion density calculated in FLASH.

For the shock to reflect incoming ions, the cross-shock electric potential must exceed the kinetic energy of the incoming ions. The electric field influencing the plasma near the sphere can be estimated using [107] $E_\parallel \sim \frac{1}{2\mu_0 n_i e}\frac{dB_\perp^2}{dx}$, where $E_\parallel$ is the electric field parallel to the flow axis, n_i is the ion density and $B_\perp$ is the magnetic field perpendicular to the flow axis and the derivative is taken along the flow axis direction. FLASH simulations predict an electric field of ~ 70 MeV/m at a distance of 0.5 mm from the sphere at 300 ns, increasing as the simulation progresses. Assuming a shock thickness on the order of the electron skin-depth $L \sim 10$ μm, the resulting cross-shock potential ≈ 700 eV is sufficient to reflect incoming Fluorine ions, with an expected kinetic energy of ~ 500 eV. These reflected ions produce the counter-streaming ion flow, which are necessary for generating lower-hybrid turbulence, an effect not captured in FLASH simulations.

Plasma Collisionality

Since the thermal background is relatively cold compared with the velocity of the reflected ions, the reflected ions will be dragged by the electrons in the thermal plasma and so the ion-electron collision mean-free-path (note not the thermal collision mean-free-path) is the most important quantity in determining whether or not the modified two-stream instability will be damped by collisions. Using PrismSPECT, a downstream plasma electron density of 10^{17} cm^{-3} and 3 eV electron temperature, the

ionisation of the Carbon, Hydrogen and Fluorine ions is 3, 1 and 2 respectively. The ion-electron collision distance for the electrons to slow down the beam of reflected ions can be calculated using standard expressions, see Table 2.1. Note that for this case, the thermal energy of the electrons is large compared to the reflected ion beam energy.

For the three different ions, this calculation gives a distance for the ions to be slowed down by electron collisions as 1, 1.5 and 5 mm for the Hydrogen, Carbon and Fluorine ions respectively. This means that for a 3 eV background plasma, the Hydrogen and Carbon reflected ions will be slowed down within $\sim$ 1 mm, whereas the Fluorine ions are effectively collisionless on the scales of interest for electron heating. Electron-electron collisions on the other-hand are the dominant mechanism for electron scattering. Although the electrons are only weakly magnetized, they can be accurately treated as an isotropic fluid, and as such, can be shown to satisfy the usual fluid limit of the lower-hybrid instability [87].

In the experiment, the counter-streaming Fluorine ions have a collisional mean-free-path of $\sim$ 5 mm, to be compared with their gyroradius $\sim$ 2 cm. Thus the Fluorine ions are not magnetised. However, since only electron heating by modes with wavelength $\ll$ 5 mm are considered, this does not affect the growth of the lower-hybrid instability [87].

3.4 X-ray Data

3.4.1 X-ray Diagnostic

The X-ray spectrometer consisted of a 25×50 mm^2 RbAP crystal, with 100 mm radius of curvature, operating at a Bragg angle of 43.5^o and is cylindrically bent along the long axis of the crystal. In this Von-Hamos geometry, the X-rays from the plasma are focused onto a 60×100 mm^2 image plate detector as shown in Figure 3.6.

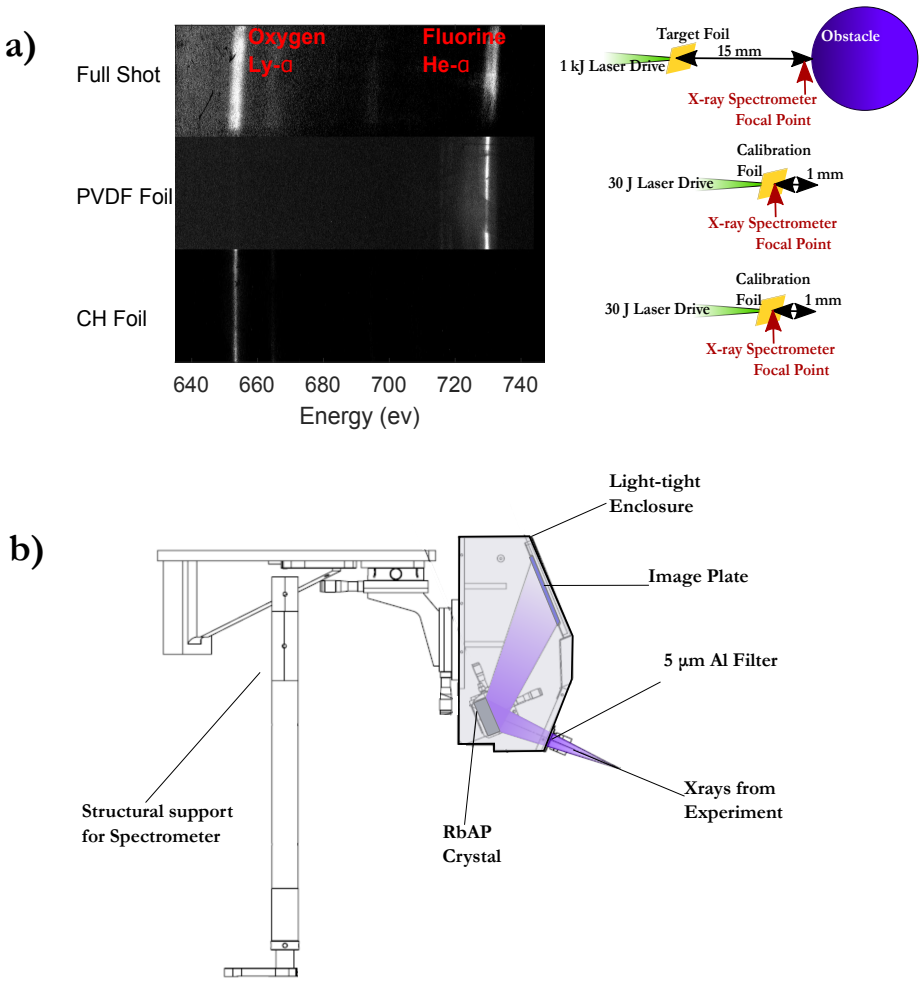

Figure 3.6: X-ray Spectrometer setup and Calibration: a) Schematic of crystal and image plate orientation in relation to the plasma. b) Spectra from PVDF and CH flag shots and a full shot. The flag shots can be used for calibrating the energy of the X-rays. c) Schematic of X-ray spectrometer, including how the crystal is housed.

This setup allows for both spectral resolution (620–770 eV full range) and spatial discrimination with 1:1 magnification [71]. By geometrical considerations [71], it is possible to show that a 1 mm source size is blurred on the image plane by 20 μm. Both the crystal and image plate were housed in a light-tight enclosure containing a small window through which the X-rays from the sample could reach the crystal (see Figure 3.6). The window was filtered with 5 μm of Aluminium.

The raw signal on the image plate was analysed in the following manner. First, the background noise across each data set was removed. The background signal

varies linearly along both the horizontal and vertical axes of the image plate. This background can be readily subtracted from the data signal. To calibrate the energy scale along the image plate, both PVDF and CH foils, placed at the focal position of the spectrometer, were used as shown in Figure 3.6. The PVDF foil produces a fluorine line at 731 eV (similarly to the main experiment). The CH foil (as expected) does not produce a line at 731 eV. Traces of Oxygen present in the vacuum chamber (rather than in the material content of the target) produce lines at 653 eV, 664 eV and 698 eV that can be seen on the image plate.

3.4.2 X-ray Data

The plasma emission in the soft X-ray range (630-770 eV) has been probed with an X-ray spectrometer that spatially resolved along the flow axis [71]. The integrated intensity of the observed Fluorine X-ray line can then be plotted as a function of position along the flow axis (see Figure 3.7). The background corrected data showed a clear line at 731 eV for all shots, the Fluorine He-α line. For every shot, the signal from the Fluorine He-α line at a given distance from the sphere has been frequency-integrated and averaged over a 0.3 mm interval. To collate the results, data from shots with the same type of sphere were averaged together. To aid comparison, different data sets are rescaled such that the peak of the spectrally resolved emission in the region close to the sphere (as shown in Figure 3.7) for the magnetized case is set to unity.

The standard deviation of the signal within the 0.3 mm spatial band determines the primary error for each data point as shown in Figure 3.7. Additionally, since the final data points are an average of several shots, the overall error is the sum in quadrature of the error for individual shots.

The excess in soft X-rays in the magnetized shots suggests that electrons of energies $\gg 3$ eV must be present. As lower-hybrid turbulence requires the reflected

ions to move perpendicularly to the field lines, the case when the sphere was rotated to have the field lines parallel to the flow has also been considered. In the latter configuration, there was no appreciable increase in X-ray intensity close to the sphere.

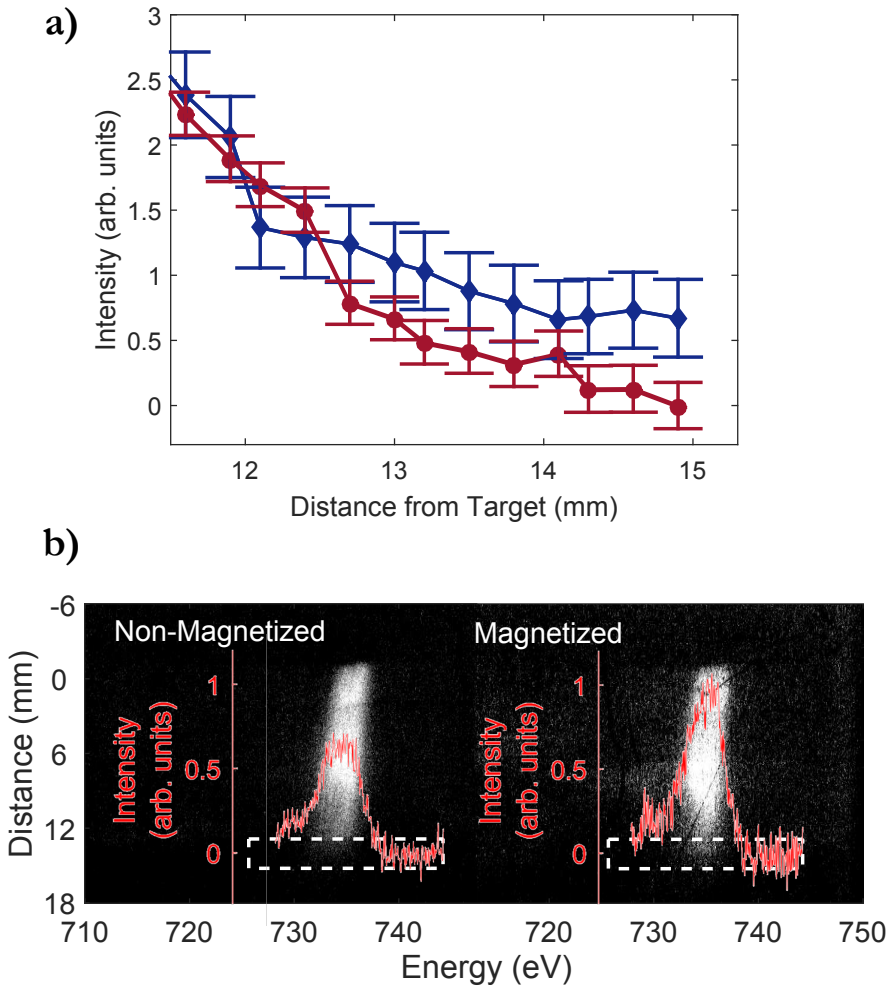

Figure 3.7: X-ray Data: a) Integrated X-ray intensity of the Fluorine He-α line as a function of position along the laser axis. Data for magnetized sphere shots (blue diamonds) has an increased intensity close to the sphere when compared with data for non-magnetized sphere shots (red circles). b) X-ray data, showing the Fluorine He-α line for both the non-magnetized (left) and magnetized (right) shots. For both cases, a white rectangle and an additional plot have been overlaid. The white rectangle indicates the region where the spatial lineouts were taken. The overlaid plots show the spectral structure within the white rectangle (i.e. close to the sphere). The intensity of the non-magnetized spectra is taken relative to the magnitude of the magnetized spectra.

3.5 Electron Energy Determination

3.5.1 Particle-in-Cell Simulations

To investigate further the lower-hybrid origin for the excess X-ray emission near the magnetized sphere and the possible presence of a suprathermal electron population, 2D particle-in-cell (PIC) simulations of the plasma flow collision with the dipolar magnetic object were performed (see Figure 3.8) using the massively parallel, fully relativistic code OSIRIS.

In these OSIRIS [78] PIC simulations, a hydrogen plasma is injected continuously from the left hand boundary with temperature $T_e = T_i \simeq 3$ eV and velocity v_0. Due to the high computational costs, OSIRIS simulations were performed with a flow velocity $\frac{v_0}{c} = 0.1$ and an electron-ion mass ratio of $\frac{m_i}{m_e} = 100$, where m_i is the average ion mass and m_e is the electron mass. The simulation results need to be scaled back to laboratory conditions. The simulation has an externally applied magnetic field $\mathbf{B} = \mathbf{B}_0 + \mathbf{B}_\mathrm{d}$, where $\mathbf{B}_\mathrm{d}$ is the sphere dipolar field (modeled in the simulation plane) and $\mathbf{B}_0$ is an upstream magnetic field with a magnitude chosen such that the ion Larmor radius is $\rho_i \simeq 8c/\omega_{pi}$ (where ω_{pi} is the ion plasma frequency), similarly to experimental conditions at the shock position. The simulation domain has dimensions $L_x \times L_y = 960 \times 1600 c/\omega_{pe}$ and the grid resolution is 10 cells per c/ω_{pe} in both directions, with 25 simulation particles per cell per species. Periodic boundary conditions are used in the y direction, and open boundary conditions are used for the right hand boundary. Figures 3.8 a) and b) show only a fraction of the simulation domain.

OSIRIS simulation results indicate, in agreement with previous FLASH simulations, that as the plasma impacts the sphere (of typical size larger than the ion Larmor radius), a bow shock develops [108]. The counter-propagating ion flow is unstable and excites plasma waves in the lower-hybrid range ahead of the shock

front (see Figure 3.8). These waves are then amplified and break, resulting in a turbulent, compressed plasma region. In fact the ratio between the parallel ($k_{\parallel}$) and perpendicular ($k_{\perp}$) wavenumber of these modes is consistent with the idealised dispersion relation for lower-hybrid waves of $\frac{k_{\parallel}}{k_{\perp}} \approx \sqrt{\frac{m_e}{m_i}}$ [25], as highlighted in Figure 3.8 (m_e and m_i are the electron and ion masses, respectively). OSIRIS simulations also show that when crossing the shock, the upstream plasma is significantly heated. The observed downstream wave spectrum is thus consistent with the hypothesis of a resonant interaction between electrons and ions being driven by lower-hybrid turbulence.

The plasma ions are reflected at the shock front and travel upstream to a distance of the order of the ion Larmor radius. The electron temperature was extracted from the OSIRIS simulations by mapping the electron distribution function in space and computing its second central moment. The downstream temperature was found to be 10–100 keV and is maximum at the bow shock flanks.

The convergence of OSIRIS simulations with scaled up/down plasma velocities/ion-electron mass ratios has been confirmed by comparing the results of previous simulations similar to the one presented here with plasma fluid velocities down to 0.02c and ion-electron mass ratios up to $m_i/m_e = 900$ (see [108]). These parameters, in particular the ion-electron mass ratio, control the separation between ion and electron temporal and spatial scales. Scaling them appropriately allows a significant reduction of the computational effort to perform the numerical experiments, yet it is still possible to gain important physical insight into the dynamics of these complex systems.

A more accurate description of the experiment could be obtained by using, for example, a multi-species plasma. In particular, the interaction between the different species with the field at different times is expected to lead to a transient. However, the transient always happens when the plasma cavity is formed and before the tur-

bulent region is excited (which happens on ∼1 ion gyroperiods, in the collisionless limit). Whether this transient time can be extended with the introduction of a multi species plasma is an interesting question, but one very difficult to answer with full PIC simulations. This would require separating clearly the time scales of the different ion species, which is computationally extremely demanding.

Despite the OSIRIS simulations being collisionless and the laboratory plasma being mildly thermally collisional, the OSIRIS results can still be applied to the laboratory plasma. The electron-electron collisions in the laboratory plasma preserve the electron isotropy and so the temperature anisotropy as seen in the OSIRIS simulations will be less pronounced in the laboratory plasma. The electron-electron collisions do not inhibit the development of the modified two-stream instability and so the average hot electron energy in the OSIRIS simulations (75 keV) can still be scaled to laboratory conditions to give a reasonable estimate of the average hot electron energy in the laboratory.

3.5.2 Electron Energy

The average energy of electrons accelerated by lower-hybrid waves can be estimated [25]. First the average energy gain of the electrons accelerated by lower-hybrid turbulence is estimated. Assuming that the energy is transferred from the ions to the electrons with an efficiency factor α, energy flow balance requires that

$$\alpha n_i m_i u^3 = n_e E_e \sqrt{\frac{E_e}{m_e}} \quad , \tag{3.4}$$

where n_i and n_e are the ion and electron densities of the resonant particles, u is the ion velocity, and E_e is the resonant electron energy. The resonant electron density can be obtained by balancing the growth rate of the ion instability against Landau

damping due to electrons moving parallel to the magnetic field, hence

$$n_e = E_e \frac{n_i}{m_i u^2}. \tag{3.5}$$

The average energy of electrons accelerated by lower-hybrid waves is then given by

$$E_e = \alpha^{2/5} \left(\frac{m_e}{m_i} \right)^{1/5} m_i u^2 \quad , \tag{3.6}$$

where α is an efficiency factor and u is the ion velocity. Using Equation 3.6, the PIC results can be scaled to the laboratory measurements. Since the PIC simulation predicts that lower-hybrid turbulence heats electrons to $E_e^{PIC} \sim 75$ keV, the expected heating for laboratory conditions is

$$\frac{E_e^{Lab}}{45 \text{ eV}} = \frac{E_e^{PIC}}{75 \text{ keV}} \left(\frac{m_e^{LAB}}{m_e^{PIC}} \right)^{1/5} \left(\frac{m_i^{Lab}}{m_i^{PIC}} \right)^{4/5} \left(\frac{u^{Lab}}{u^{PIC}} \right)^2 \quad , \tag{3.7}$$

where it is assumed that the efficiency factor is the same in both the laboratory and in PIC simulations (also note that the electron-ion mass ratio in the simulation is different from that in the experiment). Given that the predicted average electron heating in the laboratory is $\sim$ 45 eV, this electron energy can then be used in Equation 3.6 to determine an efficiency factor of $\alpha \sim 0.1$. The PIC simulation suggests that these accelerated electrons have a nearly Gaussian spectrum. The high energy tail of this distribution is then responsible for the observed X-ray excess.

The $\sim$ 45 eV electrons will be magnetised in the strong pre-shock fields. However, their gyro-radii are still not sufficient to permit collisionless transport across the shock [109].

3.5.3 PrismSPECT Simulations

The collisional-radiative code PrismSPECT was used to calculate the X-ray emission from the predicted hot electron population of lower-hybrid electrons. The PrismSPECT calculation uses a bulk plasma electron density of 5×10^{17} cm^{-3} and electron temperature of 3 eV, for a range of efficiency factors α from 0–0.5. For a given α, the energetic electron population had a Maxwellian distribution with average energy given by Equation 3.6 and density given by Equation 3.5.

When no hot electron population was present, no Fluorine X-rays were obtained. As the efficiency factor α increases, the X-ray intensity of the observed Fluorine line also increases (see Figure 3.9). The PrismSPECT results show that an average hot electron energy of 45 eV is sufficient to produce the X-rays observed within the laboratory.

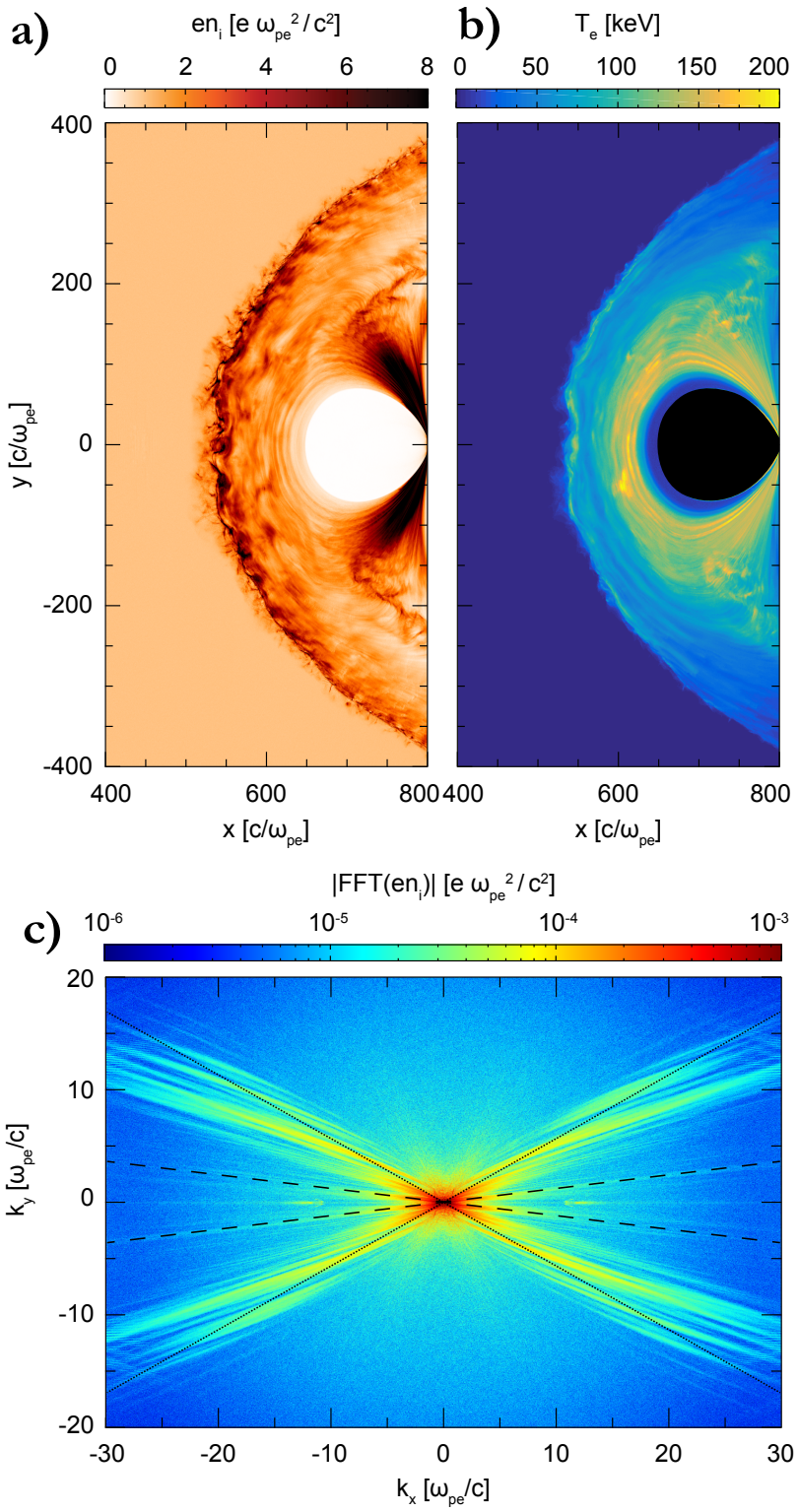

Figure 3.8: PIC Simulations: a) injected ion density, b) electron temperature and c) wave spectrum. The wave spectrum is calculated by performing a Fourier transform on the ion density to gain information on the parallel and perpendicular k-numbers. The black dashed lines indicate modes that have a ratio in k-number consistent with the lower-hybrid dispersion relation for ions reflected horizontally off of the shock. The black dotted lines indicate modes that have a ratio in k-number consistent with the lower-hybrid dispersion relation for ions reflected on the flanks of the bow shock. All figures are taken at the same time of 6 ion cyclotron periods. These PIC simulations were performed by F. Cruz.

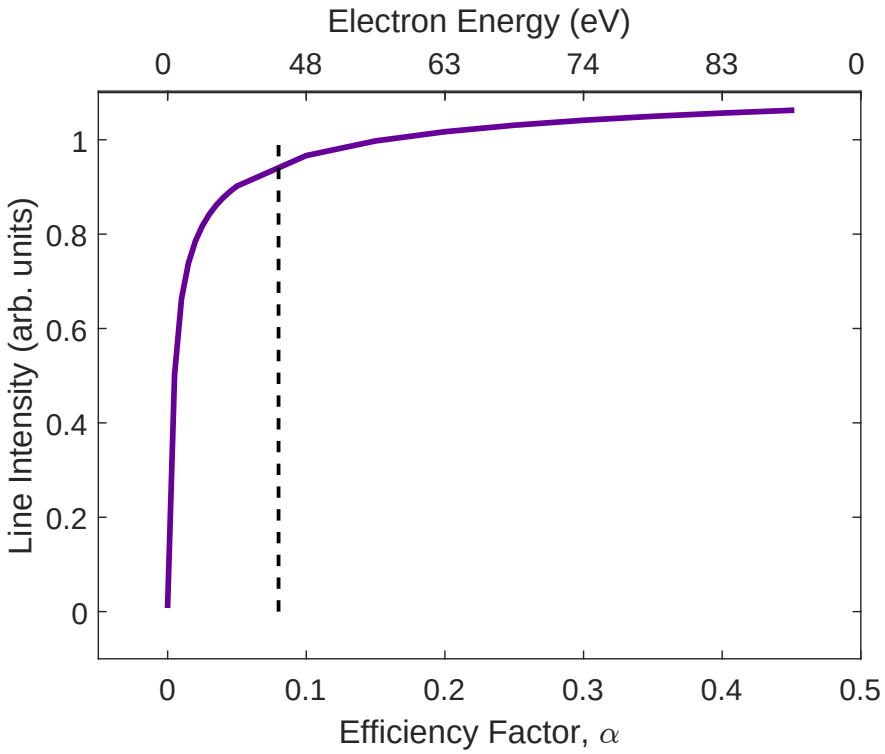

Figure 3.9: PrismSPECT: Results from PrismSPECT (purple line) indicate that as the hot electron population is increased in both fraction and average energy according to the efficiency factor α from Equation 3.6, the logged intensity of the Fluorine He-α line also increases (the average electron energy for a given value of α is shown in the top horizontal axis for reference). When no hot electron population is present, no Fluorine He-α line is generated. There is minimal contribution from bremsstrahlung. The average hot electron energy ($E_e \sim 45$ eV) and efficiency factor ($\alpha \sim 0.1$) for laboratory conditions is indicated with the black dashed line.

3.6 Comparison with Astrophysics

3.6.1 Comparing the Laboratory and Space

Table 3.1: Laboratory, Space and Simulation Parameters: Where m_p, m_e are the proton and electron mass, e is the electron charge, $\omega_{pe} = \sqrt{10^6 n_e e^2/m_e\epsilon_0}$ is the electron plasma frequency, $v_{te} = \sqrt{2eT/m_e}$ is the electron thermal velocity, $c_s = \sqrt{eZT/M + 3eT/M}$ is the sound speed, $V_A = B/\sqrt{\mu_0\left(Mn_i + m_e n_e\right)}$ is the Alfven velocity, $P_T = 10^6 n_e T e$ is the thermal pressure and $P_M = B^2/2\mu_0$ is the magnetic pressure. The length scale, L, is the minimum of the ion-beam mean free path, $V\tau_{ie}$ and the ion gyro-radius.

Quantity	Expression	Experiment	Comet-SW	PIC
Ion Mass, M	–	19 m_p	16 m_p	100 m_e
Ion Charge, Z	–	2	1	1
Electron Density, n_e (cm^{-3})	–	$5/3 \times 10^{17}$	10	5×10^{17}
Electron and Ion Temperature, T, (eV)	–	3	0.1	1
Flow Velocity, V, (m/s)	–	70×10^3	500×10^3	3×10^7
Magnetic Field, B, (T)	–	0.5	10^{-9}	320
Electron cyclotron frequency, ω_{ce}, (rad/s)	eB/m_e	8.8×10^{10}	1.8×10^3	5.7×10^{13}
Ion cyclotron frequency, ω_{ci}, (rad/s)	ZeB/M	5.0×10^6	0.060	5.7×10^{11}
Electron Larmor radius, $\mathrm{r_{ge}}$, (m)	$m_e v_{te}/\left(eB\right)$	1.2×10^{-5}	110	1.0×10^{-8}
Ion Larmor radius, $\mathrm{r_{gi}}$, (m)	$MV/\left(ZeB\right)$	0.014	8.4×10^6	5.3×10^{-5}
Sound Mach number	V/c_s	8.0	320	360
Alfven Mach Number	V/V_A	8.0	29	0.70
Plasma beta	P_T/P_M	0.80	4.0×10^{-3}	1.9×10^{-6}
Lower-hybrid frequency, ω_{LH}, (rad/s)	Equation 3.2	6.7×10^8	10	3.3×10^{12}
Average electron energy (eV)	Equation 3.6	30	100	5.0×10^4
$r_{ge}/\left(c/\omega_{pe}\right)$	–	0.90	0.063	0.0014
$r_{gi}/\left(c/\omega_{pi}\right)$	–	8.1	29	0.70
$\omega_{LH}\tau_{ie}$	–	13	1.1×10^{10}	8.1×10^6
$V/\left(L\omega_{LH}\right)$	–	0.078	0.0058	0.17

Whilst the properties of plasmas in laboratory and space environments are often vastly different, through appropriate scaling of the relevant parameters involved, a comparison between the two environments can be made. In Table 3.1 the relevant plasma parameters for this experiment, a comet interacting with the Solar-wind, and the OSIRIS simulations performed for this experiment are compared. Since the properties of greatest interest are those relating to the production of lower-hybrid waves via the MTSI, the fluorine ions only have been considered. The parameters shown in Table 3.1 for the interaction of a comet with the Solar-wind were chosen with the following considerations in mind. The expanding gas cloud surrounding a comet

is mostly comprised of water and some carbon dioxide, meaning that the majority of the cometary ions involved are photo-ionized oxygen ions. The temperature of the ions varies between $\sim 0.02 - 0.2$ eV, and so a value of 0.1 eV seems appropriate. The Solar-wind comprises of a slow mode with speed ~ 100 km/s. The Solar-wind contains a magnetic field of $\sim 10 - 200$ μG and has ion temperatures of $\sim 1 - 10$ eV with electron densities of $1 - 10$ cm^{-3}. The parameters in the OSIRIS simulations are scaled to an electron density which matches the electron density in the experiment.

Table 3.1 shows that whilst many of the parameters such as cyclotron frequencies and gyro radii are very different between the laboratory and astrophysical cases, scaled quantities such as the ratio of gyro-radii to skin depth, are conversely quite similar. The product of the lower-hybrid frequency, ω_{LH}, and the ion-beam collision time, τ_{ie} is one way of comparing the growth of the instability. Clearly in collisionless situations such as space and in OSIRIS simulations, the large time-scale between collisions makes this quantity much greater than in the mildly-collisional laboratory case. On the other hand, a comparison between the period of the lower-hybrid wave oscillations and the time it takes for an ion to interact with a lower-hybrid wave (either V/r_{gi} or τ_{ie}, depending on which quantity is smaller), is similar for all three cases.

3.7 Conclusion

In this chapter the background, design and results of a laboratory astrophysics experiment have been described. The process of electron energization through the MTSI and lower-hybrid waves has been introduced, and an astrophysical setting for this process of a comet and Solar-wind interaction has been described. The experimental setup and results from both optical and X-ray diagnostics have been discussed and compared with hydrodynamics simulations. The energy of the non-thermal electron population, inferred from the X-ray diagnostics, has been determined through a mix-

ture of PIC simulations and theory. The PIC simulations additionally indicate that the electron energization process is indeed the result of the MTSI and lower-hybrid waves. Comparison of the experimental conditions and those within the comet and solar-wind highlights the differences between the mildly collisionless experimental results and the completely collisionless setting of space. This is suggestive that this experiment lends itself to future experiments at larger laser facilities where faster, more collisionless flows are permissible and so would produce larger electron energization, allowing the effects to be fully investigated. Work within this chapter is contained within an article accepted by Nature Physics [26].

Chapter 4

Technique for Making Faraday-Rotation Measurements at the OMEGA laser Facility

In this chapter a method for measuring magnetic fields at the OMEGA laser facility is described. The setup, calibration and analysis of a new Faraday rotation diagnostic is presented. A photometric calibration to determine the electron density is reported. Finally, the magnetic field found from the Faraday rotation diagnostic is compared with that determined from proton radiography.

4.1 Measuring magnetic fields

Measuring magnetic fields in plasmas is vital for a proper understanding of plasma dynamics, but such measurements are often difficult to implement. Among the diagnostics commonly implemented in laser-plasma experiments [110, 111, 112], only proton radiography, in which (quasi) mono-energetic protons are deflected in the plasma by magnetic fields, has been used with some success at the OMEGA laser facility [111]. Proton radiography often allows a spatially and time-resolved mea-

surement of the magnetic field. Whilst reconstruction of magnetic fields from proton radiography images is possible [74, 113], proton images are difficult to analyse, and the presence of caustic structures can make the reconstruction of the path-integrated magnetic field non-unique. Moreover, this method cannot distinguish easily between magnetic or electric field deflections. This is particularly important in plasmas where strong electrostatic turbulence is present along with magnetic field fluctuations. Alternative diagnostics such as induction probes [114, 109] or polarimetry [115] have been attempted on OMEGA, but they are either too invasive or lack the needed sensitivity for accurate measurements.

Here we describe an implementation of a Faraday rotation measurement that has a much higher sensitivity and can be used together with proton radiography for accurate field measurements. The diagnostic makes use of the Thomson scattering probe beam and so causes little disruption to the currently available diagnostics on OMEGA. The requirement is that $n_e\,[\mathrm{cm}^{-3}]\,B\,[\mathrm{kG}]\,L\,[\mathrm{cm}] \geq 2.4 \times 10^{20}$ kG cm^{-2}, where B is the magnetic field, n_e the electron density, and L the path-length of the probe beam. This requirement is due to the resolution of the Faraday rotation diagnostic, which is dependent upon the plasma's magnetic field and electron density and the probe beam path-length as determined by the experimental setup.

4.2 Experimental Setup

The Faraday rotation measurement was performed on a low-density turbulent plasma [116]. Two 6% chlorine-doped plastic foils were each irradiated with 351 nm, 5 kJ drive lasers in either a 5 or 10 ns pulse. This generated two counter-propagating plasma flows which then each passed through a plastic grid, and collided with one another at ~ 25 ns after the start of the laser drive. The velocity of these flows prior to their collisions is ~ 200 km/s. The turbulence that results from this collision is expected to produce dynamically significant magnetic fields through the turbulent

dynamo mechanism [116]with one another at $\sim$ 25 ns after the start of the laser drive.

The Faraday rotation measurement is built alongside the Thomson scattering diagnostics [117], and the setup allows for a coincident measurement of the magnetic fields with proton radiography. The Thomson scattering probe beam is a 30 J, 1 or 3 ns frequency doubled (526.5 nm wavelength) laser that probes the plasma within a 50 μm^2 region. To implement a Faraday rotation measurement, a Wollaston prism was inserted into the Thomson scattering beam, see Figure 4.1. The prism splits the beam into two polarization components, labeled S and P. The two polarizations are further split such that half of each signal goes to the ion-acoustic wave (IAW) channel, which resolves ion-acoustic fluctuations, and half to the electron-plasma wave (EPW) channel, which measures the total scattered power across all wavelengths. Both the IAW and EPW diagnostics are streaked in time with a 50 ps temporal resolution. The IAW diagnostic is spectrally resolved, whilst the EPW diagnostic is not spectrally resolved.

Proton radiography is implemented at the OMEGA laser facility using a D^{3}He capsule and CR-39 nuclear track detectors. Protons are generated by fusion reactions occurring by laser-driven implosion of a spherical capsule containing D^{3}He gas [118]. This releases mono-energetic protons with energies of 3.3 and 15 MeV (accounting for Doppler shift). The protons are emitted isotropically, and thus illuminate the interaction region of the two plasma jets (see Ref. [116] for additional details). The capsule is positioned far enough away from the plasma such that the protons pass through the plasma as a thin, planar sheet. Magnetic fields generated within the plasma will deflect the protons, which are then imaged onto the CR-39 plates. These proton radiographs can be used to infer the magnetic field structure [74] within the plasma at the time the protons passed through. In this manner, quantities such as the mean magnetic field can be readily determined from the proton radiographs and

then used as comparison and validation with the Faraday rotation diagnostic.

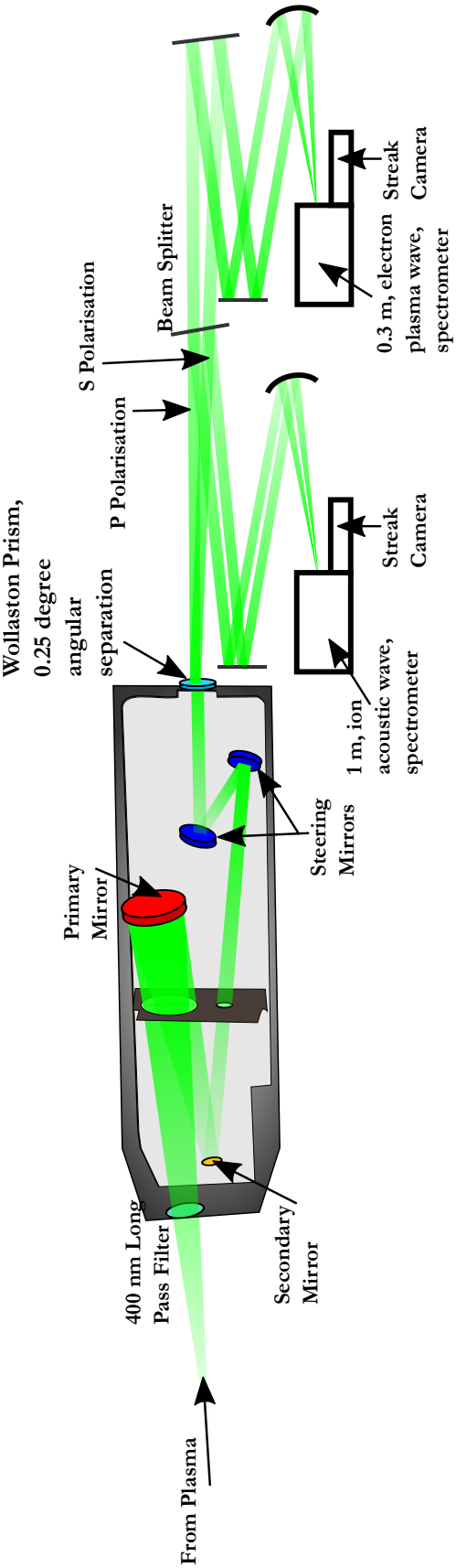

Figure 4.1: FRM setup: A 2ω, $1-3$ ns pulse probe beam is scattered from a 50 μm region of the plasma and is collected using f/10 collection optics. The collected scattered light enters the insertable polarimetry setup. Four mirrors within the configuration align the scattered light onto a quartz Wollaston prism which separates the two polarizations with a 0.25^o angular separation. The scattered light is then further split and focused onto two spectrometers. The ion acoustic wave spectrometer spectrally resolves both polarizations onto a streak camera. The electron plasma wave spectrometer measures the total scattered power across all wavelengths and so does not spectrally resolve the scattered light, and displays both polarizations onto a streak camera.

4.3 Analysis

Both the IAW and EPW diagnostics can be analysed in a similar manner with the same considerations in mind. The difference in intensity of the two polarizations depends on three different factors. First of all, in the absence of any magnetic fields, the relative intensity of the S and P polarizations are determined by the relative angle between the polarization of the light and the axis of the Wollaston prism. This angle is denoted by θ_c. In addition, the difference in intensity between the two polarizations also depends on the unequal response of the optics, detector and so on. Finally, when a magnetized plasma is present in the light path, the induced rotation of the polarization angle changes the angle at which the light enters the prism and thus the ratio of the two polarizations from when there is no magnetic field. The intensity of the two polarizations can be written:

$$I_S = I_0 A_S \sin^2(\theta_c + \Delta\theta), \tag{4.1}$$

and

$$I_P = I_0 A_P \cos^2(\theta_c + \Delta\theta), \tag{4.2}$$

where I_S and I_P are the intensities of the S and P polarizations, I_0 is the initial Thomson scattering laser intensity, A_S and A_P are the distinct transmission factors for each polarization, and $\Delta\theta$ is the rotation due to the magnetic fields. Taking the ratio of Equations 4.1 and 4.2 gives

$$\tan^2(\theta_c + \Delta\theta) = \frac{A_P I_S}{A_S I_P}. \tag{4.3}$$

Using Equation 4.3, the degree of Faraday rotation ($\Delta\theta$) can be determined, provided that the calibration angle θ_c, the ratio of A_S to A_P and the ratio of I_S to I_P is known. To determine the ratio of A_S to A_P, a measurement with no (or weak)

magnetic field was used. A half wave plate in front of the Wollaston prism is set such that the incoming polarization at the prism is $\theta_c = 45^o$. The axis of the Wollaston prism is set so that the two images from each polarization are separated along the streak camera input slit. The intensity of each polarization, I_S and I_P, is found by integrating over the total signal for each polarization.

As always, there is some stray light entering the detector. This light should not be included in the Faraday rotation analysis, since it has not been scattered and so has not been influenced by the magnetic fields within the plasma. The IAW data is spectrally resolved, and since the stray light occurs at the same wavelength as the probe beam, it can be separated from the Thomson scattered signal, which instead is shifted in wavelength as the probe photons interact with the plasma. In practice, however, isolating the stray light from the scattered signal is not always possible, if for example, the frequency shifts are such that there is still a large overlap between the two. Conversely, as the EPW measurement is not spectrally resolved, there is no obvious way to disentangle the stray light from the scattering measurement. In this case, the approach is to minimize as much as possible the stray light.

While the IAW and EPW data should give the same rotation angle, in the analysis there are other effects that could make the two measurements differ from one another. Stray light has already been mentioned and needs to be dealt carefully; either by isolating it from the sample data, as in the IAW case, or by checking that the stray light is small enough as in the EPW case. Additionally, the IAW data (being spectrally resolved) tends to be a lot noisier than the EPW data, and so the error in the measurement is larger.

4.4 Calibration

It is important to take a calibration shot that is expected to have no (or at least an undetectable) magnetic field. The calibration shot used here was a single plasma

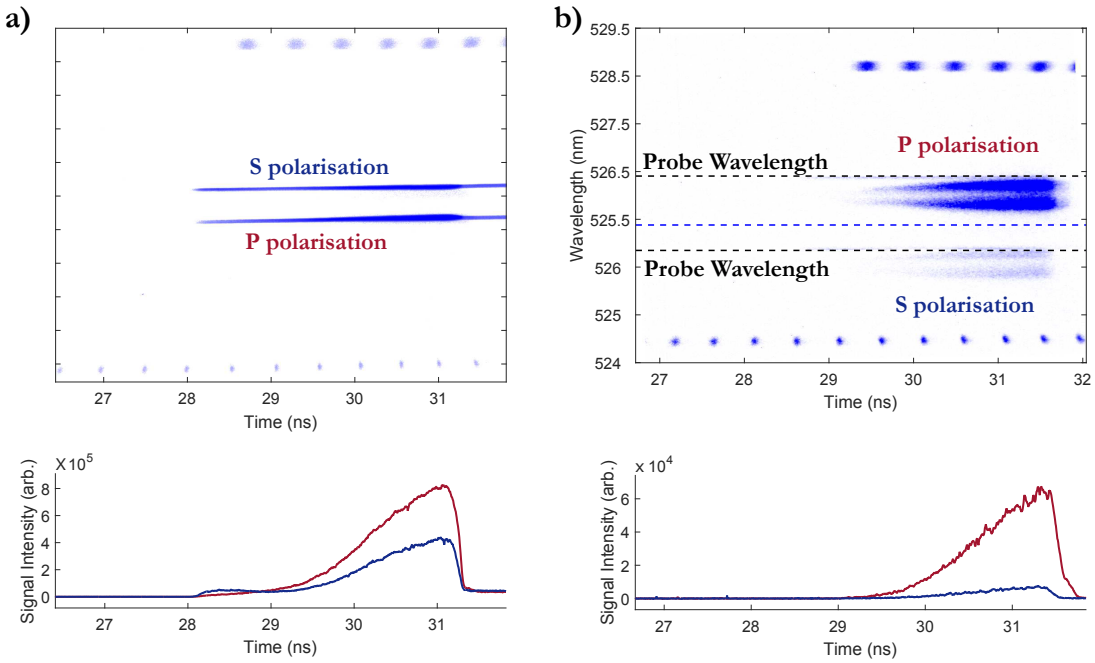

Figure 4.2: Calibration Shot: EPW (left) and IAW (right). In both images, the P polarization is positioned above the S polarization. The dots at the top and bottom of both images indicate timing fiducials and appear once every 1.1 ns and 0.548 ns respectively. The horizontal black dashed lines in the IAW image indicate the position of the probe laser. The horizontal blue dashed line in the IAW image represents the separation between the S and P polarizations and so indicates the break in the vertical wavelength axis. The lineouts underneath both images show the integrated signal of the P polarization (red) and S polarization (blue).

flow (where only one foil is irradiated and so there is no collision). The only magnetic fields present for this case are those from the seed fields generated from misaligned temperature and density gradients. These seed fields are small, $\lesssim 4$ kG [116], and below the detection threshold. There are of course caveats to using this calibration shot. It can be seen from the measured IAW signal, shown on the top of Figure 4.2b, that the stray light from the probe laser is significant. In particular, for the IAW, the wavelength of the stray light is close to the lower wavelength feature. As such, integrating across the entire signal (i.e., both ion-acoustic features) can give an incorrect result. Instead, only the lower (higher wavelength) peak should be considered in this case. Additionally, for this particular calibration shot, whilst the signal is not saturated on the CCD the signal has almost certainly saturated the

more sensitive streak camera later in time. Nevertheless, during the initial 1 ns, the signal remains unsaturated, has low noise and has a constant ratio between the two polarizations. Turning to the EPW data on the left-hand side of Figure 4.2, the two superimposed lineouts show the difference in the two polarizations. Again, the signal is likely saturated on the streak camera towards the end of the shot. However, for well over 1 ns of the shot, the signal is reliable and has an excellent signal to noise ratio and a constant ratio between the two polarizations. Overall, this shot is suitable to use as calibration: it is expected to have no magnetic field; high signal to noise; unsaturated signal for a large duration of the shot. It can be seen from the calibration shot that when the EPW data is good, it has far better signal to noise than the IAW data.

Figure 4.3 plots the initial angle θ_c obtained from equation 4.3 (when setting $\Delta\theta = 0$). By requiring that $\theta_c = 45^o$, this allows the ratio A_S/A_P to be found for both the IAW and EPW channels. This gives $A_{S_{IAW}}/A_{P_{IAW}} = 0.33 \pm 0.02$ and $A_{S_{EPW}}/A_{P_{EPW}} = 0.58 \pm 0.02$.

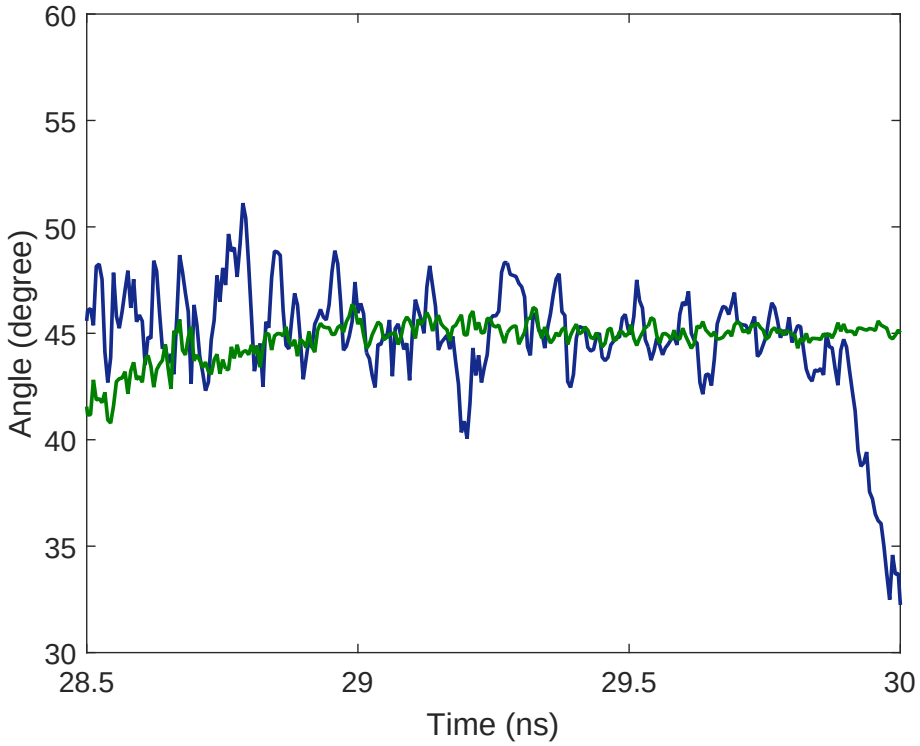

Figure 4.3: Calibration Shot: The resultant angle from both the IAW (blue) and EPW (green) data for the calibration shot. The calibration shot is a single-jet shot for which no measurable magnetic field is expected.

4.5 Data

In this section we will apply the Faraday rotation diagnostic to a few different data shots in order to measure the magnetic field during and after the collision of the two plasma flows. Data from Shot 1, taken 29.5 ns after the drive lasers are fired, is shown in Figure 4.4. The Thomson scattering probe has a 1 ns pulse duration and the IAW signal is saturated on the streak camera. The EPW data on the other hand is very good, with minimal noise, and it can be used to determine the magnetic field for this shot. In Figure 4.5, the calculated rotation angles ($\Delta\theta$) obtained from the IAW and EPW signals are reported. There is a significant difference between the two curves. As mentioned, this is likely due to saturation of the IAW signal on the

streak camera.

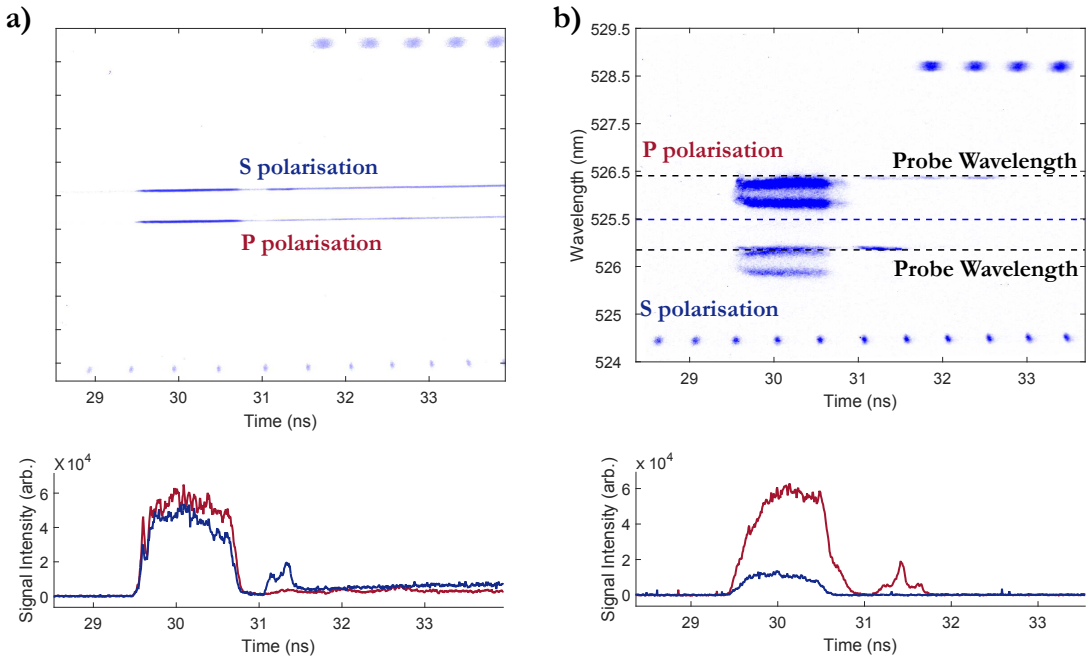

Figure 4.4: Shot 1: EPW (left) and IAW (right). In both images, the P polarization is positioned above the S polarization. The dots at the top and bottom of both images indicate timing fiducials and appear once every 1.1 ns and 0.548 ns respectively. The horizontal black dashed lines in the IAW image indicate the position of the probe laser. The horizontal blue dashed line in the IAW image represents the separation between the S and P polarizations and so indicates the break in the vertical wavelength axis. The lineouts underneath both images show the integrated signal of the P polarization (red) and S polarization (blue).

Shot 2, taken 32.5 ns after the drive lasers have been fired, also uses a 1 ns long probe beam and it is shown in Figure 4.7. The signal is much weaker than for shot 1. Figure 4.7 shows the resultant rotation angles extracted from IAW and EPW traces. We notice again that EPW gives a much better signal to noise ratio, and thus allows for a more precise determination of the rotation angle $\Delta\theta$.

Once the Faraday rotation angle has been determined, the magnetic field within the probe beam's path can be calculated. The Faraday rotation angle is given (in Gaussian units) by [119]

$$\Delta\theta = \frac{\lambda^2 e^3}{2\pi m_e^2 c^4} \int_0^{2L} n_e(s)\, B_{\parallel}(s)\, \mathrm{d}s. \tag{4.4}$$

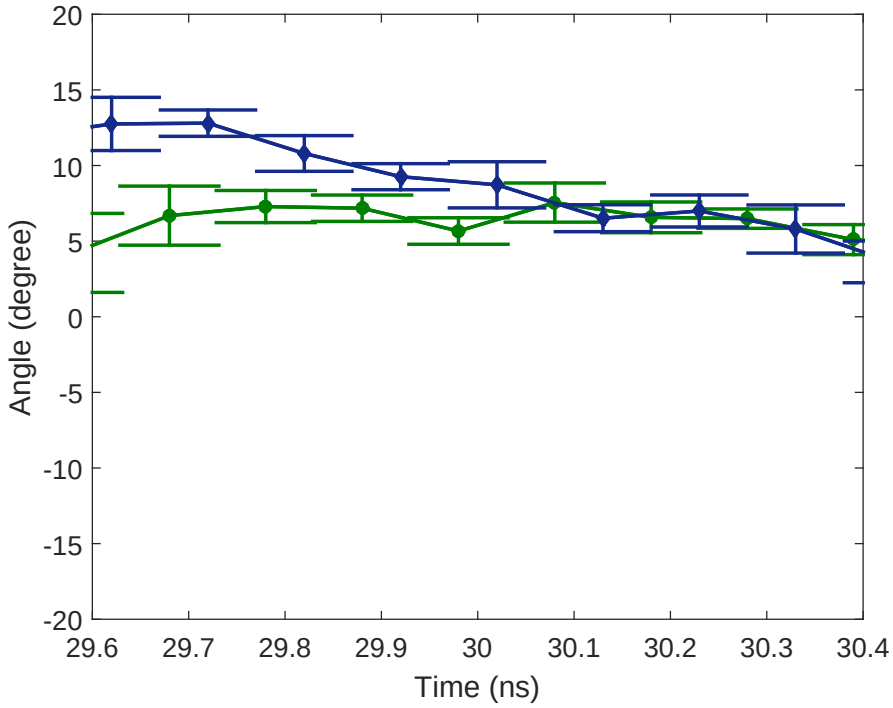

Figure 4.5: Shot 1: Resultant angle from the IAW (blue) and EPW (green) data for Shot 1 averaged over 100 ps.

It is appropriate to use twice the size of the plasma, L, for the path length of the integral because the experimental geometry is such that the scattered beam lies on the opposing side to that from which the probe beam originates. The incident laser's wavelength is $\lambda = 526.5\,\mathrm{nm}$, and so implies

$$\int_0^{2L} n_e(s)\, B_{\parallel}(s)\, \mathrm{d}s = 2.4 \times 10^{23} \Delta\theta\, \mathrm{G\ cm^{-2}}. \tag{4.5}$$

Equation 4.5 indicates that once the Faraday rotation angle and electron density are known, the path-integrated field can be determined. The Faraday rotation diagnostic can resolve 1^o of rotation and so, as previously mentioned, the requirement for the diagnostic to capture a change in magnetic field is $n_e\,[\mathrm{cm^{-3}}]\, B\,[\mathrm{kG}]\, L\,[\mathrm{cm}] \geq 2.4 \times 10^{20}\ \mathrm{kG\ cm^{-2}}$.

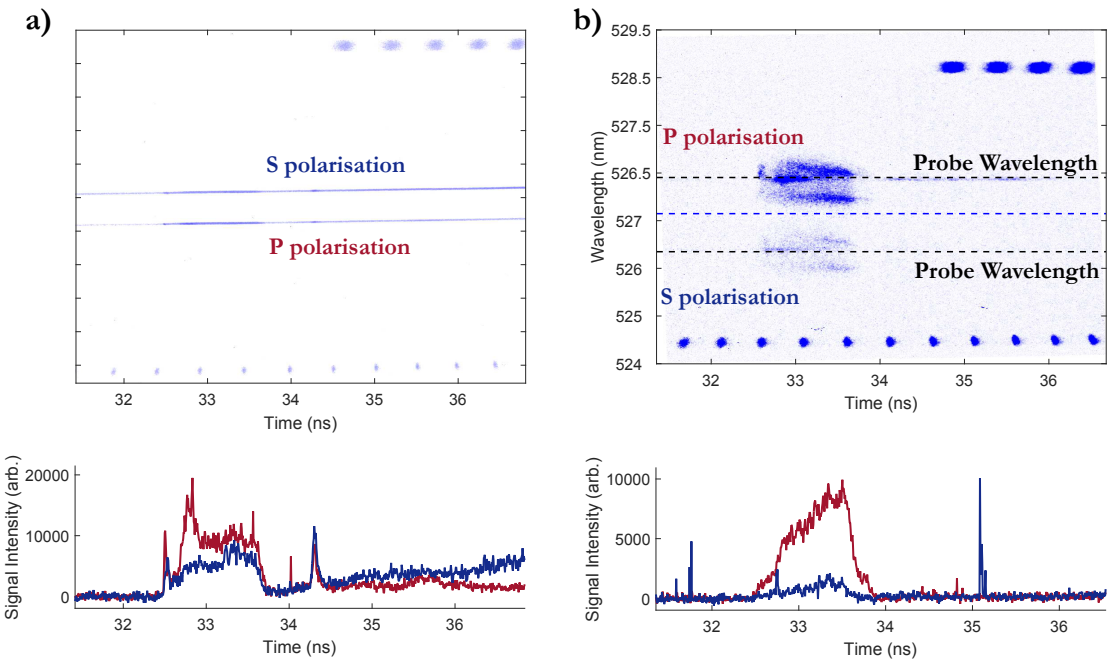

Figure 4.6: Shot 2: EPW (left) and IAW (right). In both images, the P polarization is positioned above the S polarization. The dots at the top and bottom of both images indicate timing fiducials and appear once every 1.1 ns and 0.548 ns respectively. The horizontal black dashed lines in the IAW image indicate the position of the probe laser. The horizontal blue dashed line in the IAW image represents the separation between the S and P polarizations and so indicates the break in the vertical wavelength axis. The lineouts underneath both images show the integrated signal of the P polarization (red) and S polarization (blue).

To determine the electron density, we have employed a full photometric calibration of the IAW channel, as shown in Figure 4.8. This allows for the integrated number of counts on the detector to be converted into the total scattered power. To complete the full photometric calibration, a 2ω fiducial laser was used. The amount of light coupled through the Thomson scattering telescope was measured using an energy meter and then cross referenced to a pick-off monitor at the start of the laser path. Laser pulses were then recorded on the Thomson scattering system and the energy measured through the cross calibrated energy meter. Transmission of the Thomson scattering probe beam through the Faraday rotation package was characterized separately and then included in the final calibration. The counts registered on the IAW spectrometer could then be converted to a value for the total scattered

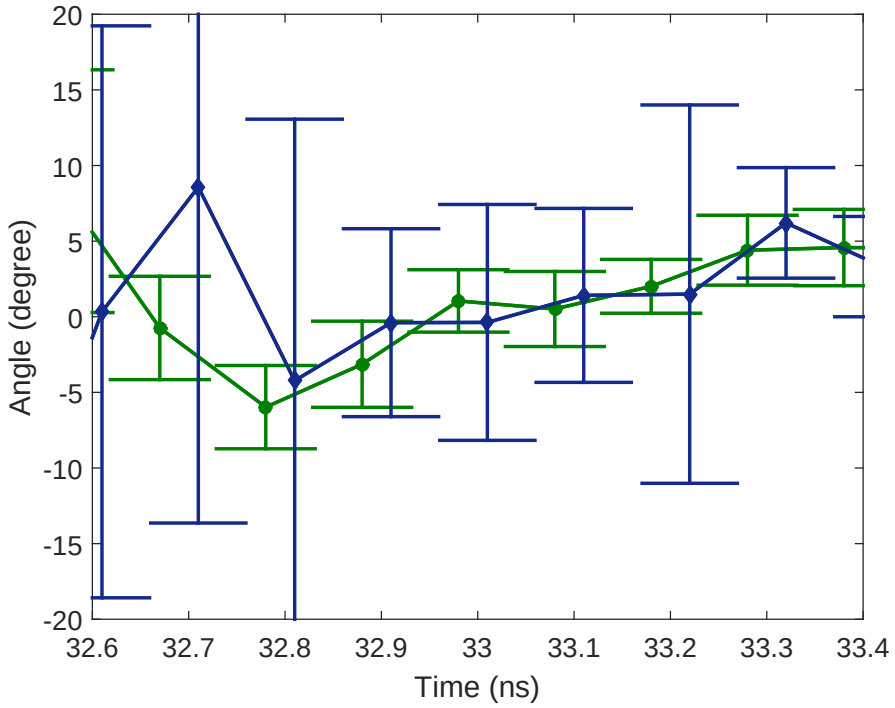

Figure 4.7: Shot 2: Resultant angle from the IAW (blue) and EPW (green) data for Shot 2, averaged over 100 ps. The IAW data is much noisier than the EPW data because the S polarization is very weak. Despite the noisiness in the IAW data, the EPW and IAW data have a similar angular distribution.

power.

The total scattered power can be used to determine the electron density via

$$P_S = P_I \, d\Omega \, r_0^2 \frac{\ell_{TS}}{2\pi} \left| \hat{\mathbf{s}} \times \left(\hat{\mathbf{s}} \times \hat{\mathbf{E}}_{\mathbf{i0}} \right) \right|^2 S(k) Z^2 n_i, \tag{4.6}$$

where P_S is the scattered power, P_I the incident power of the probe beam, $d\Omega$ the collecting solid angle, $r_0 = 2.818 \times 10^{-13}$ cm the classical electron radius, $\ell_{TS} = 50$ μm the interaction length, $\hat{\mathbf{s}}$ the unit Poynting vector, $\hat{\mathbf{E}}_{i0}$ the probe beam's electric field unit vector, $S(k)$ the spectral density function, Z the mean ion charge and n_i the ion density. The incident power is provided by the on-shot calorimetry performed at the OMEGA laser facility. The effective f-number of the collection optics was 9.1,

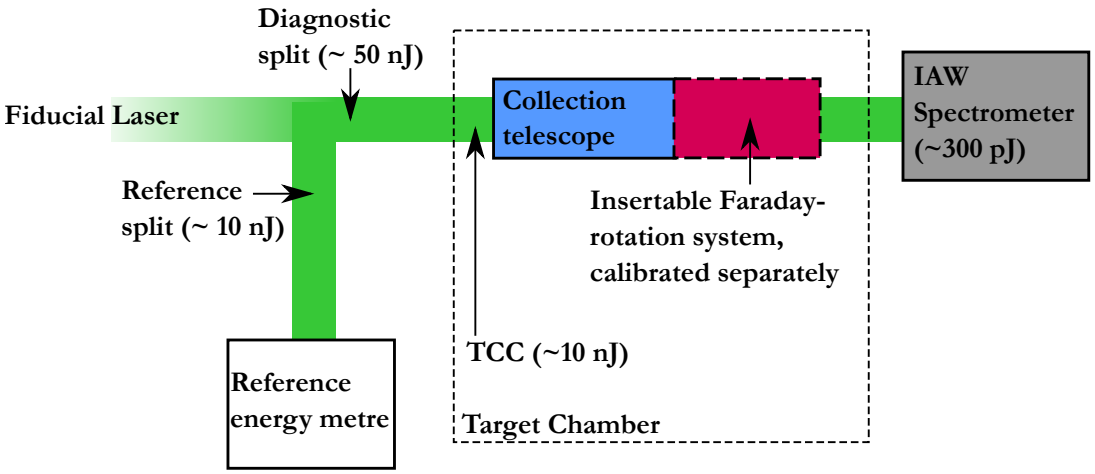

Figure 4.8: Schematic of photometric calibration setup: Scattered light from the Thomson scattering probe beam is deposited onto the IAW streak camera and recorded on a CCD as pixel counts. Initially, an energy meter is placed at the position of the IAW streak camera and records the energy of the fiducial beam once it has passed through the vacuum chamber and Thomson scattering collection optics (but not the Faraday rotation optics). The measured transmitted energy of the fiducial laser is used to calibrate a reference energy meter which records a pick-off of the fiducial laser, taken before the fiducial laser enters the vacuum chamber. The reference energy meter can then be used to determine the energy of the transmitted fiducial beam at the IAW spectrometer position. The IAW spectrometer is returned to its standard position and the transmitted energy of the fiducial laser is recorded on the IAW spectrometer as pixel counts. The reference meter then indicates the total transmitted energy to the IAW spectrometer and so a relationship between the energy transmitted to and the number of counts registered on the IAW spectrometer can be determined. Finally, the Faraday rotation setup (Wollaston prism and turning mirrors) was characterized outside of this setup, by recording the reduction in the probe beam energy due to the Faraday rotation optics, which could then be included in the final calculation.

giving a solid angle of 10^{-2} sr. The spectral density function is [66, 120]

$$S(k) = \frac{Z\alpha^4}{(1+\alpha^2)[1+\alpha^2(1+Z)]}, \tag{4.7}$$

which can be obtained using the spectral fit to the ion feature as shown in Figure 4.9. Here α is $1/k\lambda_D$, where λ_D is the Debye length. An average ionisation of $Z = 3.5$ is expected for CH plasmas (that is, both species are fully ionized). From this photometric calibration the electron density is found to be $\sim 7 \times 10^{19}$ cm^{-3}. On a similar experimental setup where no Faraday rotation diagnostic was present and so the electron features could be spectrally resolved, the electron density could

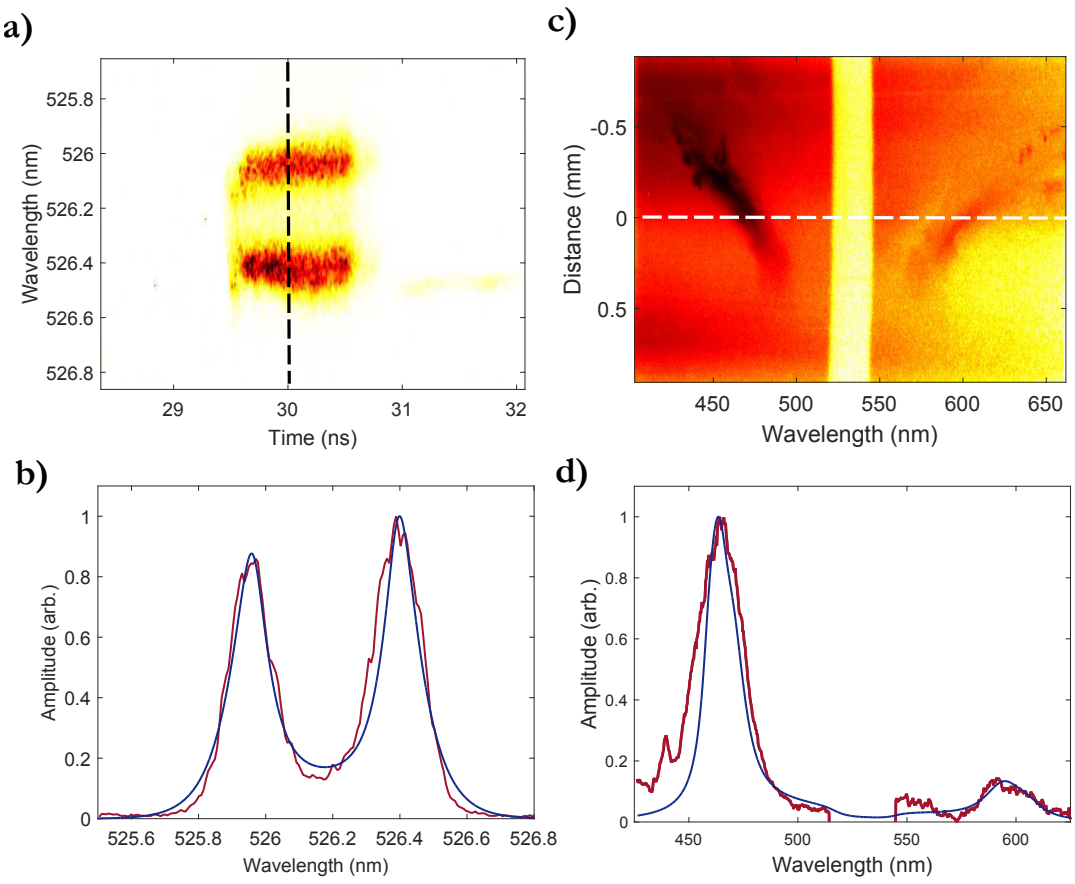

Figure 4.9: Determining electron density and temperature: a) An IAW image that can be used to determine the electron temperature of the plasma. This shot spectrally (vertical axis) and temporally (horizontal axis) resolves the ion features. A Thomson scattering spectra can then be fitted by eye to this data to determine the electron temperature and so, through the full photometric calibration, determine the electron density for each Faraday rotation shot. The black dashed line indicates where the lineout in b) is taken. b) Lineout of raw data (red) from a) with fitted spectra (blue) indicating an electron temperature $\sim$ 300 eV. Its been assumed that the electron density is $\leq 10^{20}$ cm^{-3}, that the ion and electron temperatures are equal and that the plasma is fully ionized, giving an ionization $Z \sim 3.5$. c) An EPW image that can be used to determine the electron density. This shot spatially (vertical axis) and spectrally (horizontal axis) the electron features and so a fitted Thomson scattering spectra can be found to determine the electron density. Aside from the differences in the EPW diagnostic, the experimental setup for this shot is the same as those shown previously with Faraday rotation data. The white dashed line indicates where the lineout in d) is taken. d) Lineout of raw data (red) from c) with fitted spectra (blue) indicating an electron density $\sim 5 \times 10^{19}$ cm^{-3}, similar to the value found in the full photometric calibration.

be determined by fitting the Thomson scattering spectrum to the position of the electron plasma waves. as shown in Figure 4.9. In this case, the electron density was found to be 5×10^{19} cm^{-3}, similar to the value found from the photometric calibration.

Having determined the electron density and rotation angle, the path-integrated magnetic field from the Faraday rotation measurement can be calculated using Equation 4.5. For this experiment, an effective path-length of 0.02 cm then gives a magnetic field of 40 kG and 160 kG for Shots 1 and 2 respectively. These data shot values are well above the 4 kG seed values of the calibration shot.

4.6 Comparison with Proton Radiography

The accuracy of the Faraday rotation diagnostic can be characterized through comparison with proton radiography, a diagnostic already commissioned at the Omega laser facility [121, 122, 123]. Proton radiography was performed on the same shots as those discussed previously. Faraday rotation and proton radiography probed the plasma at essentially the same time, to within 2 ns, which is much shorter than the hydrodynamic eddy turnover times at the largest scale, and so they both probe the same magnetic field structures. The path-integrated magnetic field reconstruction[74] from the proton radiographs show the entire interaction region, as opposed to the 50 μm^2 area sampled by the Faraday rotation diagnostic, as shown in Figures 4.10 and 4.11. As such, the proton radiographs can provide both a mean path-integrated field estimate for the entire region as well as the maximum path-integrated field produced at the time of the radiograph. To make a fair comparison between the two diagnostics, the mean-field from the proton radiography images is calculated within a 200 km/s $\times$2 ns $\sim$ 4 mm square region. This region is the extent that the two 200 km/s plasma jets could travel within the 2 ns difference in diagnostic timing. Additionally, because of the geometry of the experimental setup, the Thomson scattering beam

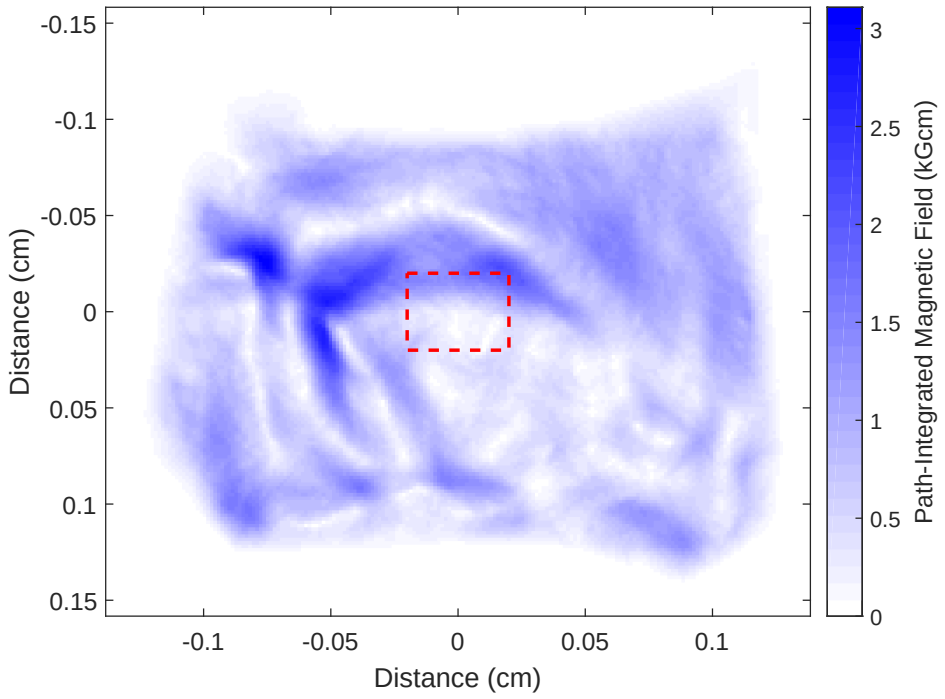

Figure 4.10: Shot 1: Reconstructed magnetic field for Shot 1. The red dashed lines indicate the extent the plasma within the Thomson scattering region can travel within the 2 ns delay between the proton radiograph and Thomson scattering measurements assuming the plasma travels at 200 km/s. The mean field within this red square is used for comparison with the Faraday rotation diagnostic. This magnetic field reconstruction was performed by A. F. A. Bott.

experiences about twice the path-length that the protons encounter. Accordingly, to fairly compare the two diagnostics, the path-integrated magnetic field measured by the Faraday rotation diagnostic is reduced by a factor of $\sqrt{2}$.

Figure 4.12 shows how the results from Faraday rotation and proton radiography compare with one another. Both the mean path-integrated magnetic field within the Thomson scattering region and the maximum path-integrated magnetic field as calculated from proton radiography are plotted in the figure. The Faraday rotation path-integrated magnetic field for each shot is estimated from the average rotation angle within the 1 ns of signal.

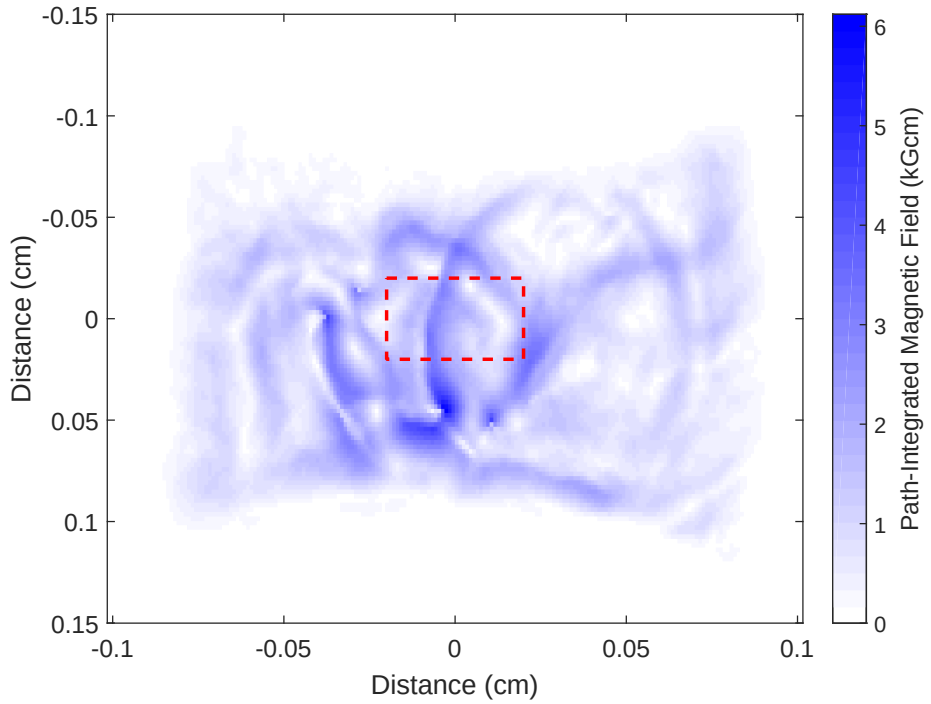

Figure 4.11: Shot 2: Reconstructed magnetic field for Shot 2. The red dashed lines indicate the extent the plasma within the Thomson scattering region can travel within the 2 ns delay between the proton radiograph and Thomson scattering measurements assuming the plasma travels at 200 km/s. The mean field within this red square is used for comparison with the Faraday rotation diagnostic. This magnetic field reconstruction was performed by A. F. A. Bott.

The error bars in the proton radiography inferred mean path-integrated field are found by sampling different 4 mm square regions throughout the reconstructed radiograph. There is an additional error of around 20% inherent in the reconstruction algorithm which is included; this uncertainty is the result of approximations employed in the derivation of the algorithm. The error from the Faraday rotation measurement comes from both the variability in the measured rotation angles and due to inferring the electron density from the absolute calibration. The main source of uncertainty in the Faraday rotation measurement is due to the electron density which is known to within $\sim 20\%$. Whilst the small difference in timing between the two diagnostics

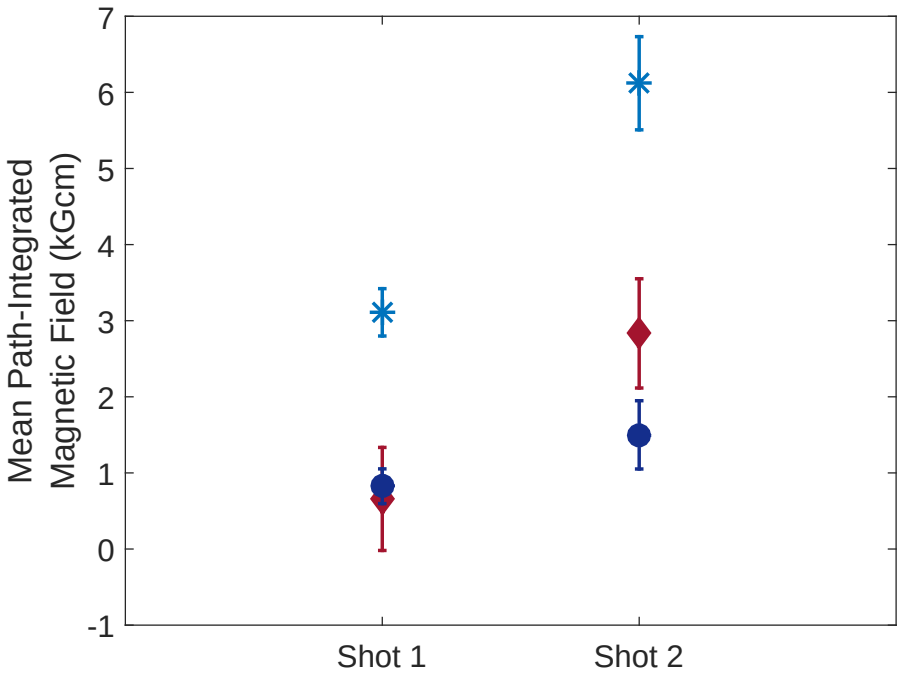

Figure 4.12: Comparison with Proton radiography: The FRM calculated path-integrated magnetic-field (red diamonds) for the shots described are compared with the path-integrated magnetic fields calculated from proton-radiography (blue circles) for the same shots. The largest path-integrated field structure recorded by proton-radiography (light-blue stars) is plotted for comparison.

allows for changes within the path-integrated magnetic field to occur, there is a close similarity between the mean path-integrated field inferred from the two diagnostics. Additionally, the mean path-integrated field calculated from Faraday rotation is consistently smaller than the maximum path-integrated field found from the proton radiography reconstructions, as expected. The similarity in the mean magnetic-field as calculated from the two diagnostics gives confidence in the results of both diagnostics, suggesting that Faraday rotation can indeed be used for on-shot analysis throughout a shot day at the Omega laser facility.

4.7 Conclusion

A new Faraday rotation diagnostic has been fielded at the OMEGA laser facility. The analysis of the results has been described and a comparison made with the results from proton radiography. The Faraday rotation results are similar to those from proton-radiography. One substantial advantage of this diagnostic is the fact it does not rely on films or passive detectors (as CR-39). As such, analysis can be performed immediately after the shot, allowing for magnetic field measurements to be performed in real time during the experiment. The work within this chapter is contained within an article submitted to High Power Laser Science and Engineering special edition on Laboratory Astrophysics [124].

Chapter 5

Characterizing the Properties of Colliding Turbulent Jets with Thomson Scattering

In this chapter, the results from the Thomson scattering diagnostic at a recent campaign at the OMEGA laser facility are discussed. An overview of the experimental campaign's goals are presented, with particular focus on the role of the Thomson scattering diagnostic. The sensitivity of the Thomson scattering data to different plasma quantities such as electron temperature and flow velocity is described. The results from the Thomson scattering data, with different target material compositions are presented. The resultant plasma parameters are then calculated and the interaction between the colliding jets described. The effect of various quantities on the plasma parameters is predicted theoretically and is then compared with the experimental observations from the different target compositions.

5.1 The Turbulent Dynamo Campaign

The results from the OMEGA experiment described within this chapter are the result of an extensive campaign to understand how astrophysical magnetic fields are amplified to their observed values. A series of experiments have discussed the generation of magnetic fields [109] and how these seed fields can then be amplified through a turbulent medium [125, 114]. The interest in this astrophysical problem stems from the fact that the universe is ubiquitously magnetized [16, 126]. However, galactic magnetic fields observed through Faraday rotation [57, 127, 128] are much larger than would be expected solely from a seed field generated through, for example, misaligned density and temperature gradients (i.e., the Biermann battery mechanism). Consequently, the comparatively large astrophysical magnetic fields are thought to be the result of an amplification process such as a turbulent dynamo mechanism [129, 14, 15, 16, 17].

This dynamo mechanism, in general, occurs in astrophysical plasmas although it is difficult to obtain observational evidence [130]. Initially, a weak magnetic field is present within the plasma. Turbulent motions which are the result of, for example, the shock at a supernova remnant [131], cause the plasma to twist and fold in on itself. Astrophysical plasmas tend to have large magnetic Reynolds numbers and so turbulent motions stretch, twist and fold the magnetic field lines with are flux frozen into the plasma due to the high Rm (i.e., small magnetic diffusivity) and thus the magnetic field strength increases exponentially. Eventually, the energy within this amplified magnetic field becomes dynamically significant to the motion of the plasma at which point the magnetic energy within the plasma continues to grow linearly and then saturates. This is what is known as the turbulent dynamo mechanism for magnetic field amplification.

Whilst there are many numerical and theoretical studies that discuss the implications and nuances of the turbulent dynamo mechanism [17, 14, 62], observing this

within the laboratory has proven difficult. This difficulty can be explained by considering that laboratory dynamo experiments use either liquid metals or plasmas. The electrical conductivity of liquid metals makes reaching high magnetic Reynolds numbers difficult. Conversely, hot plasmas are much better electrical conductors and are therefore capable of reaching high magnetic Reynolds numbers, but they tend to be magnetically confined in fusion devices with gas-to-magnetic pressure ratios $\beta \ll 1$, and are therefore unsuitable to study how they became strongly magnetized initially. The goal of the experimental campaign undertaken at the OMEGA laser facility was to observe the turbulent dynamo mechanism within the laboratory. Through a combination of simulations [132] and several experimental shot days, laboratory evidence for the turbulent dynamo mechanism was achieved [18].

The experiment hosted a large number of diagnostics to confirm this result including proton radiography, Faraday rotation, X-ray imaging, and Thomson scattering. The proton radiographs and X-ray images were used to extract the magnetic field power spectra and kinetic energy power spectra (by relating fluctuations in X-rays intensity to density variations [133]), thus enabling the characterization of the turbulent plasma. Proton radiography and Faraday rotation independently provide a measurement of the magnetic field and therefore quantify the amplification. Thomson scattering enabled the plasma properties to be fully characterized.

The experimental campaign has so far completed 3 shot days, throughout which several experimental variables have been altered. Here, the results from the Thomson scattering diagnostic will be discussed for all shot days. These results provide information on the interaction of the colliding plasma flows and the turbulent plasma their collision produces, crucially including an estimate for the magnetic Reynolds number within the plasma. The effects of experimental changes, such as target composition, on the plasma flows will be presented and compared against theoretical expectations.

5.1.1 The OMEGA Experiment

A schematic of the experimental setup is shown in Figure 5.1a. Two foils, 8 mm apart, were irradiated with ten, 500 J, 1 ns, frequency tripled (351 nm) laser beams, each with an 800 μm spot diameter. The beams are stacked in time to produce either a top-hat like 10 ns pulse or a 5 ns pulse that ramps up in intensity throughout the laser-drive, see Figure 5.1b. The two foils are made of plastic (CH) and either doped with 6%, 1% or 0% Chlorine, in atomic number. The two laser-produced plasmas flow towards one another but are each perturbed by the presence of a grid. The grids are placed 4 mm apart, equidistant from the mid-point of the two foils and are 250 μm thick and 3 mm wide. The grids have a variety of hole spacings and wire thicknesses, either 300 μm holes and 300 μm wires (labeled AB$-$1), or 300 μm holes and 100 μm wires (labeled AB$-$2). The two grids are designed such that along the axis between the two foils, the central hole of one grid opposes the central wire of the other grid.

The Thomson scattering diagnostic is implemented by a 30 J, frequency doubled (526.5 nm) probe beam with a 50 μm focal spot. Thomson scattering was set up such that the scattered light was collected with a 63^o scattering angle and the resultant scattering wavenumber was parallel to the plasma flow, see Figure 5.1c. To attain a magnetic field measurement, the Thomson scattered light was split with a Wollaston prism into two polarisations to generate a Faraday rotation setup (see Chapter 4 and [124] for more details).

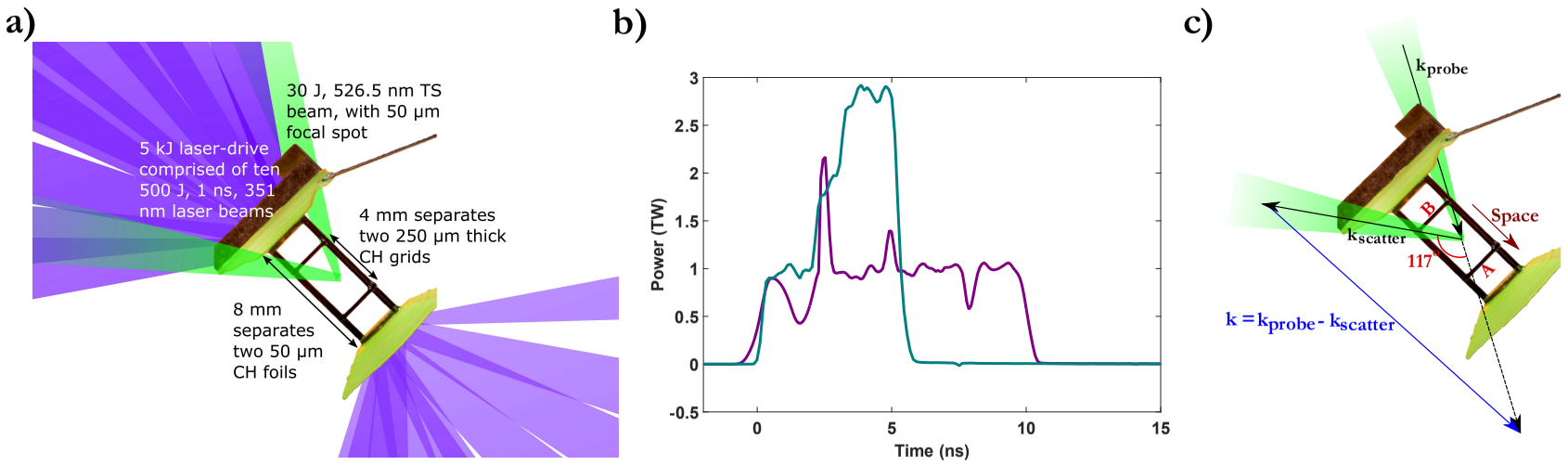

Figure 5.1: Experimental Setup: a) Two sets of ten 500 J, 1 ns, frequency tripled (351 nm) laser beams each irradiate a foil with focal spot diameter $\phi = 800$ μm. The two foils are arranged 8 mm apart, opposite one another and are predominantly plastic (CH) with a Chlorine doping of 0%, 1% or 6% by atomic number. The foils were 50 μm and had 230 μm washers to collimate the flows. The two resultant plasma flows from the back surfaces are then each perturbed by a grid. The grids are plastic (CH_2), 3 mm in diameter and 250 μm thick and are placed 4 mm apart from one another, equidistant from the middle of the two foils. The grids have either 300 μm thick wires and 300 μm wide holes; or 100 μm thick wires and 300 μm wide holes. The grids are oriented such that along the centre of the foil axis, the centre of one grid's hole is directly opposite the centre of the opposing grid's wire. The two plasma flows then collide and interact in between the two grids. The resultant turbulent plasma is probed using a 30 J, frequency doubled (526.5 nm) Thomson scattering beam with a 50 μm focal spot. The Thomson scattering beam is either 0.6 ns, 1 ns or 3 ns long and is either temporally or spatially resolved. Thomson scattering is set up such that the scattering angle between the incident and scattered light is 63^o and the resultant scattered wavenumber is along the axis of the flow (foil axis). The photograph of the target used in this figure was taken by E. Kowaluk. b) The two different pulse shapes for a 10 ns laser drive (blue) and a 5 ns laser drive (purple). The laser beams are combined together to give either a 10 ns flat-top pulse or a 5 ns pulse with a step-like ramp (i.e., the first two ns have one laser beam each, the third ns has two laser beams and the fourth and fifth ns have three laser beams each). c) Thomson scattering wavevectors. Resultant wavevector, $\mathrm{k} = \mathrm{k}_{\mathrm{probe}} - \mathrm{k}_{\mathrm{scatter}}$, ensures that the plasma velocity along the flow velocity can be detected by the Thomson scattering diagnostic. The red arrow indicates the spatial axis direction, used in additional Figures. 'A' and 'B' indicate labeling of the two grids.

5.2 Thomson Scattering Diagnostic

The Thomson scattering data was taken over multiple shot days allowing for several changes in the diagnostic to be made between the shot days as shown in Table 5.1. Throughout all the shot days, a proton radiography diagnostic was used. The laser beams that backlight the D3He capsule which produces the fusion-reacted protons for proton radiography are required by the OMEGA laser facility to be the same pulse length as the Thomson scattering probe beam. When the Thomson scattering diagnostic was temporally resolved over 1 or 3 ns, the Thomson scattering region was 50 μm^2. When the Thomson scattering diagnostic was spatially resolved, the probe beam was 0.6 ns in duration. The spatially resolved data is then collected across the entire region of the plasma.

The composition of the target foils changed between the different shot days. In the first shot day, the CH foils were doped with either 1% or 6% Chlorine by atomic number. In the second and third shot days, the foils were purely CH and had no dopant. On all shot days, a laser-drive of 10 ns was incident on each foil. On the first shot day, some of the shots had a stacked laser-drive of 5 ns.

Table 5.1: Summary of Shot days: Thomson scattering data is either temporally-resolved (TR) or spatially-resolved (SR). Whilst all shots have data from the ion-acoustic waves (IAW), each shot can have either have data from electron-plasma waves (EPW) or Faraday-rotation measurements (FRM) but not both. The target material and laser-drive change throughout the shot days. Grid type AB−1 indicates 300 μm holes and wires whilst AB−2 grids have 100 μm wires and 300 μm holes.

Year	TS	FRM	IAW	EPW	Target	Drive	Grid
2015	TR	✓	✓	×	Chlorinated	5 and 10 ns	AB−1
2016	TR	✓	✓	×	No Chlorine	10 ns	AB−2
2017	SR	×	✓	✓	No Chlorine	10 ns	AB−2

Thomson scattering data can yield a wealth of information about the plasma [72]. The information gained from the ion and electron features is usually different i.e., the ion features are very sensitive to electron temperature and insensitive to electron density.

5.2.1 Thomson Scattered Ion Features

In the collective scattering regime, the Thomson scattered ion features have two peaks [66]. By fitting the Thomson scattering data with a tailored version of the code in [72], the different plasma parameters can be found. A fully fitted spectrum is shown in Figure 5.2a.

Bulk flow velocity

The bulk flow velocity can be found from a global shift of the scattering features from the probe laser wavelength as shown in Figure 5.2b. Positive flow velocity is in the direction away from the scattering vector towards Grid B, as shown in Figure 5.1c.

Electron temperature and ionisation

The product of electron temperature, T_e, and ionisation, Z, can be found from the separation of the two ion acoustic peaks. The two resonances occur from the ion-acoustic dispersion relation and so their separation is set by the sound speed which depends on T_e and Z. These plasmas have an electron temperature of a few hundred eV and so are almost fully ionised. It can be confirmed through the collisional-radiative code PrismSPECT [79] that for an electron temperature of 200 eV and electron density of 10^{20} cm^{-3} that the ionisation of carbon, hydrogen and chlorine is 6, 1 and 14 respectively. Once the ionisation is known, the separation of the two peaks depends only the electron temperature.

Reducing the ionisation for carbon from 6 to 3 dramatically changes the spectrum as shown in Figure 5.2c. Note that if a reduced ionisation was used, a larger electron temperature would be required to attain the same peak separation. Such a large electron temperature would then generate a fully ionised plasma, and so the reduced ionisation assumption would be incorrect.

Changing the electron temperature moves the ion acoustic peaks closer together or further apart as shown in Figure 5.2d.

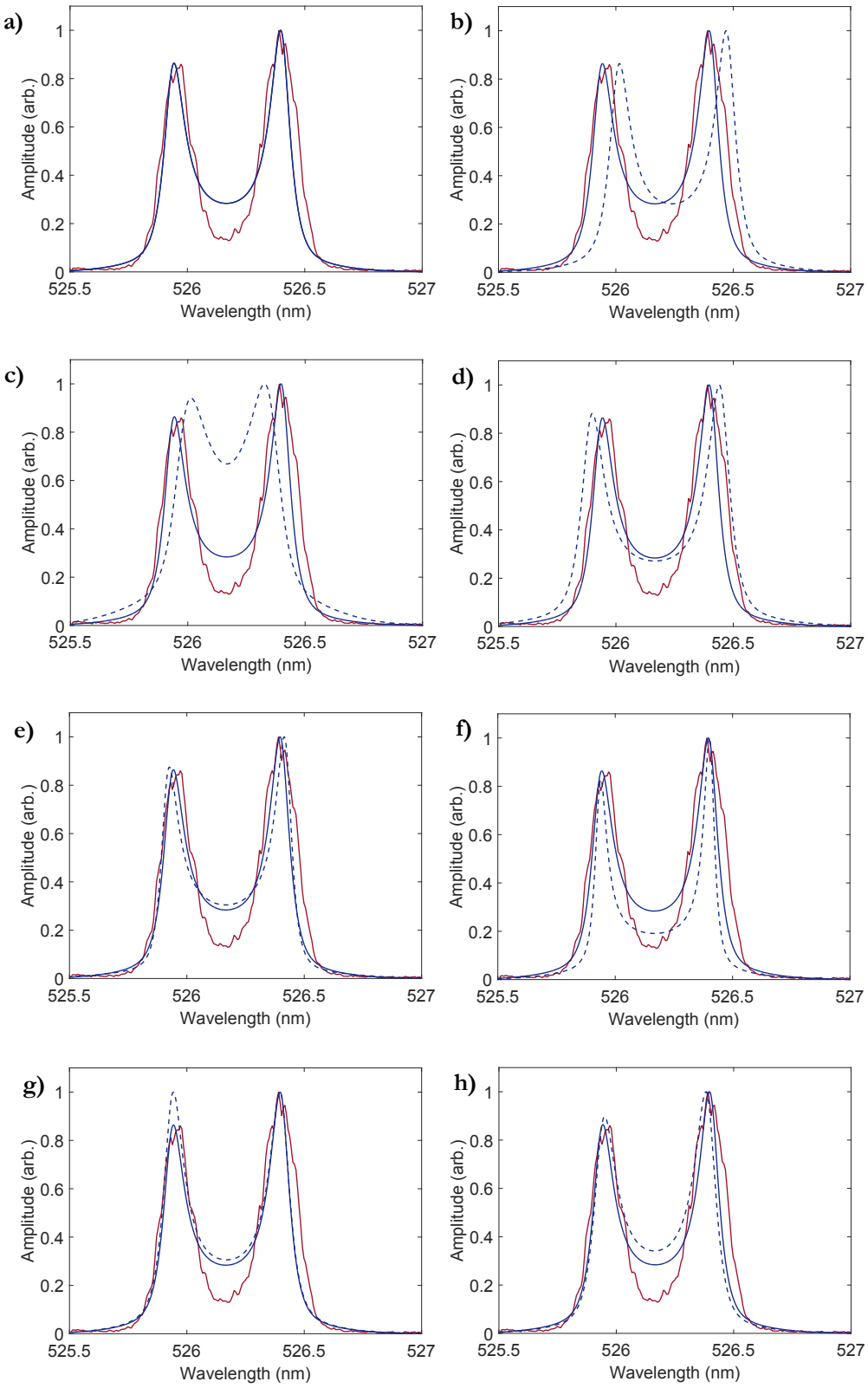

Figure 5.2: Fitted ion features: a) Thomson scattering data (red solid line) is compared with a predicted spectra (blue solid line). The predicted spectra has a flow velocity of 185 km/s, electron and ion temperature of 240 eV, fully ionised Carbon, turbulent velocity of 35 km/s, relative drift velocity of 100 km/s and an electron density of 10^{20} cm^{-3}. b)-h) are the same as a) with an additional fit (blue dashed line) that has: b) a flow velocity of 145 km/s, c) Carbon ionization $Z = 3$, d) an electron and ion temperature of 340 eV, e) an ion temperature of 340 eV and no turbulent velocity, f) no turbulent broadening, g) no relative drift velocity between the electrons and ions and h) an electron density of 10^{19} cm^{-3}.

Ion temperature

Throughout the following, it is assumed that the electron and ion temperatures are equal. This is a valid assumption because the ion and electron equilibration times are such that by the time the Thomson scattering measurements are made, the ions have had time to thermalize. To check, if the ion and electron temperatures are taken to be non-equal, the ion temperature is then required to fit the broadened ion acoustic peaks as shown in Figure 5.2e. The consequent ion temperature is much larger than the electron temperature which is unphysical since the ions thermalize more slowly than the electrons due to their increased mass.

Turbulent Velocity

The ion acoustic peaks can be Doppler broadened by the plasma. Arguably, the width of the peaks should give a measurement of the ion temperature. However, in this case the ion-electron equilibration time scale is such that by the time the two jets collide, the ion and electron temperatures should be equal. As shown in Figure 5.2f, when no additional broadening mechanism is present, the peaks are too thin. In this experiment, it is expected that the dominant broadening mechanism is through turbulent motions. The broadening due to turbulent motions is added through a convolution with a Gaussian of the form $\sim \exp\left(-\frac{1}{2}\left(\frac{\lambda-\lambda_0}{\lambda_{turb}}\right)^2\right)$ where λ is the scattered wavelength, λ_0 is the probe beam wavelength and λ_{turb} is the turbulent broadening. To relate λ_{turb} to the turbulent velocity v^0_{turb} [134],

$$\frac{\lambda_{turb}}{\lambda_0} \sim \frac{v^0_{turb}}{c}. \tag{5.1}$$

The turbulence within this plasma can be considered to consist of eddies of different sizes up to a large, outer scale, L, which is set by the grid size. The turbulent velocity at this small 50 μm scale should be converted into a turbulent velocity, v_{turb}, at the outer scale of the plasma (and so fairly compare it to other plasma parameters). For a high Reynolds number flow, a Kolmogorov scaling [59] of $\left(\frac{\ell}{L}\right)^{1/3}$

where $\ell \sim 50$ μm is the inner scale and $L \sim 600$ μm is appropriate such that $v_{turb} = v^0_{turb} (\ell/L)^{1/3}$.

Relative drift velocity

The relative drift velocity between the electrons and ions results in a different relative height between the two peaks. If there is no relative drift, then the peaks are equal in amplitude as shown in Figure 5.2g. The drift velocity is a result of Landau damping.

Electron density

The Thomson scattered ion features are relatively insensitive to changes in electron density. This can be seen directly from the Bohm-Gross relation and is shown in Figure 5.2h.

Instrument Function

An instrument function, encompassing broadening due to optics within the diagnostic, is included within the analysis. The width of the instrument function can be fitted correctly using the unscattered stray light which gives a Gaussian instrument function with width 0.025 nm is used appropriate.

5.2.2 Thomson Scattered Electron Features

The Thomson scattered electron features have two peaks which are much weaker and broader than the ion features. The same code can be used to fit the electron features.

Similarly to the scattered ion features, by fitting the unscattered light, an instrument function is included with a Gaussian of width 5.4 nm. The spectral sensitivity of the diagnostic must also be removed from the data before analysis such that the spectrum is flat-fielded.

A fully fitted spectrum is shown in Figure 5.3a.

Electron Density

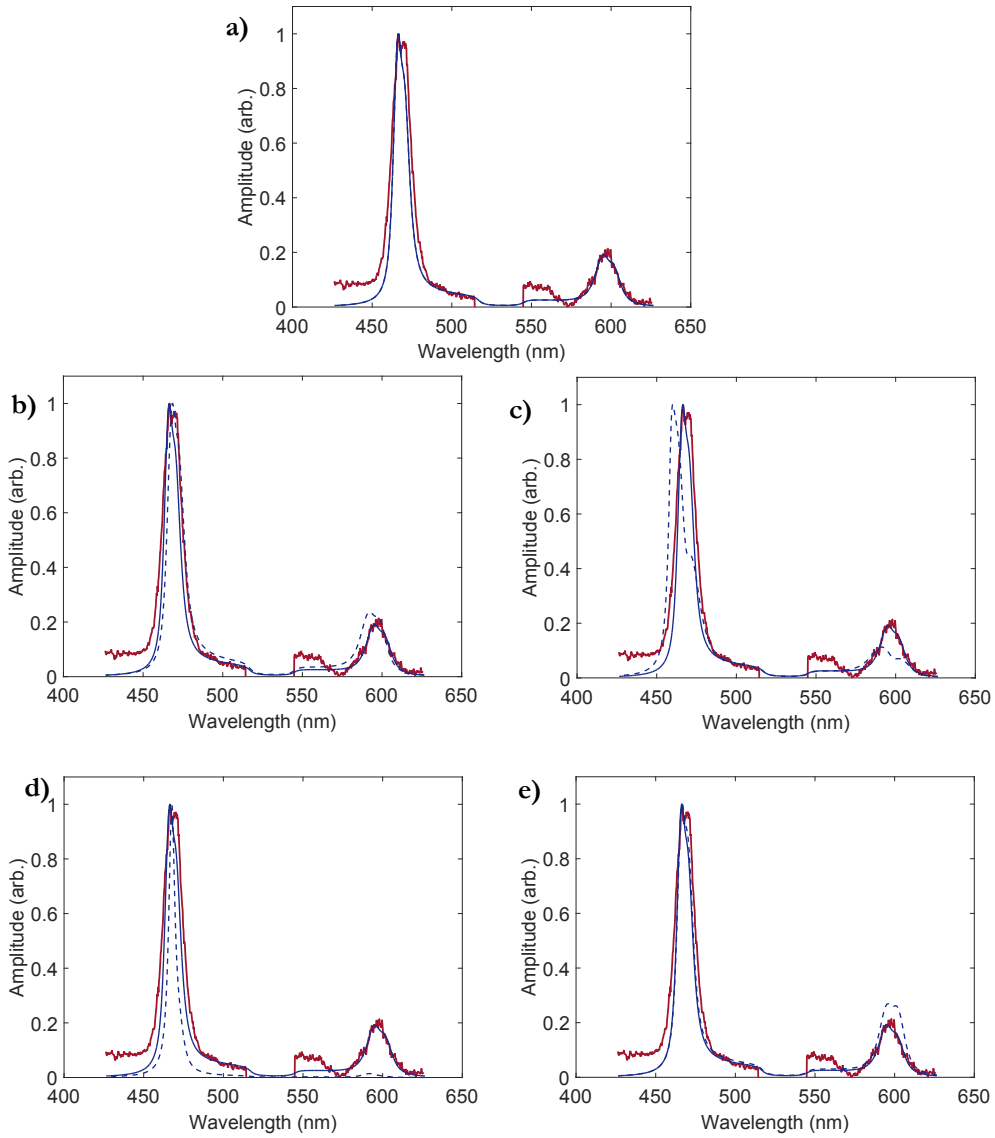

Figure 5.3: Fitted electron features: a) Thomson scattering data (red solid line) is compared with a predicted spectra (blue solid line). The predicted spectra has an electron density of 4.75×10^{19} cm^{-3} with a Gaussian range of electron densities with width 10^{19} cm^{-3}, an electron temperature of 400 eV and a spatial gradient length scale of 100 μm. b)-e) are the same as a) with an additional fit (blue dashed line) that has: b) an electron density of 4.25×10^{19} cm^{-3}, c) a Gaussian range of electron densities with width 2×10^{19} cm^{-3}, d) an electron and ion temperature of 300 eV and e) a spatial gradient scale length of 500 μm.

The separation of the two peaks in the spectrum of the electron features is governed by the electron density. Small changes in electron density can drastically change the separation of the two peaks, allowing a precise fit to be made as shown in Figure 5.3b.

In this experiment, it is not expected that the plasma will have a uniform electron density. In fact, it is more likely for multiple electron densities to be present within the interaction region due to the turbulent nature of the plasma. To include this within the Thomson scattering analysis, a range of electron densities around some central mean value have been included. The additional electron densities have been weighted according to a Gaussian, centred on the mean electron density. The width of this Gaussian then gives an indication of the range of electron densities within the plasma. The thickness of the peaks is sensitive to the width of the Gaussian, as shown in Figure 5.3c.

Electron Temperature

Changes in electron temperature alters the width of the peaks, as shown in Figure 5.3d, similarly to adding a range of electron densities. For these spectra, the electron temperature is found first by fitting the ion features and then any additional broadening can be accounted for solely by a range of electron densities.

Spatial gradients

Inhomogeneities within the plasma can cause spatial and temporal gradients to arise. By inclusion of spatial gradients within the predicted Thomson scattering spectra, the electron and ion susceptibilities are changed accordingly.

Following the method in [135], the effects of gradients within a Maxwellian plasma on the electron susceptibility can be written as

$$\chi_e(\mathbf{k},\omega) = \chi_e^{eq} - \frac{i}{\Lambda}\frac{\partial}{\partial k}\chi_e^{eq} + \frac{i}{\tau}\frac{\partial}{\partial \omega}\chi_e^{eq}, \tag{5.2}$$

where χ_e^{eq} is given by Equation 2.115 and Λ and τ are the spatial and temporal gradient scales along the scattering wavevector respectively. For a Maxwellian

plasma, exact expressions can be found and so Equation 5.2 can be written as

$$\chi_e(\mathbf{k},\omega) = \alpha^2 \left\{ \left[R(x) + \frac{1}{kv_{Te}} \left(\frac{-\omega}{\Lambda k} + \frac{1}{\tau} \right) \frac{d}{dx} I(x) \right] + i \left[I(x) - \frac{1}{kv_{Te}} \left(\frac{-\omega}{\Lambda k} + \frac{1}{\tau} \right) \frac{d}{dx} R(x) \right] \right\}, \tag{5.3}$$

where $\frac{d}{dx}I(x) = \sqrt{\pi} x e^{-x^2}$ and $\frac{d}{dx}R(x) = -\left[\frac{d}{dx}I(x)\mathrm{erfi}(x) + 2x\right]$ and $\mathrm{erfi}(x) = -i\mathrm{erf}(ix) = -i\frac{2}{\sqrt{\pi}}\int_0^{ix} e^{-p^2} dp$ is the imaginary error function.

The ion susceptibility is unchanged by spatial gradients and the effects of gradients should only be included in ϵ, i.e., in the denominators of Equation 2.111. In these sorts of plasmas, it is likely that only spatial gradients will play a role and so the spatial gradients only are included within the Thomson scattering code.

This method of including spatial gradients within the code fitting is different from that of the previous section where a range of densities was included as a Gaussian. The Gaussian range in densities indicates the different electron densities present within the Thomson scattering volume. Consequently, a situation could be imagined where there is no gradient in electron density across the entire plasma but there is still a range of electron densities within the Thomson scattering volume which would increase the width of the electron features. Conversely, a spatial gradient could still be measured within the Thomson scattering volume even if there was only one electron density within the measured volume. Spatial gradients and a Gaussian range in electron densities therefore lead to different effects on the Thomson scattering spectrum.

A relativistic correction to the phase velocity of the electron-plasma wave also changes the relative heights of the electron features. It is therefore imperative that relativistic effects [136] are accounted for first, as is done here, before the addition of inhomogeneities within the plasma.

The relative heights of the two peaks can be very sensitive to these spatial gra-

dients as shown in Figure 5.3e.

5.3 Thomson Scattering Data

The Thomson scattering data was either temporally or spatially resolved, depending on shot day (see Table 5.1). The temporally resolved data used a streak camera that had a resolution of 50 ps and so the data has been fitted every 100 ps. The spatially resolved data had a 5 μm resolution on the CCD and so is fitted every 10 μm.

The data can be divided into those shots with no Chlorine doped into the foils and those shots with Chlorine doped foils. The non-Chlorinated data is described first, followed by the Chlorinated data.

5.3.1 Non-Chlorinated Foils

The data from the non-Chlorinated target foils has a mixture of temporally and spatially resolved Thomson scattering data.

When the data was spatially resolved, smearing from the pulse duration of the Thomson scattering probe beam prevents a measurement of the turbulent velocity. Consequently, no turbulent velocity measurements are shown for the non-Chlorinated data.

Electron temperature and flow velocity can be determined for the non-Chlorinated shots. The electron temperature and flow velocity are plotted relative to where the measurement was taken in terms of space and time within the experiment as shown in Figure 5.4. For this Figure, t=0 ns is taken to be when the collision is predicted to occur from FLASH which is 21 ns after the start of the laser-drive, and 0 mm is the centre of the interaction region.

Figure 5.4a shows that, for each shot, the electron temperature remains relatively constant, to within $\sim$ 30 eV, across the region probed by the Thomson scattering

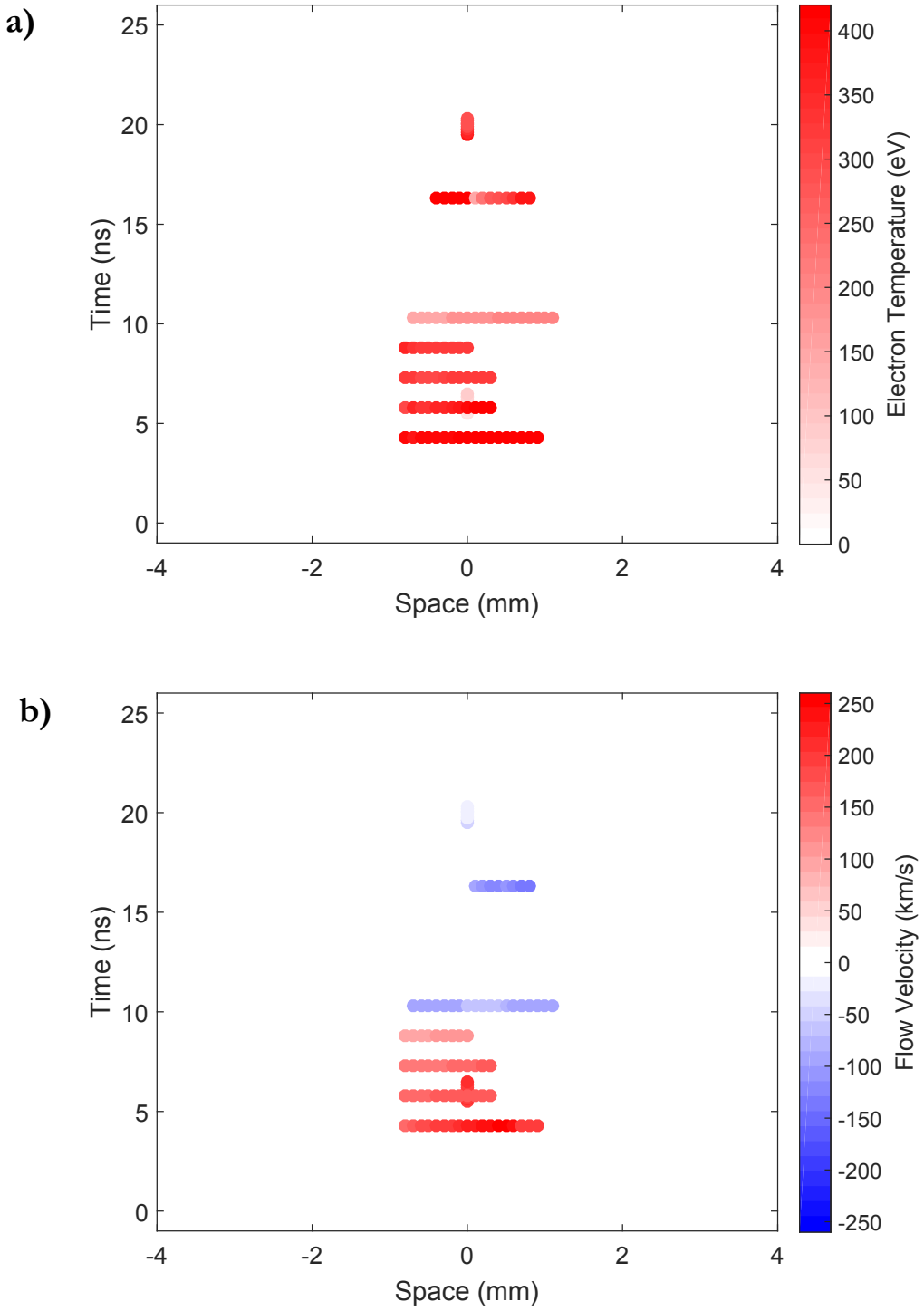

Figure 5.4: Spatial and temporal variation of a) electron temperature and b) flow velocity for non-Chlorinated shots. Here 0 ns is set to the collision time of the two jets. The spatial axis corresponds to distance along the laser axis where 0 mm is the centre of the interaction region - the point in the middle of the two grids.

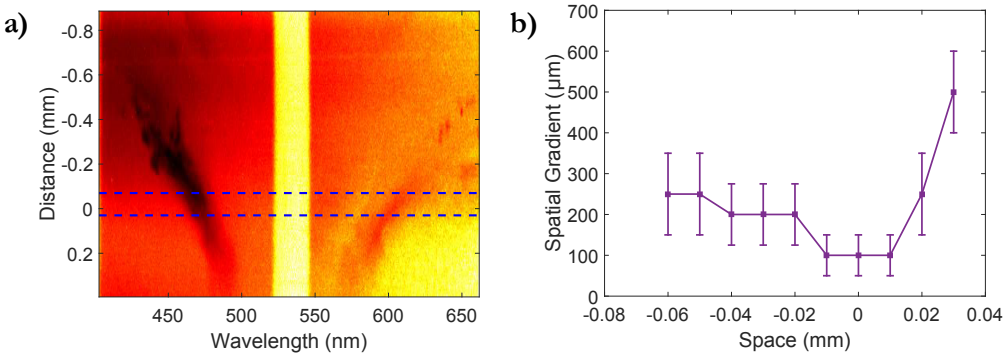

Figure 5.5: Inhomogeneities in electron features: a) EPW image allows spectrally dispersed features (horizontal axis) to be fitted at different points in space (vertical axis). The blue dashed lines indicates the extent of which a spatial gradient scale can be determined within the plasma. Outside of these blue dashed lines, one of the electron features is too weak and so it is not possible to accurately attain a measurement of the spatial gradient length scale. b) Spatial graident length scale, as determined by fitting the electron features within the 100 μm region in a), is plotted against space.

diagnostic, $\sim$ 1.6 mm. This indicates that the electron temperature is approximately uniform across the plasma region probed by the Thomson scattering beam. Similarly for those shots that are temporally resolved, the electron temperature does not appear to vary more than 30 eV during the 1 ns pulse duration. This means that the average electron temperature can be taken as a representative value for each shot.

Figure 5.4b shows that the flow velocity remains relatively constant, to within $\sim$ 40 km/s, across the region probed by the Thomson scattering diagnostic. This indicates that the flow velocity can vary by up to 50% across the plasma region probed by the Thomson scattering beam. However, the velocity does not change by a large amount within the ns of the temporally resolved shots which are measured in the centre of the interaction region. This means that, like the electron temperature, an average flow velocity can be used for each shot when making further comparisons within the central region of the plasma.

Figure 5.5 shows how the length scale of spatial gradients due to inhomogeneities within the plasma changes against distance along the Thomson scattering probe beam. This length scale is on the order of a few hundred μm and gives an indication

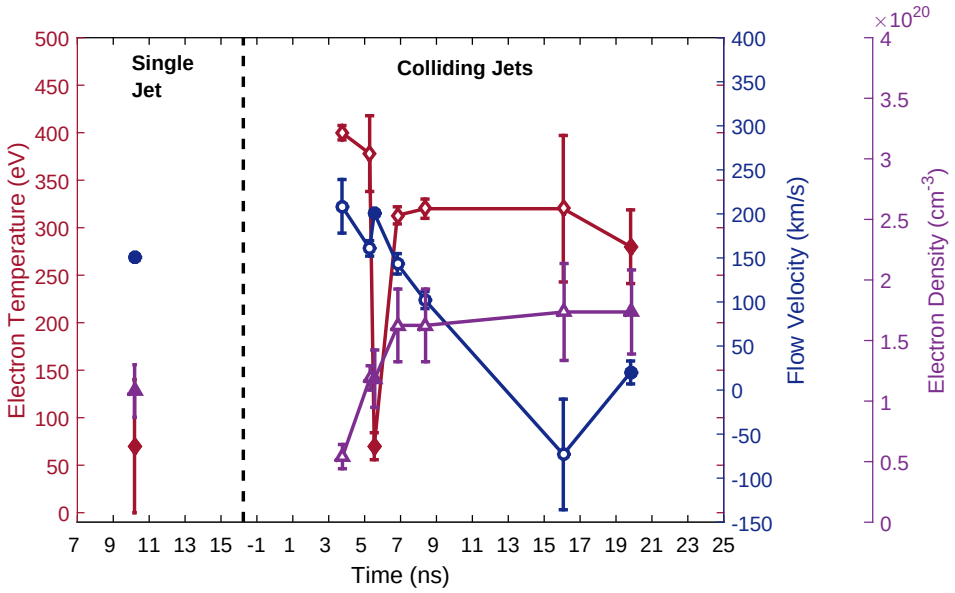

Figure 5.6: Non-chlorinated plasma quantities: The electron temperature (red diamonds), bulk flow velocity (blue circles) and electron density (purple triangles) are plotted against time. All shots included here have CH foils, a 10 ns laser-drive and grids of type AB−2. A time of 0 ns indicates the collision time of the two flows and takes place 21 ns after the laser drive. Open markers indicate shots that have spatially resolved Thomson scattering and so the electron density is calculated from fitting the electron features; those with closed markers indicate temporally resolved Thomson scattering and so the electron density is found by an absolute photometric calibration. For all of these shots, a Thomson scattering pulse length of 1 ns was used and the Thomson scattering beam was pointed at the mid-point between the two foils. The data point shown is from the average data for that shot, displayed at the centre of the Thomson scattering pulse (i.e 0.5 ns after the start of the probe beam). A shot was taken with only one half of the laser-drive such that only one plasma flow was generated. This shot is therefore indicative of the plasma conditions before the collision of the two jets and is labeled as 'Single Jet'. Note the individual time axes for the single and collided jets.

as to the scale at which changes in electron density occur. Unfortunately, the spatial gradient was only retrievable from a subsection of one shot, making further conclusions difficult. This is because once the two plasmas have collided, the resultant Bresmsstrahlung from the hot plasma washes out the two electron peaks and so the relative heights of the two peaks cannot be determined.

Electron temperature, flow velocity and electron density

The electron temperature, flow velocity and electron density of the non-Chlorinated shots are plotted against time as shown in Figure 5.6. The closed markers indicate temporally resolved Thomson scattering, whilst open markers indicate spatially resolved Thomson scattering.

A shot with a single jet (i.e., only one foil was irradiated by the laser-drive) is included for use as pre-collision parameters. The temporally resolved shot at ≈ 6 ns is very similar to the single jet shot in terms of both electron temperature and flow velocity. This suggests that the Thomson scattering data for this shot is before the collision, despite the probe beam delay time. This difference in timing could be due to less energy in the drive beams compared with the other shots. This shot characterizes the temporal uncertainty in the results from shot-to-shot variation.

The single jet shot shows that electron density, of one jet, is $\approx 10^{20}$ cm^{-3}. This electron density is in agreement with the colliding jet shots that take place immediately prior to collision. As the collision progresses, the electron density rises from $\approx 0.5\text{-}1 \times 10^{20}$ cm^{-3} to just under $\approx 2 \times 10^{20}$ cm^{-3}. This increase in electron density is partly due to the combination of having the two plasma flows converge. An additional increase in electron density is likely because of the continuous influx of material from the irradiated plasma which continues to flow into the interaction region, although this is offset by the lateral expansion of the plasma.

The electron temperature increases from 70 eV before the collision to ≈ 400 eV immediately after the collision. The collided plasma then cools to ≈ 300 eV around 8 ns after the initial collision. The plasma then maintains an electron temperature of ≈ 300 eV for tens of ns afterwards.

The Thomson scattering probe beam itself has the potential to heat the plasma. An estimate of this heating is given by [66],

$$\frac{\Delta T_e}{T_e} \leq 5.32 \times 10^{-7} \left(\frac{Z n_e}{T_e^{3/2}} \right) \lambda^3 \left(1 - \mathrm{e}^{-\hbar\omega / e T_e} \right) I_0 \tau \quad , \tag{5.4}$$

where T_e is the electron temperature (in eV), n_e is the electron density (in cm^{-3}, Z is the mean ion charge, λ is the laser wavelength (in cm), ω is the laser frequency, I_0 is the laser intensity (in W/cm^2) and τ is the laser pulse duration (in s). This equation can be regarded as an upper bound since it does not take into account the rapid transport of heat away from the laser focus by both convection and conduction - the high electron thermal conductivity is important for making the temperature uniform across the interaction region. Taking $n_e \approx 10^{20}$ cm^{-3}, $T_e \approx 400$ eV for a 30 J, 1 ns probe beam focussed onto a 50 μm^2 region gives $\Delta T_e/T_e \leq 20\%$.

The velocity of the two plasma flows is ≈ 150 km/s before the collision. Once the two plasma flows have collided, the velocity of the two flows sharply decreases. The plasma itself is free to have some bulk motion within the observed 50 μm region and so bulk velocities ≈ 50 km/s are measured tens of ns after the collision has occurred as the parallel flow motion is transferred into all directions.

Energy Transfer

To examine how the energy within the counter-streaming jets is transferred as the collision progresses, the thermal and bulk flow pressures are calculated according to $P_{therm} = (n_e + n_i)\, k_B T_e$ and $P_{bulk} = \frac{1}{2} n_i v_f^2$, where v_f is the flow speed found from the Thomson scattering data. From Figure 5.7, it is seen that the collision between the two jets is marked by a rapid increase in thermal pressure and a sharp decrease in bulk flow pressure. As the two flows collide, the flow pressure of the jets along the foil axis is converted into transverse motions and heat. A few ns after the collision, this bulk pressure becomes very low and is likely comparable to the transverse flow (or turbulent flow) pressure as the plasma isotropizes.

The horizontal, black, dashed line on Figure 5.7 indicates the total energy density before the collision for two single jets. The total energy density is calculated by doubling the bulk flow and thermal pressures for the single jet. Before the collision, the expected turbulent and magnetic pressures are negligible and so this single jet

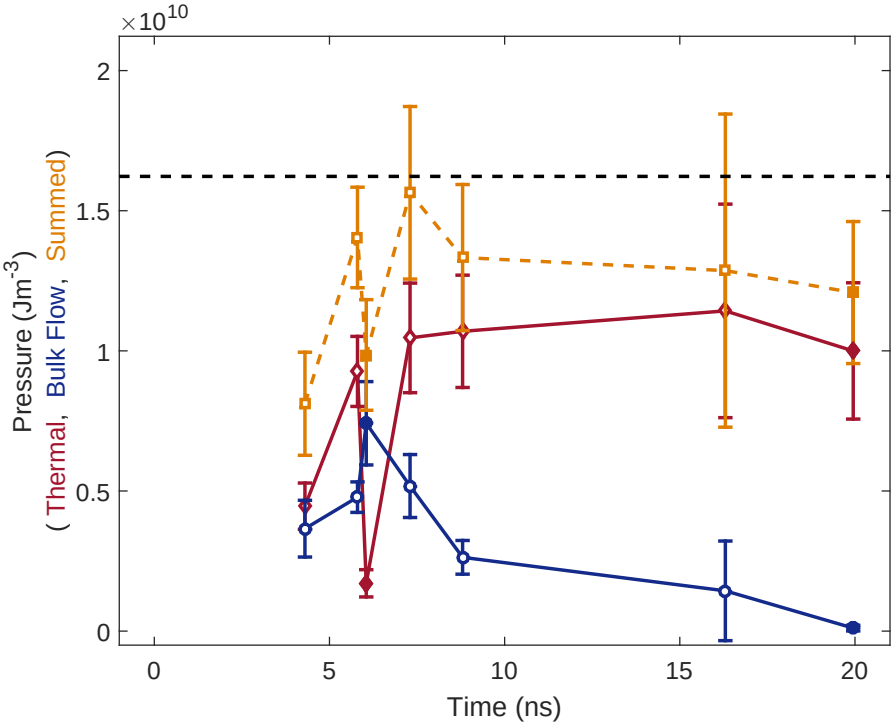

Figure 5.7: Non-chlorinated energy densities: The energy density contributions from thermal pressure (red diamonds), bulk flow pressure (blue circles) and summation of the two (dashed yellow squares) are plotted against time for different shots. All shots included here have CH foils, a 10 ns laser-drive and grids of type AB−2. A time of 0 ns indicates the collision time of the two flows and takes place 21 ns after the laser drive. Open markers indicate shots that have spatially resolved Thomson scattering and those with close markers indicate temporally resolved Thomson scattering. For all of these shots, a Thomson scattering pulse length of 1 ns was used and the Thomson scattering beam was pointed at the mid-point between the two foils. The data point shown is from the average data for that shot, displayed at the centre of the Thomson scattering pulse (i.e 0.5 ns after the start of the probe beam). The total expected energy density from before the collision (i.e., the summed thermal pressure and bulk flow pressure for two single jets) is shown with the black dashed line.

shot should provide the total available energy for the entire interaction. Immediately after the collision, the summed thermal and bulk pressures are approximately equivalent to the black dashed line. After the collision, there is a deficit which is likely accounted for by the lateral expansion velocity, which is not measured, and an increase in turbulent and magnetic pressures expected for a turbulent plasma which

is amplifying magnetic fields.

Assuming that this difference in the total energy density compared with the energy density after the collision is due to magnetic and turbulent pressures, an approximate magnetic field value can be determined. Assuming that the turbulent velocity is similar to the late time velocity, $\sim$ 50–70 km/s, then implies a maximum magnetic field of 500 kG. A magnetic field of a few hundred kG is consistent with those results from Faraday rotation and proton radiography as described in Ref. [18].

5.3.2 Collision Mechanism for interacting jets

Using the non-Chlorinated measured values for the electron temperature, flow velocities, electron density and a magnetic field of 100 kG as taken from Ref. [18], the plasma state can be fully characterized to give the parameters in Table 5.2. The Debye length for the collided jets is $\sim$ 15 nm which is greater than the ion separation length $n_i^{-1/3} \approx 2$ nm and so the plasma can be described classically. The Coulomb logarithm is ~ 7. If a Maxwellian distribution is assumed, the ion-ion mean free path is $\lambda_{ii} \approx 1$ μm which is larger than the Debye length but smaller than any relevant hydrodynamic length scales, implying a collisional plasma.

The interaction region in the centre is formed from two interacting plasma jets which can each be approximated by a Maxwellian with peaks centred at $U \sim \pm 200$ km/s. This initial distribution is then subject to a variety of processes due to the collisions between counter-propagating particles.

To investigate the effect of the interaction of the two beams, its important to note that $\frac{1}{2} m_i U^2 > k_B T_e$ and so the ion motions are energetically dominant over electron motions. This is the same as saying that the jet motion has a sonic Mach number > 1 before the collision. The collisional relaxation times can then be calculated for a test ion beam moving with velocity $2U$ into a stationary Maxwellian plasma. This test beam is fast relative to the ions in the rest frame, but slow compared to the

electrons,

$$V_{ti} = 100 \text{ km/s} < U < V_{te} = 10,000 \text{ km/s} \quad , \tag{5.5}$$

where V_{ti} and V_{te} are the ion and electron thermal speeds. Estimating the beam relaxation times accordingly, it is found that the predominant slowing and perpendicular spreading of the test beam distribution is due to the ions. The associated length scales over which particles in the jet experience these relaxation processes are $\lambda_s \sim .49$ mm and $\lambda_t \sim 4.5$ mm for the slowing and perpendicular spreading of the test ion beam.

The characteristic scale for the Weibel instability in the jet is [137, 138] $\ell_w \sim c/\omega_{pi} \sim 30$ μm. The length scale for the development of electrostatic instabilities is ~ 2 μm [137] which is smaller than the length scale associated with collisions. Further, as the interaction between the jets develop, regions of higher density and lower velocity might be expected which would then favour collisions as the dominant process. It is therefore reasonable to describe the plasma interaction as approximately Maxwellian even if the processes governing the initial jet interaction are not simply collisional. Under this assumption, the temperature equilibration time between ions and electrons is then calculated to be $\tau_{ie} \sim 9$ ns, consistent with the assumption of a plasma in thermal equilibrium.

Various transport quantities can then be calculated. The magnetization of the ions and electrons, with Larmor radii Ω_i and Ω_e, is then found to be,

$$\Omega_i \tau_{ii} \approx 5 \times 10^{-3} \ll 1 \quad , \Omega_e \tau_{ie} \approx 1.3 \geq 1 \quad , \tag{5.6}$$

and so the electrons are magnetized whilst the ions are unmagnetized. The magnetized state of the electrons has various consequences, anisotropization of the thermal and electrical conductivities and the appearance of various terms in the

generalised Ohm's law associated with a finite electron Larmour radius. However since ion flows dominate bulk motion, it might be inferred that the plasma dynamics would be relatively unaffected by this.

It can be concluded that conventional MHD provides a reasonable description of the plasma dynamics, since $T_e \sim T_i$ the electrical conductivity is essentially determined by the electrons and the viscosity by the ions [139]. This gives diffusivities,

$$\nu \approx 400 \text{ cm}^2\text{s}^{-1} \quad , \mu \approx 1400 \text{ cm}^2\text{s}^{-1} \quad . \tag{5.7}$$

It can be concluded that the interacting plasmas can be reasonably described by conventional MHD.

For this MHD type plasma, the characteristic fluid and magnetic Reynolds numbers can be estimated as Re$\sim$ 1500 and Rm$\sim$ 400, thus above the expected critical magnetic Reynolds number for turbulent dynamo. Magnetic field measurements from the Faraday rotation and proton radiography diagnostics indicate magnetic fields [18] $\approx$ 100 kG which cannot be simply explained by the compression of the field due to shock formation (which would only account for at most a factor of two), nor by further generation by Biermann battery since the temperature gradients are not strong enough. The expected timescale for saturation of the field is expected to be on the outer-scale turnover time, $\sim$ 6 ns, which is comparable to the initial flow collision and the magnetic field measurements.

5.3.3 Chlorinated Foils

A similar analysis can be completed for those shots that have a Chlorine dopant. There are four different types of Chlorine shots: 1% and 6% Chlorine doping within the CH foils and both 5 and 10 ns drive-laser pulse length. Consequently there are often not many shots of the same initial condition which makes comparisons difficult.

For all of these shots, the Thomson scattering data was temporally resolved. The

Table 5.2: Different plasma parameters associated with the collision of the two jets. The magnetic field and turbulent velocity for the non-Chlorinated shots are assumed to be similar to the non-Chlorinated shots. Within the table $W = 5.2 \times 10^{-9} AV^2$ [137] and $\ln(\Lambda)$ is the Coulomb logarithm.

Quantity	Expression	Value
Ion Mass M	–	6.5 m_p
Ion Charge Z	–	3.5
Electron Density n_e (cm^{-3})	–	10^{20}
Electron and Ion Temperature T (eV)	–	300
Flow Velocity V (m/s)	–	200×10^3
Magnetic Field, B (T)	–	0.1
Turbulent Velocity V_{turb} (m/s)	–	100×10^3
Length Scale (cm)	–	0.06
Plasma Frequency ω_{pe} (rad/s)	$\sqrt{10^6 n_e e^2/m_e \epsilon_0}$	5.6×10^{14}
Ion Plasma Frequency ω_{pi} (rad/s)	$\sqrt{10^6 n_i Z^2 e^2/m_i \epsilon_0}$	9.7×10^{12}
Electron skin depth (m)	c/ω_{pe}	5.3×10^{-7}
Ion skin depth (m)	c/ω_{pi}	3.1×10^{-5}
Electron thermal velocity (m/s)	$\sqrt{eT_e/m_e}$	1.0×10^7
Ion thermal velocity (m/s)	$\sqrt{ZeT_i/m_i}$	9.4×10^4
Debye length (m)	$\sqrt{\epsilon_0 eT_e/10^6 n_e e^2}$	1.5×10^{-8}
Sound speed c_s (m/s)	$\sqrt{eZT_e/M + 3T_i/M}$	1.7×10^5
Sound Mach number	V/c_s	1.2
Plasma beta	$2 \times 10^6 \mu_0 n_e e T_e/B^2$	1.2×10^6
$\tau_s^{i\|e}$ (s)	Table 2.1	2.5×10^{-9}
$\tau_t^{i\|e}$ (s)	Table 2.1	2.2×10^{-9}
$\tau_s^{i\|i}$ (s)	Table 2.1	5.4×10^{-11}
$\tau_t^{i\|i}$ (s)	Table 2.1	5.4×10^{-11}
$\tau_{ee}(s)$	$3.44 \times 10^5 T_e^{1.5}/Z n_e \ln(\Lambda)$	7.6×10^{-13}
$\tau_{ii}(s)$	$2.09 \times 10^7 A^{0.5} T_i^{1.5}/Z^4 n_i \ln(\Lambda)$	9.7×10^{-12}
$\tau_{ie}(s)$	$6.27 \times 10^8 A T_e^{1.5}/Z n_e \ln(\Lambda)$	9.1×10^{-9}
Electrostatic length scale, ℓ_{ES}, (m)	$3 \times 10^{-4} V\sqrt{A} W/Z\sqrt{n_e T_e}$	2.0×10^{-6}
Electron cyclotron frequency, ω_{ce}, (rad/s)	eB/m_e	1.8×10^{12}
Ion cyclotron frequency, ω_{ci}, (rad/s)	ZeB/M	5.2×10^8
Electron Larmor radius, r_{ge}, (m)	$m_e v_{te}/(eB)$	5.8×10^{-6}
Ion Larmor radius, r_{gi}, (m)	$MV/(ZeB)$	1.8×10^{-4}
Alfven Velocity V_A (m/s),	$B/\sqrt{\mu 0 (M n_i + m_e n_e) 10^6}$	1.6×10^4
Alfven Mach Number	V/V_A	12
Electron magnetisation	$\omega_{ce}\tau_{ie}$	1.6×10^4
Ion magnetisation	$\omega_{ci}\tau_{ii}$	5.0×10^{-3}
Diffusivity ν (cm^2/s)	$1.92 \times 10^{19} T_i^{2.5}/A^{0.5} Z^4 n_i \ln(\Lambda)$	410
Reynolds number Re	$V_{turb} L/\nu$	1500
Resistivity μ (cm^2/s)	$1.4 \times 10^3 Z \ln(\Lambda)/T_e^{1.5}$	1.4×10^3
Magnetic Reynolds number Rm	$V_{turb} L/\mu$	400
Prandtl number, Pm	Re/Rm	0.28

Faraday rotation diagnostic was in place and so the electron features are not spectrally resolved. Instead, the electron density is found from an absolute photometric calibration of the system, as described in Chapter 4.

Whilst none of the data was spatially resolved, there is some spatial variation in exactly where the Thomson scattering data was taken. The grids used for this shot day are slightly different to the non-Chlorinated foils in that they have larger wires (300 μm compared with 100 μm). The smaller hole size means that the two jets are more asymmetric and so the two jets collide slightly off-centre at $\approx$ 400 μm towards Grid B (see Figure 5.1c). Correspondingly, the Thomson scattering probe beam was pointed 400 μm towards Grid B. For one of the shots with 6% Chlorine and a 5 ns drive, the two grids were swapped over and so the Thomson scattering measurement made here is equivalent to 400 μm towards Grid A and so is further away from the interaction region.

By fitting the ion features of the Thomson scattering spectrum, the electron temperature and flow velocity can be plotted against space and time to give Figure 5.8.

Figure 5.8 shows that there is minimal temporal variation in the electron temperature and flow velocity over the 1 or 3 ns Thomson scattering probe beam. This means that an average electron temperature and flow velocity can be used for making comparisons between the Chlorinated shots.

The addition of Chlorine acts to slow down the resultant plasma flow due to the increase in target density and radiative cooling. The foil density before the laser-drive for those shots with no Chlorine, 1% Chlorine and 6% Chlorine are 1.07 gcm^{-3}, 1.29 gcm^{-3} and 1.55 gcm^{-3}. This indicates that there is a large initial increase in electron density when Chlorine is doped into the target foils. The increased power of the 5 ns laser drive increases the flow velocity of the two plasma flows compared with the 10 ns laser drive, advancing the collision time.

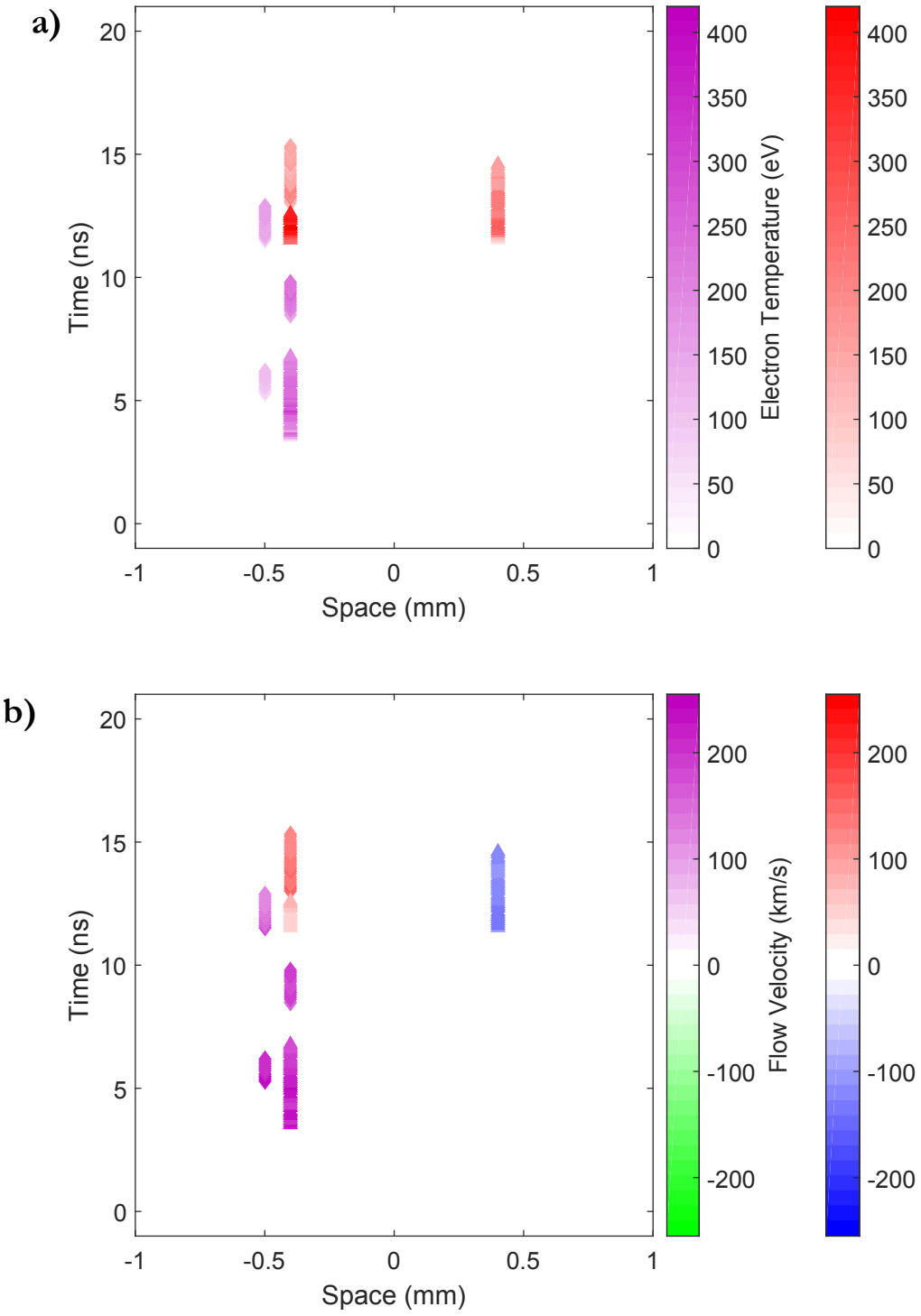

Figure 5.8: Spatial and temporal variation of electron temperature and flow velocity for Chlorinated shots: Shots with 1% Chlorine target dopant (purple-green); 6% Chlorine target dopant (red-blue); a 10 ns laser-drive (diamonds) and a 5 ns laser-drive (triangles) are plotted against space and time. Here 0 ns is set to the collision time of the two jets when there is no Chlorine in the targets and a 10 ns laser-drive. The spatial axis corresponds to distance along the laser axis where 0 mm is the centre of the interaction region - the point in the middle of the two grids. All of the data is taken at either 0.4 or −0.4 mm, those data points at −0.5 mm are artificially moved to more clearly present the data.

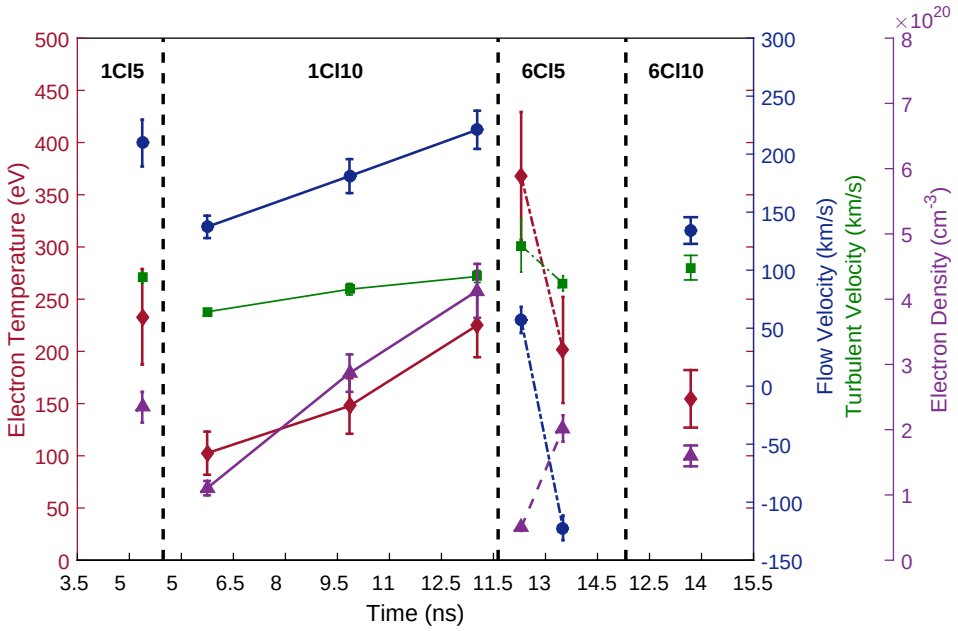

Figure 5.9: Chlorinated plasma quantities: The electron temperature (red diamonds), bulk flow velocity (blue circles), turbulent flow velocity (green squares) and electron density (purple triangles) are plotted against time for different shots with different initial conditions. Here a time of 0 ns indicates the collision time of the two flows for CH foils with a 10 ns laser drive and AB−2 grids. For the shots shown in this plot, all shots have temporally resolved Thomson scattering and grids of type AB−1. The Thomson scattering pulse length was either 1 or 3 ns, depending upon the shot and is pointed 0.4 mm away from the mid-point of the two foils, along the foil axis such that it is measuring within the interaction region. Each data point is an average of all of the acquired data for that shot and is positioned at the centre of the Thomson scattering pulse (i.e., 0.5 ns or 1.5 ns after the start of the probe beam). Four different initial conditions are shown on this plot and are indicated by the dashed black lines. Particular attention should be drawn to those shots with 6% Chlorine and a 5 ns laser-drive ('6Cl5') since for the later shot, the two grids were swapped around. In effect, this means that the Thomson scattering probe beam was measuring 0.4 mm to the other side of the foil axis centre and so is measuring the plasma properties outside of the interaction region. Note that each region has its own, individual time axis.

The electron temperature, bulk flow velocity, outer scale turbulent flow velocity and electron density are plotted for these different target conditions in Figure 5.9. The horizontal time axes refer to the FLASH predicted collision time of the non-Chlorinated, 10 ns laser drive from the previous section. This allows for a direct temporal comparison between the Chlorinated and non-Chlorinated shots.

1% **Chlorine dopant,** 5 **ns laser-drive**

The plasma conditions of '1Cl5', shown in the leftmost portion of Figure 5.9, imply that for those shots with 1% Chlorine dopant, 5 ns laser-drive, the two jets have just collided. This type of shot is expected to have a larger flow velocity than the non-Chlorinated shots due to the increased intensity of the laser-drive. The flow velocity for '1Cl5' is ~ 200 km/s which is faster than the non-Chlorinated flow velocity of ~ 150 km/s. The electron temperature is smaller for the '1Cl5' condition, 230 eV, compared with 400 eV for the non-Chlorinated case. The turbulent velocity is smaller than the measured flow velocity, implying that the motions of the plasma are not yet completely isotropic. This might suggest that the two '1Cl5' jets have just collided and a few more ns is required to allow the turbulent region to develop and for the field to fully saturate.

1% **Chlorine dopant,** 10 **ns laser-drive**

Those shots with 1% Chlorine and a 10 ns laser-drive are expected to behave similarly to the non-Chlorinated shots. There are a few differences, such as the grid spacings. It is expected that since the grid used for the non-Chlorinated shots have wider hole spacings, they will allow more material through and so produce a higher density interaction. The second panel in Figure 5.9 shows that the electron density at the collision is $\approx 1 \times 10^{20}$ cm^{-3} and then rapidly increases to 3–4 $\times 10^{20}$ cm^{-3} within 5 ns, an unexpectedly much larger density than that of the non-Chlorinated foils.

The flow velocity of the '1Cl10' shots increases with time from 120-220 km/s over 6 ns. This trend is unexpected and so could be a result of shot-to-shot variation.

The electron temperature at collision time is ≈ 100 eV, similar to that of the non-Chlorinated case, ≈ 70 eV. After collision, there is not the same rapid increase in electron temperature to $\approx 300 - 400$ eV that was seen with no Chlorine, instead the electron temperature rises steadily to ≈ 200 eV similar in value to the '1Cl5' ns

laser-drive shot. This could suggest that the Chlorine is reducing the temperature of the plasma.

The turbulent velocity increases from ≈ 50–100 km/s over 6 ns. The turnover time for this plasma can be estimated as $L/v_{turb} \approx 0.6$ mm/100 km/s ≈ 6 ns.

6% **Chlorine dopant,** 5 **ns laser-drive**

The two shots with 6% Chlorine and a 5 ns laser drive (shown in the third portion of Figure 5.9, labeled '6Cl5') cannot be directly compared. The second shot (the shot later in time) has the two grids swapped around and so is equivalent to the Thomson scattering region being 0.4 mm on the other side of the interaction i.e., far away from the main collision point.

Within the turbulent interaction region, the electron temperature is large ≈ 350 eV, similar to the non-Chlorinated case, and the flow velocity is comparable to the turbulent velocity ≈ 50 km/s, suggesting that the plasma is broadly isotropic since there are movements of the plasma in any direction. This large electron temperature implies that either this shot has captured a particularly hot region of plasma, or Chlorine does not have such a large effect on electron temperature as was indicated by the previous two data sets.

The turnover time for the plasma is ≈ 6 ns and so there has been sufficient time for the magnetic field to saturate by the time this data is taken. Outside of the interaction region, the plasma is relatively cool ≈ 150 eV, flowing at ≈ 100 km/s towards the interaction region

It appears from these two shots that the electron density is much larger outside the interaction region $\approx 2 \times 10^{20}$ cm^{-3} compared with inside the interaction region $\approx 0.5 \times 10^{20}$ cm^{-3}. This is unexpected since there is less material outside of the interaction region.

6% **Chlorine dopant,** 10 **ns laser-drive**

The 6% Chlorine and a 10 ns laser drive (and shown in the right-most portion

of Figure 5.9, labeled '6Cl10') is the slowest target because of the large percentage of Chlorine and has a flow velocity of $\approx$ 130 km/s. The cool electron temperature, as compared with the non-Chlorinated shots, indicates that the Chlorine has cooled the plasma. The reduced flow velocity implies that there is less energy within the plasma to transfer into heat, which is a possible explanation for the lower electron temperature.

The small electron temperature $\approx$ 150 eV, average flow velocity $\approx$ 130 km/s and electron density $\approx 1.5 \times 10^{20}$ cm^{-3} suggests that the predicted collision has taken place.

Accounting for experimental differences between non-Chlorinated and Chlorinated foils

The majority of Chlorinated shots have an unknown collision time and so the relative timing of different data shots is hard to establish. However, it is clear that those shots doped with more Chlorine have slower plasma flows than those without.

Those shots with no Chlorine are mostly taken from spatially resolved Thomson scattering compared with the Chlorinated shots that all have time resolved Thomson scattering. Whilst there should be no difference in the parameters attained through spatially resolved compared with temporally resolved Thomson scattering, the measurements are not identical and so may not capture the same things. The spatially resolved Thomson scattering is averaged over the 0.6 ns probe beam whereas the temporally resolved case looks at the scattering from a 50 μm^2 volume and can resolve up to 0.05 ns. Differences can arise depending upon the time scales and spatial extents of the phenomena being observed. For instance, for fast processes that can be captured by the temporally resolved Thomson scattering may not be fully captured by the spatially resolved Thomson scattering. However, it can be estimated that the turnover time for this plasma is $\approx$ 6 ns and so the two diagnostics can likely be

compared fairly to one another. From Figure 5.8, it is clear that the temporal and spatial variation of the plasma within a 0.1 ns time scale and 0.1 mm spatial scale is minimal.

The relative electron densities of the different shots shows that those shots with Chlorine have a much larger electron density than those without. This disparity in electron density could be an artifact of how the different electron densities were measured (i.e., absolute calibration versus Thomson scattering fit). Those shots with no Chlorine had both electron density measurements and both gave similar results implying that the difference in electron density is not a diagnostic issue. It should be noted that the photometric calibration was completed immediately after the non-Chlorinated shot day and so a year after the Chlorinated data was collected. The photometric calibration is expected to still be accurate to within 20–30% and so does not explain the large electron densities of the Chlorinated data.

Hydrodynamic simulations using the code FLASH predict that the collision times for '0Cl10', '1Cl5', '1Cl10', '6Cl5', and '6Cl10' are 21, 20, 24, 25 and 33 ns respectively [132]. These predicted collision times suggest, like the experiment, that Chlorinated foils are slower due to their increased foil density and that the increased laser-drive increases the jet velocity, causing a collision to occur more quickly. The FLASH predicted electron densities are $\approx 10^{20}$ cm^{-3}, in agreement with the non-Chlorinated foils.

5.3.4 Predicted effect of Chlorine, flow velocity, electron temperature and electron density on the jet interactions

The effect that the different parameters in the experiment have on equilibration times and dimensionless parameters can be examined theoretically. This illustrates which parameters are most important to the dynamics of the jet interaction. The Chlorine

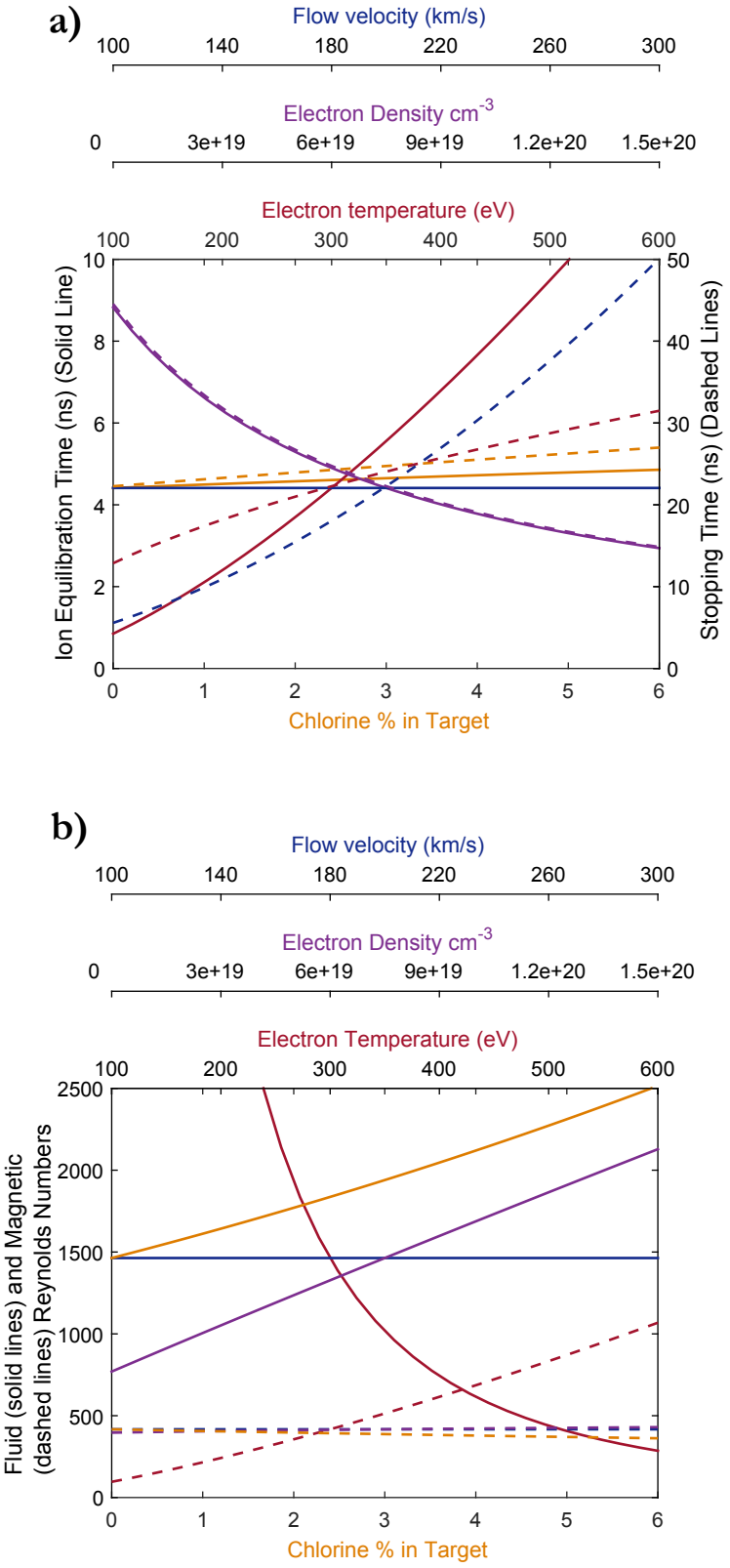

Figure 5.10: Calculated dependence on experimental parameters: a) The effect of changing different parameters on the ion-equilibration time (solid) and the transverse beam stopping time (dashed) are plotted. b) The effects of changing different parameters on the fluid Reynold's number (solid) and magnetic Reynold's number (dashed). The percentage of Chlorine within the targets (yellow) is varied from 0%–6%; the electron temperature (red) is varied from 100–600; the electron density (purple) is varied from 0.1–1.5 $\times$ 10^{20} cm^{-3}; the flow velocity (blue) is varied from 100–300 km/s.

content (which alters the ionization and atomic mass), electron temperature, electron density and jet velocity are varied and then the different properties are calculated. These parameters are varied from the following values of: 0% Chlorine, 300 eV electron temperature, 10^{20} cm^{-3} electron density and a jet velocity of 200 km/s.

Comparing the ion-equilibration time (solid lines) and transverse spreading time (dashed lines) of the two plasma jets for the range in parameters observed in the experiment, it is seen in Figure 5.10a that the ion-equilibration time is 1–10 ns and the stopping time ranges between 1–50 ns. The ion-equilibration time is most affected by the electron temperature and density whilst the transverse stopping time is most affected by the jet velocity and electron density. Consequently changes in the intensity of the drive beams and regions of denser material has a greater effect on the interaction of the two jets than the addition of Chlorine to the targets.

The fluid Reynolds number (solid lines) and magnetic Reynolds number (dashed lines) can be compared in Figure 5.10b. The velocity scale used when calculating the Reynolds' numbers is the turbulent velocity which remains unchanged throughout.

The fluid Reynolds number increases by a factor ≤ 2 as the percentage of Chlorine increases. The fluid and magnetic Reynolds number is most greatly affected by changes in electron temperature.

The fluid Reynold's numbers accessed by the experiment are consistently ≥ 500 and are ~ 1000 for typical jet-interaction parameters. The magnetic Reynold's numbers accessed by the experiment are ≥ 100 throughout the experiment and ~ 500 for typical jet-interaction parameters. This also indicates that the Prandtl number Re/Rm is ≤ 1 throughout the experiment.

By accessing a magnetic Reynold's number ≥ 300 for a Prandtl number ≤ 1, the experiment has reached a regime above the critical magnetic Reynold's number and so the threshold, as predicted by simulations [17], for a turbulent dynamo mechanism.

Figure 5.10 show that the addition of Chlorine to the targets does not have a large

effect on the predicted plasma parameters most important to the jet dynamics. This suggests that the main difference between the Chlorinated and non-Chlorinated shots is due to the initial disparity in electron density. The flow velocity of the jets and electron temperature appears to have the greatest effect upon the different plasma parameters, suggesting that the laser-drive power is important to the dynamics of the colliding jets.

By calculating the effect the different quantities accessed by the experiment have on the plasma parameters, it can be seen that the plasma regimes accessed are similar for all conditions. The interaction of the two jets is governed by the relaxation times of the species within the jets whilst properties of the turbulent plasma produced are, in part, a result of the different Reynolds numbers involved. Flow velocity, and so laser intensity, has a great effect upon the relaxation times and so the interaction of the jets. Chlorine does not have much effect on the plasma properties. However, Figure 5.9 implies that the addition of Chlorine may result in a lower electron temperature, which does greatly effect the plasma parameters. The small number of shots of each shot type and diagnostic differences between the Chlorinated and non-Chlorinated shots, makes it difficult to say conclusively the effect of doping the target foils with Chlorine. The increase in density from the addition of Chlorine certainly makes the plasma jets slower, which implies that there is less available energy to convert into heat. Chlorine doping also causes the plasma to radiatively cool more quickly, providing a possible explanation for the difference in temperature.

5.4 Conclusion

In this chapter, the Thomson scattering data from an experimental campaign at the OMEGA laser facility has been described. These results show that when two laser-irradiated plasma foils collide, energy is transferred from the fast flowing jets into heating the collided plasma jets. The collided plasma jets are turbulent and

so as the collided plasma twists and folds in on itself, magnetic fields generated from misaligned density and temperature gradients within the jets are amplified by a turbulent dynamo mechanism to become dynamically significant.

In a small number of cases, the target foils were doped with Chlorine or had an increased laser-intensity. The Chlorine increases the density of the foils and so slows down the resultant plasma jets. Conversely, the higher laser-intensity increases the flow velocity of the plasma jets.

Theoretical plasma parameters for the range of quantities accessed by this experiment suggest that Chlorine has some effect on the dynamics of the jets. However quantities such as flow velocity and electron temperature, which are affected by the addition of Chlorine, have a greater effect on the plasma parameters.

This chapter has shown that the information provided by the Thomson scattering diagnostic can help to characterize the interaction of two colliding jets and the resultant turbulent plasma they produce.

Chapter 6

Summary and Future Work

6.1 Summary of Results

The work presented in this thesis has focused primarily on the experimental results from two different laboratory based experiments which have applications relevant to astrophysics. Indeed, within both experiments, the combination of turbulence and magnetic fields has been crucial to the dynamics and outcome of the experiments. Both experiments have astrophysical implications and through these experiments and further work, it is possible to achieve a more thorough understanding of both particle acceleration and the turbulent dynamo mechanism.

Chapter 3 presented the work of an experiment at the LULI laser facility which investigated electron acceleration in a magnetized plasma. The experiment was based on a particle acceleration mechanism that has been observed at the comet and Solar-wind interface. Here, electrons are accelerated by lower-hybrid turbulence. Lower-hybrid waves are generated through the modified two-stream instability, a collisionless instability that is produced through shock reflected counter-streaming ions. Lower-hybrid waves can transfer energy between ions traveling perpendicularly to a background magnetic field to electrons traveling parallel to the background magnetic field through a Cerenkov-like interaction. In this manner, electrons can be acceler-

ated to large energies and so produce X-rays. Within the experiment, there is an excess in X-ray production when a magnetic field is present compared with when there is no magnetic obstacle present. This excess in X-rays in the magnetised case is due to the production of electrons accelerated via lower-hybrid waves within the experiment. In space, lower-hybrid waves are generated when a Solar-wind interacts with a comet and so produces X-rays.

To confirm that lower-hybrid waves are indeed the cause of the excess in X-rays in the magnetised case, scaled PIC simulations were performed to mimic the experiment. In the PIC simulations, high energy electrons are produced and the wave number spectrum from the ions is consistent with lower-hybrid waves. By scaling the accelerated electron energy found in the PIC simulations, the electrons within the experiment are found to be accelerated to 45 eV, from a thermal background of 3 eV. Using the collisional-radiative code PrismSPECT, it can be shown that this hot electron population is sufficient to produce the X-rays observed in the experiment.

Producing an accelerated electron population from the thermal background has important applications for astrophysics. Diffusive shock acceleration whereby charged particles are accelerated by being repeatedly bounced across either side of a shock requires the charged particles to have high, non-thermal velocities to permit multiple shock crossings. Consequently, there must be some initial acceleration mechanism to raise these non-thermal particles from the thermal pool. Lower-hybrid turbulence is one such initial acceleration mechanism. Consequently, this experiment provides a platform on which further experimental investigation can be performed on particle acceleration.

Chapters 4 and 5 discuss the work from an experimental campaign investigating the amplification of magnetic fields through the turbulent dynamo mechanism. To measure the amplified magnetic fields within the generated plasma, a Faraday-rotation diagnostic was implemented. This diagnostic has not been used on the

OMEGA laser facility before and so required a new diagnostic setup, calibration and analysis.

The Faraday-rotation diagnostic was installed on the Thomson scattering probe beam. The scattered light was collected, as usual, and then split by a Wollaston prism into its two polarizations. These two polarizations behave differently in the presence of a magnetic field and so by recording the intensity of the two polarizations, a magnetic field measurement could be inferred. First, a calibration shot with no magnetic field is required so that all changes in polarization intensity on data shots can be correctly interpreted. The ratio in polarization intensity can be converted into a magnetic field measurement provided that the electron density is known.

Whilst in general the electron density can be determined through fitting the Thomson scattered electron features, due to the implementation of the Faraday-rotation diagnostic, it was not possible to make a spectrally resolved measurement. As such, the electron density had to be determined through a full photometric calibration of the entire Thomson scattering and Faraday-rotation system. A photometric calibration is inherently less accurate than measuring the electron density through Thomson scattered electron features. However, by comparing data from both techniques, the electron density determined through a photometric calibration is similar to that measured by the Thomson scattered electron features. Once the electron density has been measured, the magnetic field can be determined from the Faraday-rotation diagnostic.

The path-integrated magnetic field as measured from Faraday-rotation was compared with that from proton radiography. The two diagnostics gave similar results. Whilst proton radiography can reveal a 2D reconstruction of the magnetic field, this takes time to perform and the data is not available on shot day. An advantage of Faraday rotation is that the analysis can be performed during the shot day and is coupled into the Thomson scattering diagnostic, reducing the total number of

diagnostic ports required for the experiment.

Chapter 5 discusses the results from the Thomson scattering data recorded at an experiment investigating the turbulent dynamo mechanism at the OMEGA laser facility. The experimental results were taken over several shot days and so there are some changes between the experimental shot days. The material composition of the target foils was varied to include different amounts of Chlorine doping. Further, some of the shots have an increased laser intensity, increasing the resultant flow velocity of the plasma jets.

The Thomson scattering data can provide information on a variety of quantities including electron and ion temperature, flow velocity, electron density and turbulent broadening. Expanding the electron susceptibility to include gradients within the plasma allows a measurement of spatial gradients to be inferred. Whilst it was not possible to gather a measurement of the spatial gradients for the majority of the data, as a proof of principle, it may be possible to measure these spatial gradients within the plasma on future experiments. The collated data on the different plasma quantities can then be used to interpret the flow dynamics of the plasma jets.

On collision, the non-Chlorinated plasma jets rapidly increase in temperature and electron density as material flows into the interaction region and transfers energy from the flowing jets into heating the turbulent region. As time passes, the plasma begins to cool, presumably transferring much of its energy into generating magnetic fields. The plasma is turbulent and so different regions of the plasma have slightly different densities and move around one another with some outer scale turbulent velocity. This outer scale turbulent velocity can be inferred as a broadening of the Thomson scattered ion features. As the plasma twists and turns through its turbulent motions, the magnetic field frozen into the plasma is amplified many times over in a turbulent dynamo mechanism. The measured Thomson scattering parameters confirm that a magnetic field will indeed be frozen into the plasma since the magnetic

Reynolds number is large for the plasma in this experiment.

The collision and interaction of those jets doped with Chlorine and different laser drives is similar to that of the non-Chlorinated jets. It appears that the Chlorine somewhat slows down the plasma jets and cools the resultant plasma. Those targets doped with Chlorine had a significantly higher mass density than those without. This increased density could be the cause of the difference in flow velocity of the Chlorinated jets. Further, if the jet velocities are smaller, there will be less available energy to transfer into thermal energy thus resulting in a smaller electron temperature. The relatively small number of Chlorinated shots with the exact same target conditions makes comparisons extremely difficult as it is unknown when the collision occurred for each condition as well as if a particular shot is probing an unusually hot or dense region of plasma. To try and disentangle whether or not Chlorine should have a great effect on the plasma parameters and regime considered here, theoretical plasma parameters were calculated for the parameter range accessed by the experiment.

Different relaxation processes and dimensionless parameters were calculated for the range of parameters measured within the experiment. It is readily seen that the addition of Chlorine does not affect the ion-equilibration time, transverse beam spreading time or the Reynolds numbers of the flows by a large amount. Instead, changing the flow velocity and electron temperature has the greatest effect upon the calculated parameters. The parameters accessed by the experiment all fall into the same regime. The resultant plasma is collisional and the ion-electron equilibration time is small enough ~ 9 ns to allow the plasma to be treated as in thermal equilibrium. The length scale of collisions is small ~ 2 μm and prevents the formation of electrostatic instabilities. The plasma can be reasonably described by MHD. Lastly, the magnetic Reynolds number is sufficiently greater than the critical value as predicted by simulations, suggesting that in all cases a turbulent dynamo mechanism

could be at work. It would seem that the addition of Chlorine increases the target foil density and so decreases the flow velocity of the jets, lowering the electron temperature of the plasma. Consequently it would seem it is the reduced flow velocity that has the greatest effect on the generated plasma rather than the Chlorine itself.

This experiment is part of a larger campaign to understand the role turbulence plays in astrophysical plasmas. This on-going campaign has observed amplification of magnetic fields through the turbulent dynamo mechanism. Future work based on a similar setup aims to investigate the possibility of particle acceleration as well as further investigating different aspects of the turbulent dynamo mechanism.

6.2 Future Work

In terms of an experimental standpoint, there is much that can be further investigated. Particle acceleration is a currently hotly studied topic. Lower hybrid turbulence is one mechanism by which particles can be accelerated. This lower hybrid method of particle acceleration could be further investigated at a larger scale laser facility than LULI such as Omega. A higher powered laser facility would increase the flow velocity, v. Since the accelerated electron energy is proportional to v^2, a modest increase in flow velocity could greatly increase the accelerated electron energy. Further, following from the work of Ref. [44], this faster flow lends itself to a collisionless shock which would allow the modified two-stream instability, necessary for the generation of lower hybrid waves, to the develop un-hindered by collisions.

A multi-kJ laser facility can produce typical flow velocities ≈ 1000 km/s [44, 140], which could increase the average electron energy to ≈ 5 keV. At this increased electron energy, the electrons themselves could be recorded on an electron spectrometer, rather than inferring the electron energy from the resultant X-rays. An electron energy spectra has useful astrophysical applications. The exact shape of the electron energy spectra is a debated topic since it depends on the exact form of the hot

electron distribution function [141].

Additionally, a Thomson scattering diagnostic could be included to gather more information about the shock reflected ions. Previous work has shown evidence of a peak in the Thomson scattering spectra due to reflected ions [112, 142]. Inclusion of a Thomson scattering diagnostic could provide direct evidence of shock-reflected ions and also indicate the fraction of ions reflected off of the shock [102]. Whilst shock-reflected ions were inferred from the measured data at LULI, direct evidence would enable less reliance on simulations and theoretical predictions when deriving the accelerated electron energy. Further experiments could more thoroughly investigate the exact nature of electron acceleration via lower hybrid turbulence.

Particle acceleration is a phenomenon that commonly occurs in turbulent regions. As such, one of the future goals of the turbulent dynamo campaign is to investigate particle acceleration. Stochastic acceleration through a Fermi like process is expected to occur within the turbulent plasma and so is currently being investigated.

The turbulent dynamo mechanism is a complicated process which has been investigated through numerous simulations in multiple regimes. Having demonstrated magnetic field amplification through the turbulent dynamo mechanism, it would be instructive if it was possible to 'turn off' the dynamo mechanism whilst keeping the same flow properties i.e., to reduce the magnetic Reynolds number by increasing the magnetic diffusivity. This could potentially be achieved by increasing the ionization of the plasma whilst decreasing the temperature through doping the foil with a high Z material.

The experimental platform as it currently exists can provide further information. The kinetic and magnetic energy spectra are theoretically informative. Increasing the dynamic range of both the X-ray spectra and the proton radiographs would increase the range in wavenumbers over which the spectra cover, allowing the power spectra to be more accurately determined.

Focusing on developments that can be made to the Thomson scattering diagnostic, it would be interesting to be able to confirm that spatial gradients within the plasma can be accurately measured. The work shown here has demonstrated that spatial gradients can be measured, although this was only possible for one shot. Learning how the development of the turbulence affects inhomogeneities within the plasma would be an interesting measurement. Further, it would be useful to include heat flux into the Thomson scattering code to see how temperature gradients affect the plasma.

Whilst the Thomson scattering diagnostic has been used in imaging mode i.e., spatially resolved, the Faraday rotation diagnostic has not yet been spatially resolved. Imaging Faraday rotation would allow the length scale over which the magnetic field changes be determined. This would have useful applications when investigating the turbulent dynamo mechanism. Changing the Faraday rotation setup to act in an imaging mode should be a small alteration the existing diagnostic setup.

Overall, there are several further pursuits that these experiments could take. Further investigations into particle acceleration and the turbulent dynamo mechanism would provide fruitful experimental verification of theoretical predictions.

Bibliography

[1] Bruce A Remington. High energy density laboratory astrophysics. *Plasma Physics and Controlled Fusion*, 47(5A):A191, 2005. 1

[2] R Paul Drake. Radiative shocks in astrophysics and the laboratory. In *High Energy Density Laboratory Astrophysics*, pages 49–59. Springer, 2005. 1

[3] E Falize, Claire Michaut, and Serge Bouquet. Similarity properties and scaling laws of radiation hydrodynamic flows in laboratory astrophysics. *The Astrophysical Journal*, 730(2):96, 2011. 1

[4] J M Foster, B H Wilde, P A Rosen, R J R Williams, B E Blue, R F Coker, R P Drake, A Frank, P A Keiter, A M Khokhlov, and Others. High-energy-density laboratory astrophysics studies of jets and bow shocks. *The Astrophysical Journal Letters*, 634(1):L77, 2005. 1

[5] Yuri P Zakharov. Collisionless laboratory astrophysics with lasers. *IEEE transactions on plasma science*, 31(6):1243–1251, 2003. 1

[6] D D Ryutov, R P Drake, and B A Remington. Criteria for scaled laboratory simulations of astrophysical MHD phenomena. *The Astrophysical Journal Supplement Series*, 127(2):465, 2000. 1

[7] Joseph E Cross, Brian Reville, and Gianluca Gregori. Scaling of magneto-quantum-radiative hydrodynamic equations: from laser-produced plasmas to astrophysics. *The Astrophysical Journal*, 795(1):59, 2014. 1

[8] T R Boehly, R L McCrory, C P Verdon, W Seka, S J Loucks, A Babushkin, R E Bahr, R Boni, D K Bradley, R S Craxton, and Others. Inertial confinement fusion experiments with OMEGA-A 30-kJ, 60-beam UV laser. *Fusion engineering and design*, 44(1-4):35–42, 1999. 1

[9] C Yamanaka, K Mima, and S Nakai. Inertial confinement fusion research by GEKKO lasers at ILE Osaka and target design for ignition. In *Plasma physics and controlled nuclear fusion research 1986*. 1987. 1

[10] S V Lebedev, J P Chittenden, F N Beg, S N Bland, A Ciardi, D Ampleford, S Hughes, M G Haines, A Frank, E G Blackman, and Others. Laboratory astrophysics and collimated stellar outflows: The production of radiatively cooled hypersonic plasma jets. *The Astrophysical Journal*, 564(1):113, 2002. 1

[11] M D Knudson, D L Hanson, J E Bailey, C A Hall, and J R Asay. Use of a wave reverberation technique to infer the density compression of shocked liquid deuterium to 75 GPa. *Physical review letters*, 90(3):35505, 2003. 1

[12] Axel Brandenburg and Kandaswamy Subramanian. Astrophysical magnetic fields and nonlinear dynamo theory. *Physics Reports*, 417(1-4):1–209, 2005. 1, 2.5.2

[13] Roger D Blandford and James P Ostriker. Particle acceleration by astrophysical shocks. *The Astrophysical Journal*, 221:L29—-L32, 1978. 1, 2.4, 3.1

[14] Dongsu Ryu, Hyesung Kang, Jungyeon Cho, and Santabrata Das. Turbulence and magnetic fields in the large-scale structure of the universe. *Science*, 320(5878):909–912, 2008. 1, 5.1

[15] Francesco Miniati and Andrey Beresnyak. Self-similar energetics in large clusters of galaxies. *Nature*, 523(7558):59, 2015. 1, 5.1

[16] Ellen G Zweibel and Carl Heiles. Magnetic fields in galaxies and beyond. *Nature*, 385(6612):131, 1997. 1, 5.1

[17] Alexander A Schekochihin and Steven Charles Cowley. Turbulence, magnetic fields, and plasma physics in clusters of galaxies. *Physics of Plasmas*, 13(5):56501, 2006. 1, 2.5.2, 5.1, 5.3.4

[18] P Tzeferacos, A Rigby, A F A Bott, A R Bell, R Bingham, A Casner, F Cattaneo, E M Churazov, J Emig, F Fiuza, and Others. Laboratory evidence of dynamo amplification of magnetic fields in a turbulent plasma. *Nature communications*, 9(1):591, 2018. 1, 5.1, 5.3.1, 5.3.2, 5.3.2

[19] Enrico Fermi. Galactic Magnetic Fields and the Origin of Cosmic Radiation. *The Astrophysical Journal*, 119:1, 1954. 1, 2.5.1

[20] W I Axford, E Leer, and G Skadron. Acceleration of cosmic rays by shock waves. 1978. 1

[21] James J Beatty and Stefan Westerhoff. The highest-energy cosmic rays. *Annual Review of Nuclear and Particle Science*, 59:319–345, 2009. 1

[22] Ray J Protheroe and R W Clay. Ultra high energy cosmic rays. *Publications of the Astronomical Society of Australia*, 21(1):1–22, 2004. 1, 2.2

[23] J Abraham and Pierre Auger Collaboration. Correlation of the highest-energy cosmic rays with nearby extragalactic objects. 2007. 1

[24] Anatoly Spitkovsky. Particle acceleration in relativistic collisionless shocks: Fermi process at last? *The Astrophysical Journal Letters*, 682:8–11, 2008. 1

[25] R Bingham, J M Dawson, V D Shapiro, D A Mendis, and B J Kellett. Generation of X-rays from Comet C/Hyakutake 1996 B2. *Science*, 275(5296):49–51, 1997. 1, 3.1, 3.1.1, 3.1.2, 3.2, 3.5.1, 3.5.2

[26] A Rigby, F Cruz, B Albertazzi, R Bamford, A R Bell, J E Cross, G Fraschetti, P Graham, Y Hara, P M Kozlowski, and Others. Electron Acceleration by Wave Turbulence in a Magnetised Plasma (accepted). *Nature Physics*, 2018. 1, 3.7

[27] F Chen Francis and Others. Introduction to plasma physics and controlled fusion. *Plasma Physics*, 1984. 2.1.1, 2.1.2, 2.2, 2.3, 2.3.1

[28] Thomas James Morrow Boyd and Jeffrey John Sanderson. *The physics of plasmas*. Cambridge University Press, 2003. 2.1.2, 2.2, 2.2.1, 2.3.1, 2.3.2, 2.6

[29] Joseph D Huba. NRL: Plasma formulary. Technical report, NAVAL RESEARCH LAB WASHINGTON DC BEAM PHYSICS BRANCH, 2004. 2.1.4, 2.1.4, 2.1

[30] Peter Mulser and Dieter Bauer. *High power laser-matter interaction*, volume 238. Springer, 2010. 2.2, 2.6

[31] Richard O Dendy. *Plasma physics: an introductory course*. Cambridge University Press, 1995. 2.2.1

[32] Thomas H Stix. *Waves in plasmas*. Springer Science & Business Media, 1992. 2.3

[33] Lev Davidovich Landau. On the vibrations of the electronic plasma. *Zh. Eksp. Teor. Fiz.*, 10:25, 1946. 2.3.1

[34] Yu A Omelchenko, R A Sagdeev, V D Shapiro, and V I Shevchenko. Numerical simulation of quasilinear relaxation of an ion ring and production of superthermal electrons. *Sov. J. Plasma Phys*, 15:427, 1989. 2.3.2, 3.1.1

[35] J L Han, R N Manchester, and G J Qiao. Pulsar rotation measures and the magnetic structure of our Galaxy. *Monthly Notices of the Royal Astronomical Society*, 306(2):371–380, 1999. 2.3.2

[36] V Formisano and P C Hedgecock. Solar wind interaction with the Earth's magnetic field: 3. On the Earth's bow shock structure. *Journal of Geophysical Research*, 78(19):3745–3760, 1973. 2.4

[37] Reinout J Van Weeren, Huub J A Röttgering, Marcus Brüggen, and Matthias Hoeft. Particle acceleration on megaparsec scales in a merging galaxy cluster. *Science*, 330(6002):347–349, 2010. 2.4, 3.1

[38] André Balogh and Rudolf A Treumann. *Physics of collisionless shocks: space plasma shock waves*. Springer Science & Business Media, 2013. 2.4

[39] D W Forslund, K B Quest, J U Brackbill, and K Lee. Collisionless dissipation in quasi-perpendicular shocks. *Journal of Geophysical Research: Space Physics*, 89(A4):2142–2150, 1984. 2.4

[40] Takayuki Umeda, Yoshitaka Kidani, Shuichi Matsukiyo, and Ryo Yamazaki. Modified two-stream instability at perpendicular collisionless shocks: Full particle simulations. *Journal of Geophysical Research: Space Physics*, 117(A3), 2012. 2.4

[41] Alexandre Marcowith, Antoine Bret, Andrei Bykov, Mark Eric Dieckman, L O'C Drury, Bertrand Lembège, Martin Lemoine, Giovanni Morlino, Gareth Murphy, Guy Pelletier, and Others. The microphysics of collisionless shock waves. *Reports on Progress in Physics*, 79(4):46901, 2016. 2.4, 3.1, 3.1.1

[42] Derek A Tidman and Nicholas A Krall. Shock waves in collisionless plasmas. *American Journal of Physics*, 40(7):1055, 1972. 2.4

[43] R Paul Drake. *High-energy-density physics: fundamentals, inertial fusion, and experimental astrophysics*. Springer Science & Business Media, 2006. 2.1, 2.4

[44] H-S Park, C M Huntington, F Fiuza, R P Drake, D H Froula, G Gregori, M Koenig, N L Kugland, C C Kuranz, D Q Lamb, and Others. Collisionless shock experiments with lasers and observation of Weibel instabilities. *Physics of Plasmas*, 22(5):56311, 2015. 2.5, 6.2

[45] J E Cross, G Gregori, J M Foster, P Graham, J-M Bonnet-Bidaud, C Busschaert, N Charpentier, C N Danson, H W Doyle, R P Drake, and Others. Laboratory analogue of a supersonic accretion column in a binary star system. *Nature communications*, 7:ncomms11899, 2016. 2.5

[46] C C Kuranz, R P Drake, E C Harding, M J Grosskopf, H F Robey, B A Remington, M J Edwards, A R Miles, T S Perry, B E Blue, and Others. Two-dimensional blast-wave-driven Rayleigh-Taylor instability: experiment and simulation. *The Astrophysical Journal*, 696(1):749, 2009. 2.5

[47] K Koyama, R Petre, E V Gotthelf, U Hwang, M Matsuura, M Ozaki, and S S Holt. Evidence for shock acceleration of high-energy electrons in the supernova remnant SN1006. *Nature*, 378(6554):255, 1995. 2.5.1, 3.1

[48] Roger Blandford and David Eichler. Particle acceleration at astrophysical shocks: A theory of cosmic ray origin. *Physics Reports*, 154(1):1–75, 1987. 2.5.1

[49] Enrico Fermi. On the origin of the cosmic radiation. *Physical Review*, 75(8):1169, 1949. 2.5.1

[50] Russell M Kulsrud and Attilio Ferrari. The relativistic quasilinear theory of particle acceleration by hydromagnetic turbulence. *Astrophysics and Space Science*, 12(2):302–318, 1971. 2.5.1

[51] Ramanath Cowsik and Subir Sarkar. The evolution of supernova remnants as radio sources. *Monthly Notices of the Royal Astronomical Society*, 207(4):745–775, 1984. 2.5.1

[52] A R Bell. The acceleration of cosmic rays in shock fronts–I. *Monthly Notices of the Royal Astronomical Society*, 182(2):147–156, 1978. 2.5.1

[53] Mario A Riquelme and Anatoly Spitkovsky. Electron injection by whistler waves in non-relativistic shocks. *The Astrophysical Journal*, 733(1):63, 2011. 2.5.1, 3.1

[54] Ludwig Biermann and Arnulf Schlüter. Cosmic radiation and cosmic magnetic fields. II. Origin of cosmic magnetic fields. *Physical Review*, 82(6):863, 1951. 2.5.2, 2.5.2

[55] Russell M Kulsrud, Renyue Cen, Jeremiah P Ostriker, and Dongsu Ryu. The protogalactic origin for cosmic magnetic fields. *The Astrophysical Journal*, 480(2):481, 1997. 2.5.2, 2.5.2

[56] Eugene Newman Parker. Cosmical magnetic fields: Their origin and their activity. *Oxford, Clarendon Press; New York, Oxford University Press, 1979, 858 p.*, 1979. 2.5.2

[57] Ia B Zeldovich, Aleksandr Andreevich Ruzmaikin, and Dmitrij Dmitrievič Sokolov. Magnetic fields in astrophysics. In *New York, Gordon and Breach Science Publishers (The Fluid Mechanics of Astrophysics and Geophysics. Volume 3), 1983, 381 p. Translation.*, volume 3, 1983. 2.5.2, 5.1

[58] Katepalli R Sreenivasan. Fluid turbulence. *Reviews of Modern Physics*, 71(2):S383, 1999. 2.5.2

[59] Andrey Nikolaevich Kolmogorov. The local structure of turbulence in incompressible viscous fluid for very large Reynolds numbers. In *Dokl. Akad. Nauk SSSR*, volume 30, pages 299–303, 1941. 2.5.2, 5.2.1

[60] Andrey Beresnyak. Universal nonlinear small-scale dynamo. *Physical Review Letters*, 108(3):35002, 2012. 2.5.2

[61] Nils Erland L Haugen, Axel Brandenburg, and Wolfgang Dobler. Simulations of nonhelical hydromagnetic turbulence. *Physical Review E*, 70(1):16308, 2004. 2.5.2

[62] Alexander A Schekochihin, Steven C Cowley, Samuel F Taylor, Jason L Maron, and James C McWilliams. Simulations of the small-scale turbulent dynamo. *The Astrophysical Journal*, 612(1):276, 2004. 2.5.2, 5.1

[63] S I Vainshtein and Ya B Zel'Dovich. REVIEWS OF TOPICAL PROBLEMS: Origin of Magnetic Fields in Astrophysics (Turbulent" Dynamo" Mechanisms). *Soviet Physics Uspekhi*, 15:159–172, 1972. 2.5.2

[64] Vladimir E Fortov. *Extreme states of matter: on Earth and in the Cosmos*. Springer Science & Business Media, 2010. 2.6

[65] L Schlessinger and J Wright. Inverse-bremsstrahlung absorption rate in an intense laser field. *Phys. Rev. A*, 20(5):1934–1945, nov 1979. 2.6

[66] D E Evans and J Katzenstein. Laser light scattering in laboratory plasmas. *Reports on Progress in Physics*, 32(1):207, 1969. 2.7, 2.7.4, 4.5, 5.2.1, 5.3.1

[67] E A McLean and S A Ramsden. Optical interferometric and spectroscopic measurements of electron density in a plasma. *Physical Review*, 140(4A):A1122, 1965. 2.7.1

[68] Takashi Fujimoto. *Plasma spectroscopy*, volume 123. Oxford University Press on Demand, 2004. 2.7.2

[69] Hans-Joachim Kunze. *Introduction to plasma spectroscopy*, volume 56. Springer Science & Business Media, 2009. 2.7.2

[70] Jakoub Szlachetko, M Nachtegaal, E De Boni, M Willimann, O Safonova, J Sa, G Smolentsev, Monika Szlachetko, J A Van Bokhoven, J-Cl Dousse, and Others. A von Hamos x-ray spectrometer based on a segmented-type diffraction crystal for single-shot x-ray emission spectroscopy and time-resolved resonant inelastic x-ray scattering studies. *Review of Scientific Instruments*, 83(10):103105, 2012. 2.7.3

[71] Alexander P Shevelko. X-ray spectroscopy of laser-produced plasmas using a von Hamos spectrograph. In *Current Russian Research in Optics and Photonics: New Methods and Instruments for Space-and Earth-based Spectroscopy in XUV, UV, IR, and Millimeter Waves*, volume 3406, pages 91–109. International Society for Optics and Photonics, 1998. 2.7.3, 3.4.1, 3.4.2

[72] John Sheffield, Dustin Froula, Siegfried H Glenzer, and Neville C Luhmann Jr. *Plasma scattering of electromagnetic radiation: theory and measurement techniques*. Academic press, 2010. 2.7.4, 2.3, 2.7.4, 5.2, 5.2.1

[73] John David Jackson. Classical electrodynamics, 1999. 2.7.4

[74] A F A Bott, C Graziani, P Tzeferacos, T G White, D Q Lamb, G Gregori, and A A Schekochihin. Proton imaging of stochastic magnetic fields. *Journal of Plasma Physics*, 83(6), 2017. 2.7.5, 4.1, 4.2, 4.6

[75] Petros Tzeferacos, Milad Fatenejad, Norbert Flocke, Carlo Graziani, G Gregori, D Q Lamb, D Lee, J Meinecke, A Scopatz, and K Weide. FLASH MHD simulations of experiments that study shock-generated magnetic fields. *High Energy Density Physics*, 17:24–31, 2015. 2.8, 3.3.2

[76] Bruce Fryxell, Kevin Olson, Paul Ricker, F X Timmes, Michael Zingale, D Q Lamb, Peter MacNeice, Robert Rosner, J W Truran, and H Tufo. FLASH: An adaptive mesh hydrodynamics code for modeling astrophysical thermonuclear flashes. *The Astrophysical Journal Supplement Series*, 131(1):273, 2000. 2.8

[77] Anshu Dubey, Katie Antypas, Murali K Ganapathy, Lynn B Reid, Katherine Riley, Dan Sheeler, Andrew Siegel, and Klaus Weide. Extensible component-based architecture for FLASH, a massively parallel, multiphysics simulation code. *Parallel Computing*, 35(10-11):512–522, 2009. 2.8

[78] Ricardo A Fonseca, Lu\'\is O Silva, Frank S Tsung, Viktor K Decyk, Wei Lu, Chuang Ren, Warren B Mori, S Deng, S Lee, T Katsouleas, and Others. OSIRIS: A three-dimensional, fully relativistic particle in cell code for modeling plasma based accelerators. In *International Conference on Computational Science*, pages 342–351. Springer, 2002. 2.8, 3.5.1

[79] Joseph MacFarlane, I Golovkin, P Wang, P Woodruff, J Bailey, T Mehlhorn, and G Rochau. Simulation of the Spectral Properties of Materials with Prism-SPECT. In *APS Meeting Abstracts*, 2007. 2.8, 5.2.1

[80] Adam Masters, Lukasz Stawarz, Masaki Fujimoto, STEVEN J Schwartz, Nick Sergis, MICHELLE F Thomsen, Alessandro Retino, Hiroshi Hasegawa, Bertalan Zieger, GETHYN R Lewis, and Others. Electron acceleration to relativistic energies at a strong quasi-parallel shock wave. *Nature Physics*, 9(3):nphys2541, 2013. 3.1

[81] D A Green. A catalogue of 294 Galactic supernova remnants. *arXiv preprint arXiv:1409.0637*, 2014. 3.1

[82] T AMANO and M HOSHINO. Electron Injection at Quasi-Perpendicular Supernova Remnant Shocks. 3.1

[83] K G McClements, R O Dendy, R Bingham, J G Kirk, and L O'C Drury. Acceleration of cosmic ray electrons by ion-excited waves at quasiperpendicular shocks. *Monthly Notices of the Royal Astronomical Society*, 291(1):241–249, 1997. 3.1.1

[84] R Bingham, B J Kellett, J M Dawson, V D Shapiro, and D A Mendis. X-ray emission from comets, cometary knots, and supernova remnants. *The Astrophysical Journal Supplement Series*, 127(2):233, 2000. 3.1.1, 3.1.1

[85] J Martin Laming. Accelerated electrons in Cassiopeia A: Thermal and electromagnetic effects. *The Astrophysical Journal*, 563(2):828, 2001. 3.1.1

[86] Jacco Vink and J Martin Laming. On the magnetic fields and particle acceleration in Cassiopeia A. *The Astrophysical Journal*, 584(2):758, 2003. 3.1.1

[87] John B McBride, Edward Ott, Jay P Boris, and Joseph H Orens. Theory and simulation of turbulent heating by the modified two-stream instability. *The Physics of Fluids*, 15(12):2367–2383, 1972. 3.1.1, 3.3.3

[88] Nathaniel J Fisch. Theory of current drive in plasmas. *Reviews of Modern Physics*, 59(1):175, 1987. 3.1.1

[89] R Cesario, L Amicucci, A Cardinali, C Castaldo, M Marinucci, L Panaccione, F Santini, O Tudisco, M L Apicella, G Calabro, and Others. Current drive at plasma densities required for thermonuclear reactors. *Nature Communications*, 1:55, 2010. 3.1.1

[90] M Porkolab, B Lloyd, Y Takase, P Bonoli, C Fiore, R Gandy, R Granetz, D Griffin, D Gwinn, B Lipschultz, and Others. High-power electron Landau-heating experiments in the lower hybrid frequency range in a tokamak plasma. *Physical review letters*, 53(13):1229, 1984. 3.1.1

[91] D D Barbosa, A Eviatar, and G L Siscoe. On the acceleration of energetic ions in Jupiter's magnetosphere. *Journal of Geophysical Research: Space Physics*, 89(A6):3789–3800, 1984. 3.1.1

[92] J C Weatherall and J Eilek. Diffuse Thermal and Relativistic Plasma in Galaxy Clusters. In *Proceedings of the Workshop held at Ringberg Castle (19–23, 1999), eds. H. Bohringer, L. Feretti, PS Garching, Max-Planck-Institut fur Extraterrestrische Physik (Germany, 1999)*, page 255, 1999. 3.1.1

[93] A A Galeev. Acceleration of electrons to ultrarelativistic energies by shock waves and synchrotron radiation of these electrons. *Sov. Phys. JETP*, 59(5):965–971, 1984. 3.1.1

[94] Martin Torney, R Bingham, J M Dawson, B J Kellett, V D Shapiro, and H Summers. Modelling X-ray line and continuum emission from comets. *Physica Scripta*, 2002(T98):168, 2002. 3.1.2

[95] T E Cravens. Comet Hyakutake x-ray source: Charge transfer of solar wind heavy ions. *Geophysical Research Letters*, 24(1):105–108, 1997. 3.1.2

[96] P Beiersdorfer, K R Boyce, G V Brown, H Chen, S M Kahn, R L Kelley, M May, R E Olson, F S Porter, C K Stahle, and Others. Laboratory simulation of charge exchange-produced X-ray emission from comets. *Science*, 300(5625):1558–1559, 2003. 3.1.2, 3.2

[97] Iver H Cairns and G P Zank. Turn-on of 2–3 kHz radiation beyond the heliopause. *Geophysical research letters*, 29(7), 2002. 3.2

[98] Yu P Zakharov, V M Antonov, A V Melekhov, S A Nikitin, A G Ponomarenko, V G Posukh, V O Stoyanovsky, and I F Shaikhislamov. Simulation of astrophysical plasma dynamics in the laser experiments. In *AIP Conference Proceedings*, volume 369, pages 357–362. AIP, 1996. 3.2

[99] J J MacFarlane, I E Golovkin, P Wang, P R Woodruff, and N A Pereyra. SPECT3D–A multi-dimensional collisional-radiative code for generating diagnostic signatures based on hydrodynamics and PIC simulation output. *High energy density physics*, 3(1-2):181–190, 2007. 3.4

[100] M Hipp, J Woisetschläger, P Reiterer, and T Neger. Digital evaluation of interferograms. *Measurement*, 36(1):53–66, 2004. 3.3.1

[101] A R Bell, P Choi, A E Dangor, O Willi, D A Bassett, and C J Hooker. Collisionless shock in a laser-produced ablating plasma. *Physical Review A*, 38(3):1363, 1988. 3.3.1

[102] S V Lebedev, L Suttle, G F Swadling, M Bennett, S N Bland, G C Burdiak, D Burgess, J P Chittenden, A Ciardi, A Clemens, and Others. The formation of reverse shocks in magnetized high energy density supersonic plasma flows. *Physics of Plasmas*, 21(5):56305, 2014. 3.3.1, 6.2

[103] Phillip Colella and Paul R Woodward. The piecewise parabolic method (PPM) for gas-dynamical simulations. *Journal of computational physics*, 54(1):174–201, 1984. 3.3.2

[104] Dongwook Lee. A solution accurate, efficient and stable unsplit staggered mesh scheme for three dimensional magnetohydrodynamics. *Journal of Computational Physics*, 243:269–292, 2013. 3.3.2

[105] Shengtai Li. An HLLC Riemann solver for magneto-hydrodynamics. *Journal of computational physics*, 203(1):344–357, 2005. 3.3.2

[106] J P Edmiston and C F Kennel. A parametric survey of the first critical Mach number for a fast MHD shock. *Journal of plasma physics*, 32(3):429–441, 1984. 3.3.3

[107] R Z SAGDEEV. Cooperative Phenomena and Shock Waves in Collisionless Plasmas. *Rev Plasma Phys*, 4:23, 1966. 3.3.3

[108] F Cruz, E P Alves, R A Bamford, R Bingham, R A Fonseca, and L O Silva. Formation of collisionless shocks in magnetized plasma interaction with kinetic-scale obstacles. *Physics of Plasmas*, 24(2):22901, 2017. 3.5.1

[109] G Gregori, B Reville, and Francesco Miniati. The generation and amplification of intergalactic magnetic fields in analogue laboratory experiments with high power lasers. *Physics Reports*, 601:1–34, 2015. 3.5.2, 4.1, 5.1

[110] E T Everson, P Pribyl, C G Constantin, A Zylstra, D Schaeffer, N L Kugland, and C Niemann. Design, construction, and calibration of a three-axis, high-frequency magnetic probe (B-dot probe) as a diagnostic for exploding plasmas. *Review of Scientific Instruments*, 80(11):113505, 2009. 4.1

[111] C K Li, F H Séguin, J A Frenje, J R Rygg, R D Petrasso, R P J Town, P A Amendt, S P Hatchett, O L Landen, A J Mackinnon, and Others. Measuring E and B fields in laser-produced plasmas with monoenergetic proton radiography. *Physical review letters*, 97(13):135003, 2006. 4.1

[112] G F Swadling, S V Lebedev, G N Hall, S Patankar, N H Stewart, R A Smith, A J Harvey-Thompson, G C Burdiak, P de Grouchy, J Skidmore, and Others. Diagnosing collisions of magnetized, high energy density plasma flows using a combination of collective Thomson scattering, Faraday rotation, and interferometry. *Review of Scientific Instruments*, 85(11):11E502, 2014. 4.1, 6.2

[113] Muhammad Firmansyah Kasim, Luke Ceurvorst, Naren Ratan, James Sadler, Nicholas Chen, Alexander Sävert, Raoul Trines, Robert Bingham, Philip N Burrows, Malte C Kaluza, and Others. Quantitative shadowgraphy and proton radiography for large intensity modulations. *Physical Review E*, 95(2):23306, 2017. 4.1

[114] Jena Meinecke, Petros Tzeferacos, Anthony Bell, Robert Bingham, Robert Clarke, Eugene Churazov, Robert Crowston, Hugo Doyle, R Paul Drake, Robert Heathcote, and Others. Developed turbulence and nonlinear amplification of magnetic fields in laboratory and astrophysical plasmas. *Proceedings of the National Academy of Sciences*, 112(27):8211–8215, 2015. 4.1, 5.1

[115] A Davies, D Haberberger, R Boni, S Ivancic, R Brown, and D H Froula. Polarimetry diagnostic on OMEGA EP using a 10-ps, 263-nm probe beam. *Review of Scientific Instruments*, 85(11):11E611, 2014. 4.1

[116] P Tzeferacos, A Rigby, A Bott, A R Bell, R Bingham, A Casner, F Cattaneo, E M Churazov, J Emig, F Fiuza, and Others. Laboratory evidence of dynamo amplification of magnetic fields in a turbulent plasma. *arXiv preprint arXiv:1702.03016*, 2017. 4.2, 4.4

[117] D H Froula, J S Ross, L Divol, and S H Glenzer. Thomson-scattering techniques to diagnose local electron and ion temperatures, density, and plasma wave amplitudes in laser produced plasmas. *Review of scientific instruments*, 77(10):10E522, 2006. 4.2

[118] R. D. Petrasso, J. A. Frenje, C. K. Li, F. H. Séguin, J. R. Rygg, B. E. Schwartz, S. Kurebayashi, P. B. Radha, C. Stoeckl, J. M. Soures, J. Delettrez, V. Yu Glebov, D. D. Meyerhofer, and T. C. Sangster. Measuring Implosion Dynamics through [Formula presented] Evolution in Inertial-Confinement Fusion Experiments. *Physical Review Letters*, 90(9):4, 2003. 4.2

[119] Torsten A Ensslin and Corina Vogt. The magnetic power spectrum in Faraday rotation screens. *Astronomy & Astrophysics*, 401(3):835–848, 2003. 4.5

[120] B J B Crowley and G Gregori. X-ray scattering by many-particle systems. *New Journal of Physics*, 15(1):15014, 2013. 4.5

[121] MJ-E Manuel, A B Zylstra, H G Rinderknecht, D T Casey, M J Rosenberg, N Sinenian, C K Li, J A Frenje, F H Séguin, and R D Petrasso. Source characterization and modeling development for monoenergetic-proton radiography experiments on OMEGA. *Review of scientific instruments*, 83(6):63506, 2012. 4.6

[122] C K Li, F H Séguin, J R Rygg, J A Frenje, M Manuel, R D Petrasso, R Betti, J Delettrez, J P Knauer, F Marshall, and Others. Monoenergetic-proton-radiography measurements of implosion dynamics in direct-drive inertial-confinement fusion. *Physical review letters*, 100(22):225001, 2008. 4.6

[123] C K Li, F H Séguin, J A Frenje, J R Rygg, R D Petrasso, R P J Town, P A Amendt, S P Hatchett, O L Landen, A J Mackinnon, and Others. Monoenergetic proton backlighter for measuring E and B fields and for radiographing implosions and high-energy density plasmas. *Review of scientific instruments*, 77(10):10E725, 2006. 4.6

[124] A Rigby, J Katz, A F A Bott, T G White, P Tzeferacos, D Q Lamb, D H Froula, and G Gregori. Implementation of a Faraday Rotation Diagnostic at the OMEGA laser facility (submitted). *High Power Laser Science and Engineering*, 2018. 4.7, 5.1.1

[125] Jena Meinecke, H W Doyle, Francesco Miniati, A R Bell, R Bingham, R Crowston, R P Drake, Milad Fatenejad, Michel Koenig, Yasuhiro Kuramitsu, and Others. Turbulent amplification of magnetic fields in laboratory laser-produced shock waves. *Nature Physics*, 10(7):520, 2014. 5.1

[126] Andrii Neronov and Ievgen Vovk. Evidence for strong extragalactic magnetic fields from Fermi observations of TeV blazars. *Science*, 328(5974):73–75, 2010. 5.1

[127] C L Carilli and G B Taylor. Cluster magnetic fields. *Annual Review of Astronomy and Astrophysics*, 40(1):319–348, 2002. 5.1

[128] Massimo Giovannini. Estimating relic magnetic fields from CMB temperature correlations. *Physical Review D*, 79(12):121302, 2009. 5.1

[129] Kandaswamy Subramanian, Anvar Shukurov, and Nils Erland L Haugen. Evolving turbulence and magnetic fields in galaxy clusters. *Monthly Notices of the Royal Astronomical Society*, 366(4):1437–1454, 2006. 5.1

[130] Rainer Moll, J Pietarila Graham, J Pratt, R H Cameron, W-C Müller, and M Schüssler. Universality of the small-scale dynamo mechanism. *The Astrophysical Journal*, 736(1):36, 2011. 5.1

[131] Tsuyoshi Inoue, Ryo Yamazaki, and Shu-ichiro Inutsuka. Turbulence and magnetic field amplification in supernova remnants: interactions between a strong shock wave and multiphase interstellar medium. *The Astrophysical Journal*, 695(2):825, 2009. 5.1

[132] Petros Tzeferacos, A Rigby, A Bott, A R Bell, R Bingham, A Casner, F Cattaneo, E M Churazov, J Emig, N Flocke, and Others. Numerical modeling of laser-driven experiments aiming to demonstrate magnetic field amplification via turbulent dynamo. *Physics of Plasmas*, 24(4):41404, 2017. 5.1, 5.3.3

[133] E Churazov, A Vikhlinin, I Zhuravleva, A Schekochihin, I Parrish, R Sunyaev, W Forman, H Böhringer, and S Randall. X-ray surface brightness and gas density fluctuations in the Coma cluster. *Monthly Notices of the Royal Astronomical Society*, 421(2):1123–1135, 2012. 5.1

[134] Michel Baranger and Bernard Mozer. Light as a plasma probe. *Physical Review*, 123(1):25, 1961. 5.2.1

[135] P M Kozlowski, B J B Crowley, D O Gericke, S P Regan, and G Gregori. Theory of Thomson scattering in inhomogeneous media. *Scientific reports*, 6:24283, 2016. 5.2.2

[136] J S Ross, S H Glenzer, J P Palastro, B B Pollock, D Price, G R Tynan, and D H Froula. Thomson-scattering measurements in the collective and noncollective regimes in laser produced plasmas. *Review of Scientific Instruments*, 81(10):10D523, 2010. 5.2.2

[137] Hye-Sook Park, D D Ryutov, J S Ross, N L Kugland, S H Glenzer, C Plechaty, S M Pollaine, B A Remington, A Spitkovsky, L Gargate, and Others. Studying astrophysical collisionless shocks with counterstreaming plasmas from high power lasers. *High Energy Density Physics*, 8(1):38–45, 2012. 5.3.2, 5.2

[138] R P Drake and G Gregori. Design considerations for unmagnetized collisionless-shock measurements in homologous flows. *The Astrophysical Journal*, 749(2):171, 2012. 5.3.2

[139] S I Braginskii. Transport processes in a plasma. *Reviews of plasma physics*, 1:205, 1965. 5.3.2

[140] N L Kugland, D D Ryutov, P Y Chang, R P Drake, G Fiksel, D H Froula, S H Glenzer, G Gregori, M Grosskopf, M Koenig, and Others. Self-organized electromagnetic field structures in laser-produced counter-streaming plasmas. *Nature Physics*, 8(11):809, 2012. 6.2

[141] V D Shapiro, R Bingham, J M Dawson, Z Dobe, B J Kellett, and D A Mendis. Energetic electrons produced by lower hybrid waves in the cometary environment and soft X ray emission: Bremsstrahlung and K shell radiation. *Journal of Geophysical Research: Space Physics*, 104(A2):2537–2554, 1999. 6.2

[142] A J Harvey-Thompson, S V Lebedev, S Patankar, S N Bland, G Burdiak, J P Chittenden, A Colaitis, P De Grouchy, H W Doyle, G N Hall, and Others. Optical Thomson scattering measurements of plasma parameters in the ablation stage of wire array Z pinches. *Physical review letters*, 108(14):145002, 2012. 6.2